DEVELOPMENT AND CHARACTERIZATION OF MATERIALS FOR INTERMEDIATE TEMPERATURE SOLID OXIDE FUEL CELL ANODES

A Dissertation
Presented to
The Academic Faculty

by

Ben Michael deGlee

In Partial Fulfillment
of the Requirements for the Degree
Doctor of Philosophy in
School of Materials Science & Engineering

Georgia Institute of Technology
August, 2019

DEVELOPMENT AND CHARACTERIZATION OF MATERIALS FOR INTERMEDIATE TEMPERATURE SOLID OXIDE FUEL CELL ANODES

Approved by:

Dr. Meilin Liu Advisor
School of Materials Science & Engineering
Georgia Institute of Technology

Dr. Lawrence Bottomley
School of Chemistry & Biochemistry
Georgia Institute of Technology

Dr. Preet Singh
School of Materials Science & Engineering
Georgia Institute of Technology

Dr. Joseph Sadighi
School of Chemistry & Biochemistry
Georgia Institute of Technology

Dr. Dong Qin
School of Materials Science & Engineering
Georgia Institute of Technology

Date Approved: April 11, 2019

ACKNOWLEDGEMENTS

I would like to acknowledge the many wonderful people who have supported me throughout my PhD work. First and foremost, my lovely wife has been, and continuous to be, a spectacular partner. Her patience and love has elevated me above the many obstacles I've faced during my time in graduate school, for which I will always be grateful. I'd like to personally thank the members of the Sandhage group who helped me at the start of my graduate career, especially Dr. Phil Brooke, Dr. Taylor Shapero, Dr. Brandon Goodwin, and Dr. Nick Semenikhin. Without the daily discussions, hands-on tinkering and early mentorship of these dear colleagues I would not be the engineer or scientist that I am today.

Furthermore, I'd like to thank all the members of the Liu group, who graciously welcomed me into their lab and have been instrumental in the production of this work. Dr. Brian Doyle was a constant source of optimism, never losing his hopeful attitude even when experiments were blowing up in our faces. Without the hard work and hard won SOFC skills of Dr. Yu Chen, this dissertation, as well as our co-authored publications, would simply not be possible. Dr. Bote Zhao has been an ever-present motivator, and his scientific advice has been well appreciated during my time at Georgia Tech. Ryan Murphy has been an essential trouble-shooter and confidant and has made incredible selfless efforts to construct our new high-functioning, safe, and impressive SOFC testing lab. The Liu group has too many members to thank everyone, but I hope that my current and former colleagues know that I am and always will be grateful for their welcoming and supportive attitudes.

Finally, I’d like to thank my committee members for their support during the preparation of this document. I chose these members not only for their expertise but for dedication to education as well as research. This value is especially represented by my advisor, Prof. Meilin Liu, a dedicated lecturer and scientist with a genuine interest in the success of his students both in his classroom and in his lab. In addition, I want to acknowledge that this work was partially supported by the US Department of Energy ARPA-E REBELS Program under award number DE-AR0000502.

TABLE OF CONTENTS

LIST OF TABLES

LIST OF FIGURES

LIST OF SYMBOLS AND ABBREVIATIONS

SOFC	Solid Oxide Fuel Cell
OCV	Open Circuit Voltage
DFT	Density Functional Theory
SDC	Samarium Doped CeO_2
GDC	Gadolinium Doped CeO_2
YSZ	Yttrium Stabilized Zirconia
MIEC	Mixed Ionic Electronic Conductor
LSCF	Lanthanum Strontium Cobalt Ferrite $(La_{0.60}Sr_{0.40})_{0.95}Co_{0.20}Fe_{0.80}O_{3-\delta}$
IT-SOFC	Intermediate Temperature Solid Oxide Fuel Cell
LT-SOFC	Low Temperature Solid Oxide Fuel Cell
PBSCF	$PrBa_{0.5}Sr_{0.5}Co_{1.5}Fe_{0.5}O_{5+\delta}$
ARL	Anode Reforming Layer
BZCYYb	$BaZr_{0.1}Ce_{0.7}Y_{0.1}Yb_{0.1}O_{3-\delta}$
EIS	Electrochemical Impedance Spectroscopy
TPB	Triple Phase Boundary
SEM	Scanning Electron Spectroscopy
EDS	Energy Dispersive Spectroscopy
XRD	X-ray Diffraction
TEM	Transmission Electron Microscopy

SUMMARY

Solid Oxide Fuel Cells (SOFCs) are demonstrated energy conversion devices which directly convert chemical energy into electrical energy through high temperature electrochemical oxidation of fuels. Although more efficient than current energy production methods, there remain serious obstacles before these devices can be fully implemented into the modern energy infrastructure. Lowering SOFC operating temperatures to less than 600 °C would expand the application of SOFCs while dramatically reducing system complexity and cost, but performance of these devices remains prohibitively low, and many corrosion mechanisms are exasperated under these conditions. Critically, the operation of SOFCs directly on hydrocarbon fuels has the highest potential for technological impact, but activity of state-of-the-art materials toward these fuels is relatively low compared to hydrogen, and SOFCs can quickly degrade due to the deposition of solid carbon (coking).

To address these obstacles, this work focuses on two key issues in SOFC technology development: improvement of SOFC materials and advancement of SOFC characterization techniques. To address the first issue, a high performing SOFC is designed and demonstrated, uniquely suited for low temperature direct methane operation through the addition of an internal reforming catalyst layer. In situ spectroscopy was used extensively to evaluate the defect and surface structure of the reforming catalyst, directly relating the material structure to device performance. The second issue is addressed through the development of a testing platform for quantitative comparison of different anode surface coatings, as well as the design and fabrication of in situ equipment which increases the current testing capability of the SOFC community.

The key conclusions made in this work are that Ru and Ni can be substitutionally doped into a CeO_2 host lattice, resulting in unique defect structures that enable a high-performance, low-temperature SOFC internal reforming layer. Through the combination of in situ Raman spectroscopy and DFT simulation, the role of each dopant in the material's performance was analyzed, with ionic Ru enhancing the defect structure and steam activation of the host lattice, and ionic Ni providing preferred sites for C-H bond activation. Through the fabrication of a patterned model cells, a new testing platform for Ni-SDC anode development was realized, allowing the quantitative comparison of catalytic and electro-catalytic activities of different materials coated on the anode surface under SOFC operating conditions. The applicability of this platform was demonstrated by validating a number of key assumptions, and comparison of several candidate anode coating materials.

These conclusions build upon the current SOFC literature, and provide clear direction for future research. The Anode Reforming Layer (ARL) component has clearly shown it's potential, and should be considered for more widespread SOFC application in lower temperature direct hydrocarbon SOFCs. The study of precious metal doped CeO_2 for use in low-temperature SOFCs is warranted by the high performance achieved in this work, as well as the demonstration of in situ Raman spectroscopy as an effective tool for investigating these materials. Most interesting is the application of these materials not just as an anode reforming layer, but as an infiltrated catalyst layer, where they are likely to improve not only reforming reactions, but also electrochemical reactions. The embedded mesh Ni-SDC model cell, described in this work, is well-suited for both screening candidate catalyst coating materials and investigating mechanisms of electrode reactions using *in situ* analysis. By using model cells to optimize and study these infiltrated materials

first, the eventual application to anode-supported button cells will be less empirical and more efficient, as these model cells will provide more rigorous understanding of the effect of the material compared to traditional button-cell testing.

CHAPTER 1. INTRODUCTION

1.1 Motivation of Work

Modern energy production is transitioning away from traditional gas and coal fired plants to more efficient alternative forms of energy. There are clear incentives from an environmental, ethical, and commercial stand-point to develop new technologies which burn less fossil fuels, more efficiently, until renewable sources of energy can replace the current energy infrastructure. Fuel cells have high chemical to electrical conversion efficiency, with the potential to produce zero emissions (other than H_2O). Solid Oxide Fuel Cells (SOFCs) are especially attractive, since they provide a transition technology, with the ability to run on the hydrocarbon fuels that power our current infrastructure, as well as the hydrogen fuel poised to be the foundation of the future energy infrastructure. Although the technology has already been implemented in the current marketplace, wide-spread use is limited by the relative cost. This cost is primarily caused by the high operating temperatures required by these devices (~800 °C – 1000 °C), which leads to several disadvantages such as expensive housing materials, accelerated corrosion, and slow start-up times. This is especially disadvantageous for small-scale energy generation, or distributed generation, wherein large power plants are replaced by a larger number of smaller systems to reduce transmission losses, placed directly at the point of use (residential building or industrial campus). As distributed generation is expected to dominate the future energy landscape, there is a clear commercial and technological need to lower the operating temperatures of these devices, while retaining fuel flexibility and high performance.

This is fundamentally a materials science problem, as new SOFC materials must be designed with higher conductivity, stability, and activity at these proposed lower temperatures (<600 °C). Functional electrode coatings are an effective strategy to improve SOFC performance by increasing power output (catalytic activity, conductivity, surface area) as well as stability (physically isolate sensitive components from poisons, catalyze the chemical removal of poisons). Use of electrode coatings also accelerates device development, as the base architecture and manufacturing of the cell is left unchanged and only a single infiltration step is added to the process. SOFC development has been relatively slow, with commercial materials largely unchanged for decades. This is due to the chemical complexity of SOFC operation, wherein performance is affected by numerous competing factors in addition to material properties, including microstructure, material compatibility, temperature management, gas distribution, sealing, and fabrication. This leads to technological advancement largely through empirical evidence, rather than fundamental understanding and rational design of these systems. Therefore there is a critical need for improved characterization and cell testing techniques to better understand SOFC materials under operating conditions. Model testing platforms for isolating specific processes and interfaces are required to enable more targeted experimentation, and to use the more fundamental results to rationally design new materials for improved SOFC performance.

1.2 Research Objectives

1.2.1 Engineering Objectives

- Design and fabricate high performing direct methane SOFCs for lower temperature operation, focusing on new anode reforming layer materials
- Demonstrate a model cell testing platform for intermediate temperature SOFC, focusing on the anode surface and anode surface coatings
- Develop advanced operando characterization capability

1.2.2 Scientific Objectives

- Form structure-property relationships for high performing anode reforming layer material (co-doped Ru-Ni-CeO_2)
- Validate key assumptions of model cell testing platform, and use this platform to quantify fundamental properties of SOFC anode materials.

1.3 Description of Dissertation Structure

This dissertation consists of three main sections. First, Chapters 2 and 3 contain the relevant background information required to provide adequate context for the work, as well as descriptions of the technical approaches used in the described experiments. The second section, Chapter 4, describes the design and testing of a high performing SOFC which exhibits high performance on direct methane fuel at low temperatures, enabled by a novel catalyst layer composed of Ru and Ni doped CeO_2. The third section, Chapter 5, describes the development of new characterization and testing capabilities for SOFC materials, namely a model cell for investigation of new catalysts on Ni-SDC anode surfaces, and the fabrication of an operando Raman testing chamber which enables testing of full SOFC button-cells. Finally, there is a brief section (Chapters 6 and 7), which contains the key conclusions and recommendations for future work, followed by an appendix which

includes preliminary data which was beyond the scope of the dissertation but may be useful to future PhD students continuing along this research direction.

CHAPTER 2. BACKGROUND

2.1 Solid Oxide Fuel Cells (SOFCs)

Fuel Cells are electrochemical devices that produce energy through oxidation and reduction reactions. The principle of operation is very similar to that of a conventional battery, the key difference being that the reactive species are continuously fed to the system, as a *fuel*, rather than being a limited and self-contained supply. Fuel cells are poised to replace traditional combustion based heat engines for energy production. They have no moving parts, produce clean exhaust products and are not bound by Carnot's theorem and can therefore achieve very high efficiencies at low temperatures.

There are a variety of fuel cell types available, as illustrated in Figure 1. This work focuses on Solid Oxide Fuel Cells (SOFCs), defined by their solid-state oxygen conducting ceramic electrolyte. SOFCs traditionally operate at higher temperatures (650 °C – 1000 °C) due to the high activation energies required for diffusion of oxygen ions through ceramic electrolytes. These temperatures add complexity and cost to these devices; components must be able to withstand these conditions and the accelerated corrosion that comes with it. Despite the extreme operating environment, SOFCs remain one of the most attractive class of fuel cells because of their all solid state construction, low-cost electrode materials requirements (Pt-free), and most importantly, fuel flexibility. Hydrocarbon fuels can be directly fed to SOFC anodes to create electrical energy, immediately applicable in the modern hydrocarbon fuel infrastructure.

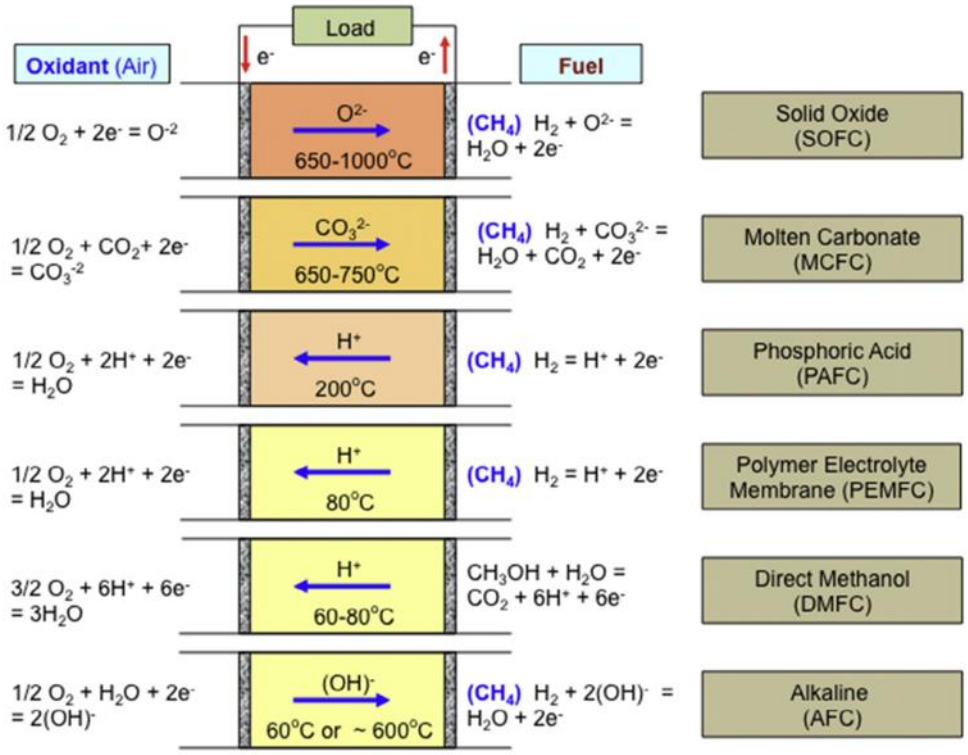

Figure 1 – Anodic and cathodic reactions, standard reaction temperatures and diffusing species involved in the basic operation of common fuel cell classes. Figure adapted from Gur et al.[1]

2.1.1 Operating principles

For SOFCs to produce electrical energy, redox reactions must be coupled between the anode and cathode sides of the electrolyte. The fuel is oxidized at the anode, producing electrons and exhaust products (H_2O in the case of H_2 fuel). These electrons flow through a circuit to the cathode, where they reduce O_2 to O^{2-} anions within the ceramic lattice. The oxygen anions then flow through the electrolyte to the anode, where they react with the fuel and circuit continues. This flow of electrons can be harnessed to produce useful work. The cathodic and anodic reactions are written as

$$\frac{1}{2}O_2 + 2e^- \rightarrow 2O^{2-} \quad (1)$$

and

$$H_2 + O^{2-} \rightarrow 2e^- + H_2O \quad (2)$$

These devices are limited by their Nernst potential, the maximum reversible cell potential between the fuel and the oxidizing streams for a given composition. This potential is derived from the thermodynamic definition of work for a purely electrical system:

$$W_{el} = \Delta G = -nFE \quad (3)$$

Where W_{el} is the electrical work, ΔG is the change in Gibbs Free energy for the global oxidation reaction, n is the number of electrons transferred, F is Faraday's constant (the charge associated with one mol of electrons), and E is the electrical potential of the cell. We can relate the Gibbs energy change to the fugacities of the reacting species by the relation:

$$\Delta G = \Delta G^0 + RTln(\frac{f_C^c}{f_A^\alpha}\frac{f_D^\delta}{f_B^\beta}) \quad (4)$$

Where ΔG° is the free energy change at standard state pressure, R is the universal gas constant, T is temperature and f_D^δ represents the fugacities and stoichiometries of the example reaction, αA + βB = cC + δD.

By combining Equations 3 and 4 we arrive at the Nernst potential for this reaction

$$E = -\frac{\Delta G}{nF}^{0} + \frac{RT}{nF} ln(\frac{f_A^{\alpha}}{f_C^{c}} \frac{f_B^{\beta}}{f_D^{\delta}}) \quad (5)$$

Or more generally,

$$E = E^0 + \frac{RT}{nF} ln \frac{\prod Reactant\ Fugacity^{v}}{\prod Product\ Fugacities^{v}} \quad (6)$$

Applied to the anodic and cathodic reactions here, and assuming ideal gas behaviour, pH_2

$$E = E^0 + \frac{RT}{2F} ln \frac{pH_2 * \sqrt{pO_2}}{pH_2O} \quad (7)$$

This value E is equivalent to the theoretical Open Cell Voltage (OCV) of the cell, the potential when no current flows through the cell (before the circuit is completed). Theoretical OCV can be calculated for different gas compositions and temperatures, based on the different electrochemical reactions that are taking place. For an SOFC operating in humidified H_2 (3% H_2O) fuel with ambient air (21% O_2) as the cathode, the voltage at 600 °C is calculated as 1.16 V.

Once a circuit is completed and current begins to flow, the actual operating voltage is decreased by several irreversible losses, i.e. polarization. These losses are described by the overpotentials associated with various phenomena such as ohmic resistance to ion and

electron conduction, activation barriers for reactions at the anode or cathode, and mass transfer limitations. Polarization losses can also result from other, non-standard, issues such as poor lead connections, current leakages, or inadequate sealing between anode and cathode atmospheres. These losses can be summarized as:

$$E_{cell} = E_{rev} - \eta_{act,anode} - \eta_{act,cathode} - \eta_{ohmic} - \eta_{concentration} - \eta_{other} \quad (8)$$

The primary goal of the SOFC engineer is to maximize the power density of these devices by systematically identifying each cause of polarization and then designing new materials and architectures to decreases these losses.

2.1.2 State-of-the-art SOFCs

The state of the art SOFC is composed of three basic sections: porous anode support, dense electrolyte, and porous Cathode. The anode consists of a porous ceramic-metal composite (cermet) of nickel and Yttrium Stabilized Zirconia (YSZ). The nickel phase acts as the hydrocarbon reforming and hydrogen oxidation catalyst as well as the electronic conductor. YSZ is an oxygen conducting ceramic with reasonable ionic conductivity at temperatures above 800 °C and good stability while operating in syngas and hydrogen fuels. A dense, thin layer of YSZ also acts as the electrolyte. The porous anode is the thickest section of the device, providing high surface area and mechanical integrity in so-called anode supported cells. The state of the art cathode is a Mixed Ionic-Electronic Conductor (MIEC) Perovskite, e.g. LSCF ($(La_{0.60}Sr_{0.40})_{0.95}Co_{0.20}Fe_{0.80}O_{3-\delta}$) which has high activity toward the

oxygen reduction reaction and does not require a secondary electron-conducting phase. A basic schematic of an anode supported SOFC is given in in Figure 2.

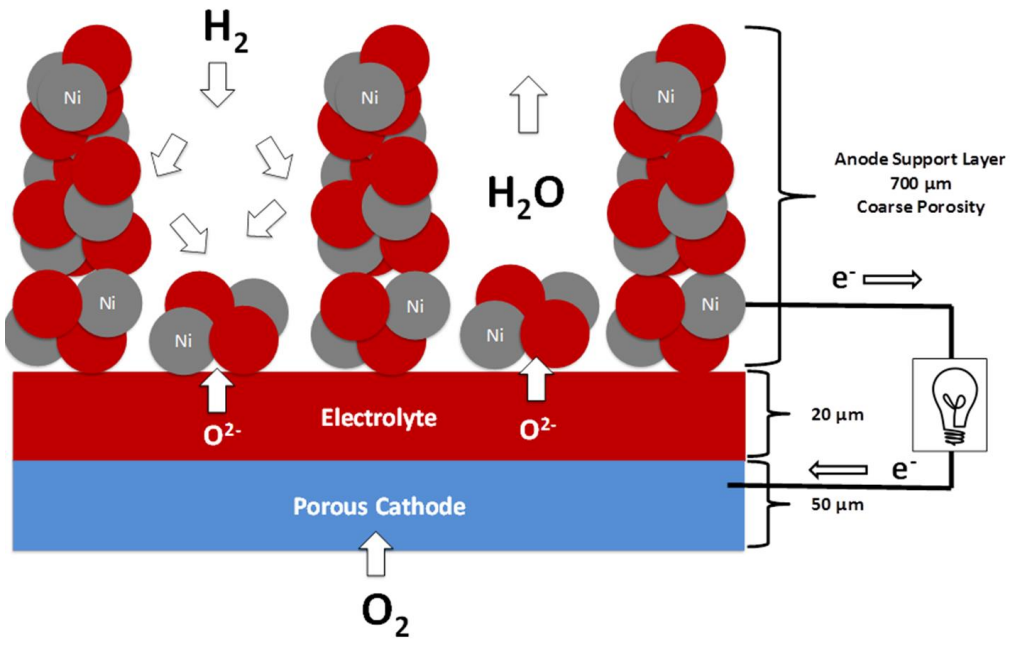

Figure 2 – Modern SOFC anode supported cell architecture, operating in Hydrogen. Fuel enters the porous anode support (~700 µm thick), then as it reaches the electrochemically active regions near the electrolyte, the fuel is oxidized. The electrons produces from the oxidation of the fuel then flow through a circuit towards the cathode, where they reduce O_2 to O^{2-} lattice anions. These O^{2-} anions flow through the electrolyte to the anode, and the circuit is complete.

2.1.3 Intermediate and low temperature SOFCs

The high operating temperatures of traditional Ni-YSZ based SOFCs make these energy systems inherently complex and expensive, requiring high temperature compatible housing and restricting their entry into the modern energy infrastructure. Significate effort has been directed toward Intermediate Temperature cells (IT-SOFCs), operating between 650 °C

and 850 °C and, more recently, Low Temperature cells (LT-SOFCs), which operate below 650 °C.[2]

Enabling these lower temperatures are new ceramic electrolytes with higher ionic conductivities. Gd and Sm doped CeO_2 (GDC and SDC) represent the workhorse of this field due to their high conductivity, stability and ease of processing.[3] A relatively new class of proton conducting perovskites, such as Yttrium doped Barium Cerates (BCY) or Barium Zirconates (BZY), have also shown promise for intermediate and low temperature SOFCs.[4] The activation energy required for proton diffusion is much lower than that for oxygen and therefore the ionic conductivity of these electrolytes is not as affected by decreasing temperatures. Of course, utilizing proton conduction modifies the fundamental reactions taking place at the electrodes. Rather than a flux of oxygen anions flowing toward the anode surface, hydrogen protons are instead drawn from the anode and water is formed on the cathode side. Interestingly, these materials have exhibited promising performance in hydrocarbon fuels at low temperatures, showing remarkable tolerance to coking and sulfur poisoning and therefore are the subject of intense research.[5-7] Significant amounts of steam must be added to the fuel to enable coking resistance with proton conducting systems, in order to provide a source of oxygen required to form volatile oxidation products of carbon (CO_2).

Although great advancements have been made in IT-SOFC technology, operating temperatures remain prohibitively high, and power densities prohibitively low, for many applications.[8,9] Therefore this remains a significant and competitive area of research for the energy community.

2.2 Characterization of SOFCs and SOFC materials

2.2.1 Electrochemical testing

Linear voltammetry is the most common technique for testing SOFC devices. The critical performance metric for these devices is the peak power density supplied by the cell. A well-engineered cell will have minimum polarization losses, resulting in a higher power output and a more effective device. In addition, the I-V-P curves (plots of voltage and power density as a function of current density) can illustrate the contribution of different polarization losses to cell performance under different current density regimes (Figure 3).

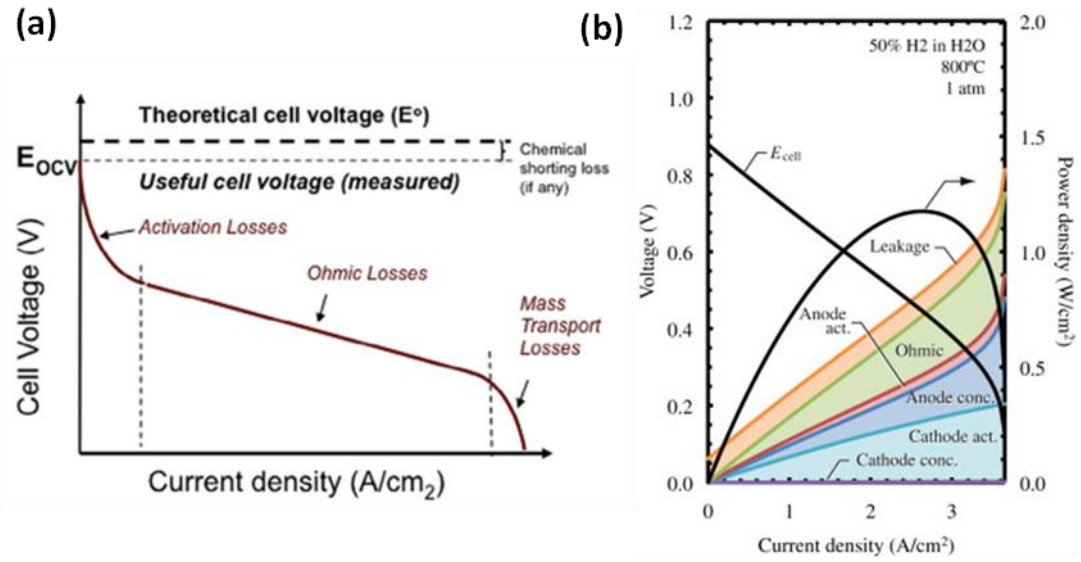

Figure 3 – Predicted I-V (a) and I-V-P (b) describing the polarization behavior of SOFC devices. Figures adapted from Gur and Ghoniem et al[1,10]

For a galvanic system there are typically three polarization regimes. At relatively low current densities, the reaction rate is limited by the charge transfer polarization, representative of the activation energy barrier of the oxidation or reduction reaction. At higher current densities, the overpotential is sufficient for the charge transfer reaction, but as the current is increased the polarization due to ohmic losses also increases (by Ohm's Law $V_{loss} = I*R_{ohmic}$). Ohm's law is a linear function, and therefore as this polarization dominates the I-V curve becomes linear. As the cell reaches peak possible current, the polarization due to mass transfer begins to dominate, as the reaction is occurring at a faster rate than the reactants and products can diffuse to and from the reactive sites, respectively.

These regions are modeled by the well-known Butler-Volmer equation:

$$I = I_0 \left[exp\left(\frac{\alpha_a n F_\eta}{RT}\right) - exp\left(\frac{-\alpha_c n F_\eta}{RT}\right)\right] \quad (9)$$

Where I is the applied current, η is the developed overpotential, I_0 is the exchange current density, and α_a and α_c are the anodic and cathodic charge transfer coefficients, respectively.[11,12] The number of electrons exchanged in the rate limiting step is represented by n, with F and R being Faraday's constant and the ideal gas constant, respectively.

Depending on the conditions of the cell, the Butler-Volmer relation can be simplified. For example, at low polarizations the exponential terms become linear ($e^x \sim 1+x$ as $x \rightarrow 0$) and a low-field approximation is made as

$$I = I_0(\alpha_a + \alpha_c)\left(\frac{F}{RT}\right)\eta \quad (10)$$

Additionally, if the overpotential is sufficiently large in one direction, one of the exponential terms becomes negligible, and the relation simplifies to:

$$\ln(|I|) = \ln|I_0| + \alpha \frac{F}{RT}|\eta| \qquad (11)$$

In cases in which the mass transport of reactants and products to and from the active sites become rate limiting, the concentration polarization must be considered and the equations are modified as follows:

$$I = I_0 \left[(1 - \frac{I}{I_{L,a}}) exp\left(\frac{\alpha_a n F_\eta}{RT}\right) - (1 - \frac{I}{I_{L,c}}) exp\left(\frac{-\alpha_c n F_\eta}{RT}\right) \right] \qquad (12)$$

Where $I_{L,a}$ and $I_{L,c}$ are the limiting current densities for the anode and cathode reactions, respectively.

Another crucial characterization technique is Electrochemical Impedance Spectroscopy (EIS), which provides more detail on the specific sources of polarization occurring in the system. Briefly, a small AC signal (~10 mV in amplitude) is applied to the cell and impedance is measured as a function of frequency. The phase of the sinusoidal current produced by the AC voltage will be shifted depending on the impedance of the cell. By separating the imaginary and real impedance values as a function of the signal frequency, one can deconvolute the capacitive and resistive type responses, which can yield information on the impedance contribution from different frequency dependent phenomena, reaction steps, ohmic resistances, or diffusion processes. Data are often presented in a Nyquist plot for this purpose, which plots the impedance value collected at each frequency as a vector on an imaginary coordinate plane. This results in one or more

loops or semicircles on the plot, which provides ready interpretation and deconvolution of the impedance.

Circuit modeling can be applied to electrochemical systems by assigning proposed reaction steps to fundamental electrical components (e.g. resistors, capacitors, and inductors) arranged in a specific circuit. The most commonly used circuit model is a simplified Randles cell (Figure 4), in which a solution resistance R_S is placed in series with a parallel combination of a capacitive element (either electrical double layer or a constant phase element) and a resistive element assigned to charge transfer. In addition, a resistive diffusion element (Warburg impedance) can be added in series with the charge transfer element, which represents polarization resulting from the flux of reactants to, and products from, the reaction sites. It's important to note that there is no single unique equivalent circuit model that describes each spectrum so empirical models with the fewest elements possible often yield the most useful conclusions.

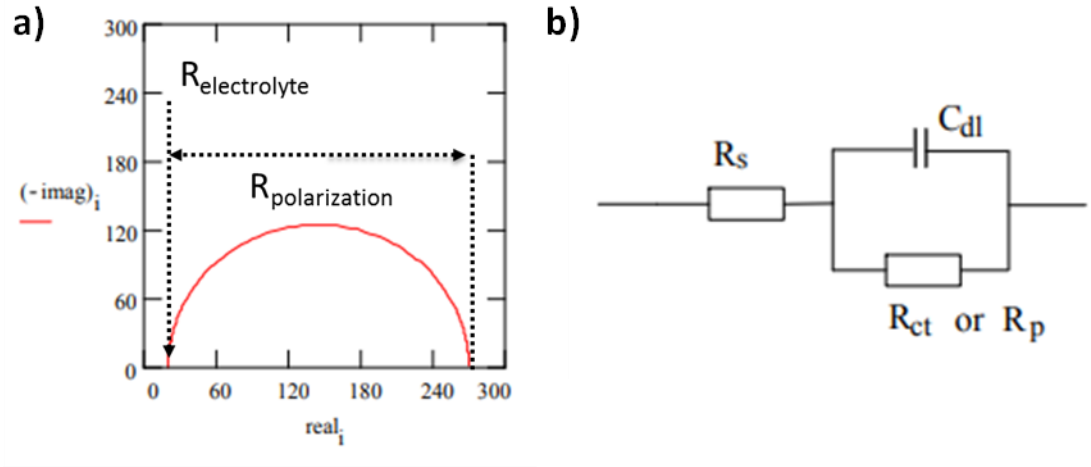

Figure 4 – (a) Simulated impedance spectra of a simple Randles cell, illustrating the locations of the ohmic resistance (high frequency intercept of the x-axis), and the polarization resistance (difference between the high and low-frequency intercepts of the x-axis, (b) circuit diagram of Randles cell simulated in (a).

As the specific impedance resulting from various electrochemical processes are defined, EIS can be used to calculate activation energies for each process by collecting impedance spectra at various temperatures and applying the values to an Arrhenius relation in the form of:

$$\mathrm{R}_p = R_{p,0}\exp(\frac{-E_{a,Rp}}{RT}) \qquad (13)$$

2.2.2 Raman spectroscopy

Raman Spectroscopy is a vibrational spectroscopy technique that relies on inelastic scattering of light correlating with the polarizability of the electrons in a molecule. As light interacts with a material, molecules are excited to higher energy states. Usually the molecules relax back to the same ground state (Rayleigh scattering), but some will relax to a slightly higher energy state than ground level (Stokes scattering), as illustrated in Figure 5. This results in scattered light with a shift from the original wavelength to a higher wavelength (lower energy). By placing an edge filter between the scattered light and the detector, you remove the incident wavelength and only allow the shifted (higher wavelength, lower energy, Stokes shift) light to reach the detector. This is the Raman signal.

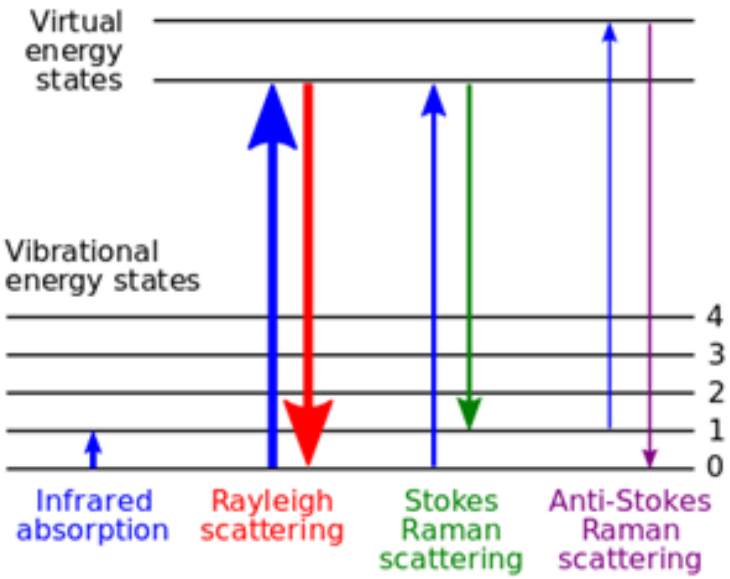

Figure 5 – Schematic of the change in vibrational energy states that result in Raman scattering (Stokes and Anti-stokes).[13]

The intensity of the Raman signal is dictated by the polarizability of the molecule or bond scattering the light. Certain molecular vibrations will distort the electron cloud, allowing the electrons to interact (exchange energy) with the electric field of the incident light. Symmetric vibrations, such as C=C bonding, are very polarizable (distort the electron cloud during vibrations) and therefore often show very strong Raman bands. On the other hand, most asymmetric vibrations, such as the C=O bonding in CO_2, do not distort the electron cloud during vibrations (are not polarizable) and therefore show weak or no Raman bands.

Raman spectroscopy can theoretically be used with any laser wavelength, since it is the *shift* in frequency that correlates with the vibrational mode, rather than the specific adsorption frequency (as in IR spectroscopy). Still, the laser used does have significant effects on the Raman signal. The Raman signal intensity directly depends on frequency of the laser, as seen by the relation:

$$I \propto N(\nu_0 \pm \nu)^4 \sum \left|\alpha_i E_j\right|^2 \qquad (14)$$

Where I is the Raman intensity, N is the number of molecules, ν_o is the incident light frequency, ν is the vibration frequency, α is the polarizability, and E is the electric field strength of the bond. The relatively large exponential term on the frequency variable predicts that even small changes can drastically increase the measured intensity, and therefore lasers with lower wavelength beams are often most attractive for Raman spectroscopy. High frequency (low wavelength) lasers can have drawbacks though, such as induced fluorescence and sample damage.

There are many advantages of Raman spectroscopy compared to similar optical techniques (such as IR absorption). Transmission through the sample is not required, as the scattered light from a sample surface can easily produce enough signal. The flexibility in laser wavelength allows analysis through glass, enabling in situ and operando experiments. In addition, the very small spot sizes of modern lasers provide very high spatial resolution, critical for mapping experiments of sample surfaces.

CHAPTER 3. TECHNICAL APPROACHES

3.1 SOFC device fabrication and testing methods

3.1.1 Fabrication methods used for SOFC devices

3.1.1.1 Tape-casting

Tape-casting was used to fabricate large tapes of green ceramic (anode or cathode) using a doctor blade to control thickness. Slips were made by adding powders to Menhaden Fish Oil, Graphite (pore former), Xylene, ethanol, polyalkylene glycol (plasticizer), butyl benzul phthalate (plasticizer), and polyvinyl butryl (binder) in a 10 : 0.36 : 1 : 4 : 4 : 0.66 : 0.34 : 0.62 ratio, where solvents were measured by volume and remaining components by mass. The slip was degassed in a vacuum oven for 10 min to avoid bubble formation before pouring the slip on the moving tape before the doctor blade. After drying at room temperature for >12 h the sheet was punched into the required size for the circular electrode. Cathode tapes were sinter-bonded to the electrolyte by depositing 30 μL of SDC suspension (1:4:20 ratio by mass of powder, V006 binder, and acetone), allowing to dry for 10 min, then softly pushing the tape against the electrolyte. The green tapes were fired to 1060 °C for 2 h to bond the electrode to the electrolyte. A similar process was also used for fabricating anode supports, firing the unsupported green Ni-cermet tapes to 1000 °C for 2 h. An image of the tape-caster and representative optical image of a green tape are shown in Figure 6.

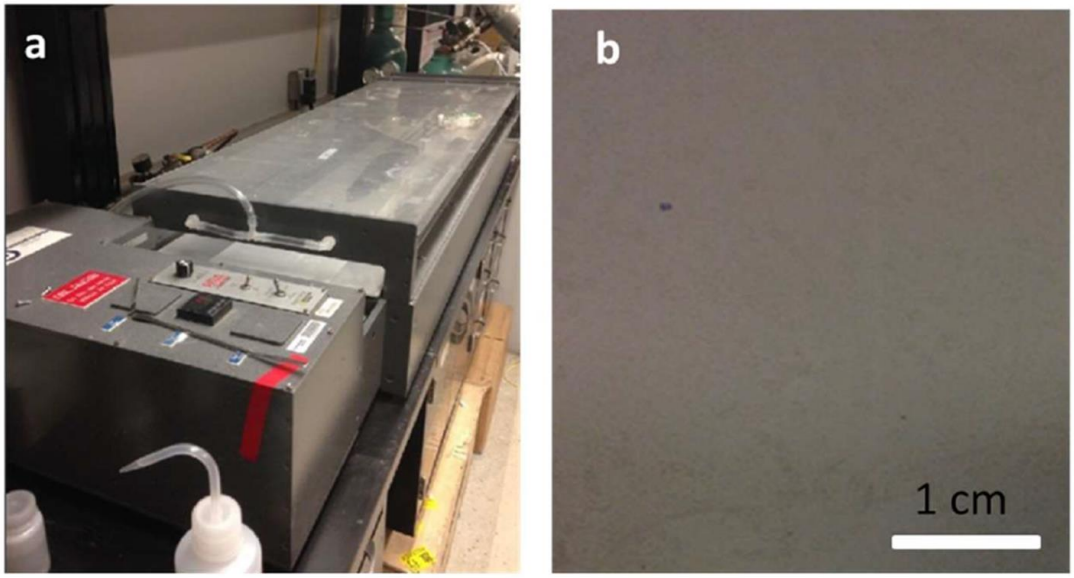

Figure 6 – Optical images of (a) tape-caster used for anode support and cathode green body fabrication, (b) top-down image of tape after drying at room temperature for 12 h. (image courtesy of Dr. Yu Chen).

3.1.2 Button-cell assembly and testing

Button cells are the work horse of SOFC materials development. A large scale, commercially viable SOFC system is composed of a stack of planar or tubular SOFCs, which requires complex current collection, temperature management, and gas distribution systems. A button-cell is a small circular SOFC fabricated by dry-pressing or tape-casting, often between 10 mm and 25 mm in diameter. These cells can be easily sealed to the end of a similar diameter ZrO_2 or Al_2O_3 ceramic tube, creating a controlled atmosphere on the anode side of the cell (inside the tube). These tubes are mounted into a simple compression fitting and can therefore can support and provide fuel to a single cell within a standard lab-scale furnace. Silver wire is guided along the tube and connected to each electrode using

silver or nickel based conductive pastes. A simple compression fitting tee is used to provide input and exhaust to the cell, using a smaller diameter ceramic tube to provide fuel input directly at the anode surface. A schematic and example of the button-cell fixtures used in this work are shown in Figure 7.

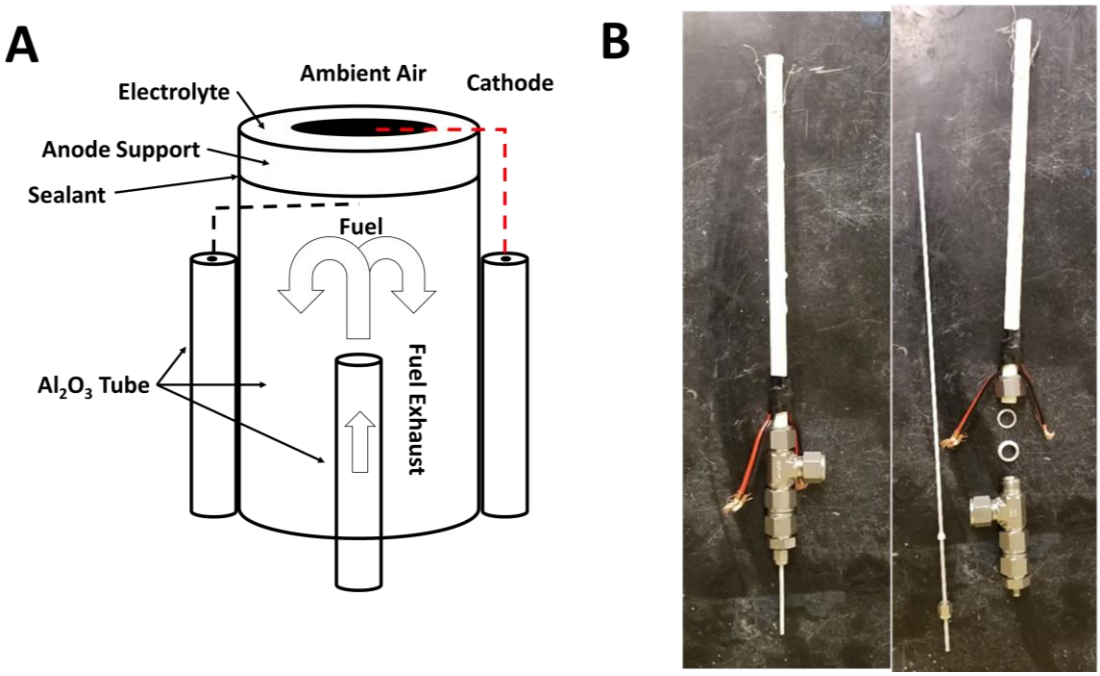

Figure 7 – (A) schematic of button-cell testing set up and (B) photograph of testing setups used in this work, including the Swagelok fittings which hold the input and exhaust lines.

Although this is the simplest technique for testing SOFCs, there are some drawbacks. Fuel utilization is inherently low compared to stack-level systems, as not all of the fuel gas is confined to flow through the porous anode, and therefore not all of the fuel interacts with the active sites. Ambient air within the furnace is used for the cathode of the cell, which can yield lower power compared to flowing a controlled atmosphere over the cathode, especially if pure oxygen is used rather than the ~21% O_2 present in air. Still, these devices

are the most simple and cost/time efficient strategy for testing new SOFC designs without the complications and cost of stack testing.

3.2 Material synthesis and deposition

3.2.1 Combustion synthesis

In addition to standard solid state reactions of precursor powders, combustion synthesis was also used to make small batches of powders and doped catalysts. In this method, metal nitrate precursors are dissolved in an aqueous solution of a suitable chelating agent, e.g. Citric Acid, EDTA, or Glycine. This agent forms metal organic complexes with the cations, increasing their solubility. As the solution is heated a gel is formed and once a critical temperature is reached a violent combustion reaction is ignited. Since the nitrate species act as the oxidant, and chelating agents as fuel, the combustion can quickly each temperatures well above 1000 °C. [14] These brief, but extreme, high temperatures facilitate the formation of complex doped oxides without the use of high temperature furnaces and slow solid state reactions. Correct phase formation is assisted by the homogenous distribution of the cations within the gel, as well as the normalizing the decomposition temperatures of the metal precursors. If only metal nitrates are dissolved in solution, nitrate salts will simply precipitate during heating. Different Nitrates have dramatically different decomposition temperatures in air, therefore oxides will be formed at different times and multiple phases will be produced rather than a pure doped phase.[15] Powders formed through this method have relatively high surface areas and nanoscale pore features and crystal sizes which makes them very effective for catalysis and low temperature sintering

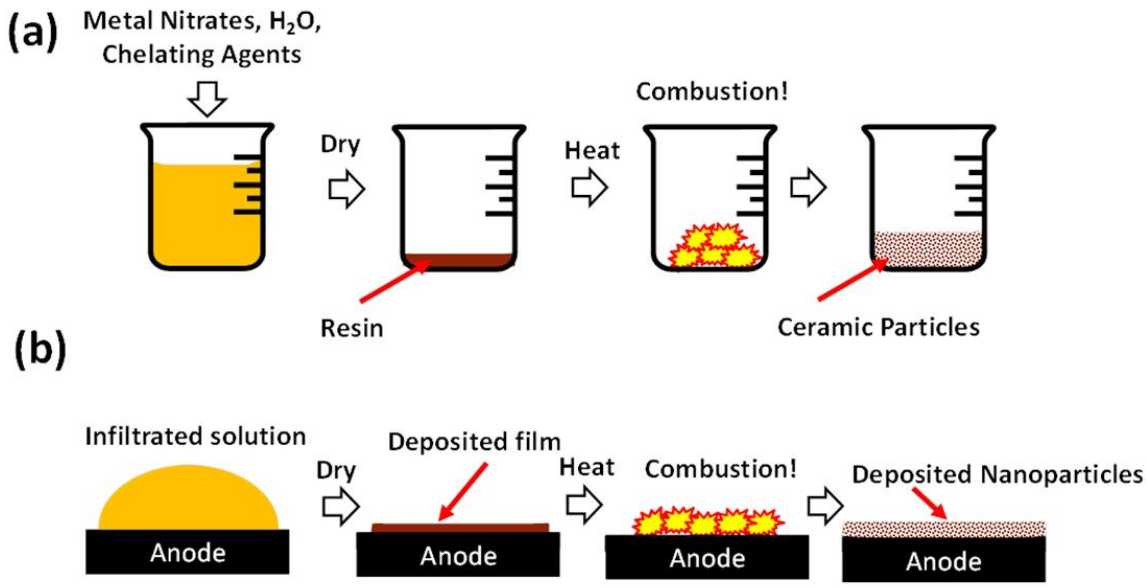

Figure 8 – Simple illustration summarizing (a) the basic steps of combustion synthesis and (b) the solution infiltration of a combustion precursor solution

Although well-controlled systematic investigations are rare, the most important factors controlling product morphology and phase purity are: choice of chelating agent, cation to agent ratio, and fuel to oxidant ratio.[14,16] _ENREF_15Chelating agents with stronger affinity to all of the cations present, and those which can form complexes with multiple cations, provide the most phase pure products. The fuel to oxidant ratio controls the local temperatures reached during the combustion. According to propellant chemistry, fuel-lean and fuel-rich mixtures will be kinetically limited and will not allow for the rapid self-promoting combustion that a stoichiometric mixture will have, and therefore will not reach the high temperatures necessary to form doped oxides.[17] For the purposes of this work, an excel spreadsheet was used to calculate the required chelating agent to cation ratio for the ideal fuel-oxidant ratio, following the approach of Jain et al to calculate and balance the oxidizing and reducing power of each precursor. [18]

3.2.2 Solution Infiltration

Solution infiltration is a useful and popular technique for coating porous anode and cathode electrodes with functional metals and metal oxides. Readily available metal oxide precursors (e.g. Nitrates) and complexing agents (e.g. Citric Acid, Glycine, EDTA) are dissolved in a suitable solvent (in an identical approach as for combustion synthesis solutions) and deposited on the porous electrode. Often, a surfactant is added (e.g. 0.1% wt% Triton-X 100) to lower the surface tension of the solution and promote the complete wetting and infiltration of the porous structure. After drying, the infiltrated electrode is calcined to form the desired phase of the coating.

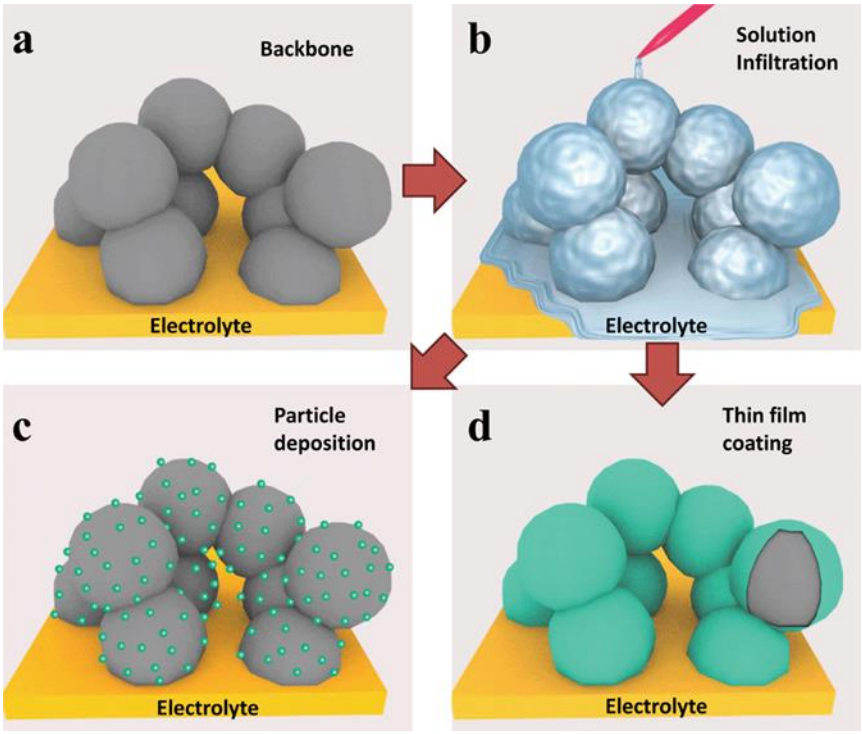

Figure 9 – Porous electrode backbone (a) is wetted with solution of metal precursors and complexing agents (b). After calcination two coating morphologies are possible: discrete particles (c) and an interconnected film (d).Figure reproduced from Ding et al[19]

Although this may appear like a very straightforward technique, the structure and morphology of the film can depend on a number of factors. Phase purity, crystallite size, and porosity are determined by the kinetics of the decomposition of precursors during calcination. Coating morphology will depend on number of infiltration cycles, method of infiltration (submerged, vacuum assisted, injected), contact angle and solution viscosity. The performance of these infiltrated coatings is directly related to the structure and therefore deposition by infiltration must be well optimized in order to achieve high performances and great care must be taken in controlling morphology when comparing different chemistries.[20-23] A representative coating morphology of one coating of 0.1 M infiltration solution is shown in Figure 10.

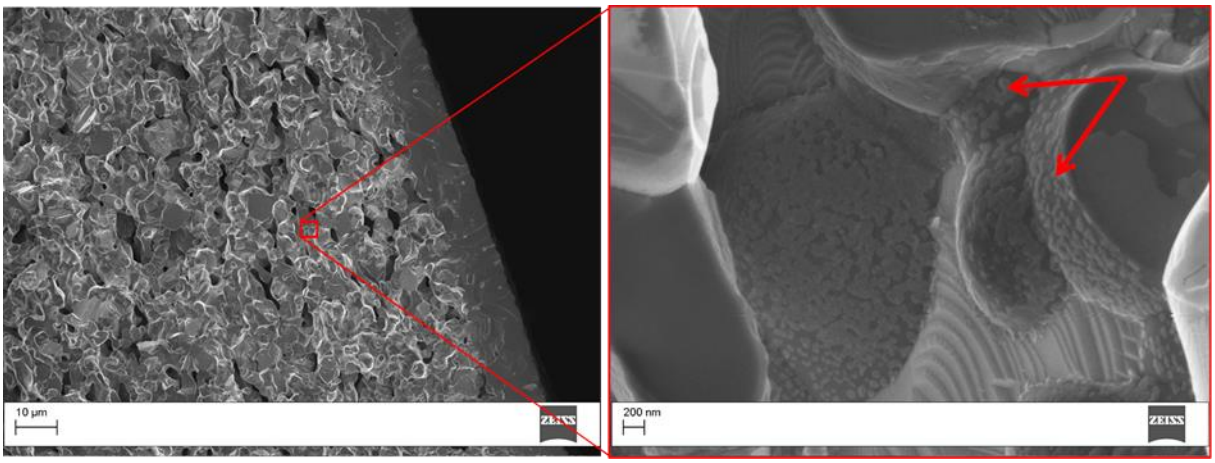

Figure 10 – Cross-section SEM image of Ni-BZCYYb anode backbone near electrolyte showing the presence and morphology of doped ceria catalysts after infiltration and calcination of Nitrate precursor solution (Citric acid, 1.0 Fuel:Ox ratio). Catalyst are present as small nanoparticles as defined by the red arrows in the right-hand image

3.2.3 Physical Vapour Deposition

Sputtering is a common thin film deposition technique that uses the combination of a low vacuum (~10^{-3} mbar) and high voltage to create a plasma over a target material. The ionized gas, typically argon, bombards the target material ejecting high energy free atoms. The vacuum conditions increased the mean free path of the ejected atoms, allowing a relatively conformal deposition of the target material on the substrate of interest. Both DC and RF voltages were used, for conductive and insulating target materials, respectively.

A sputtering system custom built in the Liu group was used in this work, which has both DC and RF power supplies, as shown in Figure 11. Vacuum conditions are controlled through the combination of roughing pump, turbo (capable of 10^{-7} mbar), and a mass flow controller. After pumping the chamber down, the MFC is used to set the appropriate amount of Ar to produce a strong plasma while controlling the mean free path of the ejected atoms. A lower pressure is often advantageous for sputtering of dense films, while higher pressures will introduce porosity and more roughness. For the conditions used in this work, the material deposition was uniform within ~4" diameter circle, which provided enough space for up to six samples to be sputtered simultaneously. Samples were generally coated while at room temperature, which is more likely to produce amorphous films, and therefore all coatings were annealed at 750 °C for 4 h before testing to ensure a crystalline phase had formed.

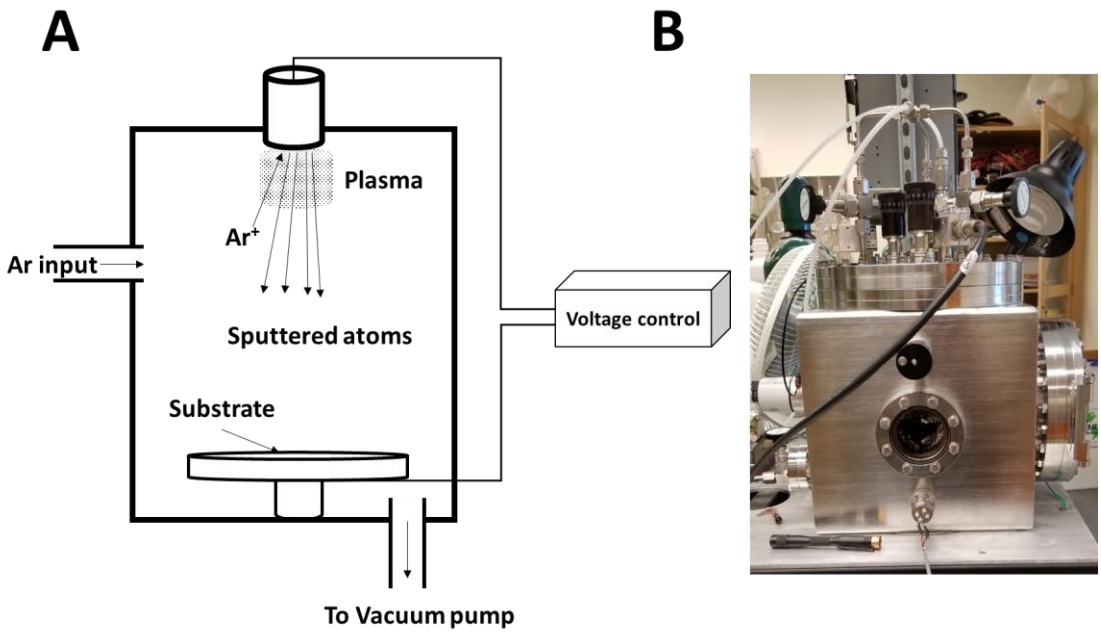

Figure 11 – (a) schematic of RF/DC sputtering system (b) optical image of sputtering chamber used in this work.

3.3 In situ Raman spectroscopy

3.3.1 Description of Raman system and Harrick in situ chamber

A Renishaw RM1000 spectroscopy system equipped with both 633 nm and 514 nm laser sources was used in this work. Laser was focused on the sample through a Leica DM series microscope paired with a Prior Procscan II motorized stage. Several objectives were used, but primarily the 50x and 20x Olympus SLMPlan and LMPlan FL series, respectively, due to their relatively high numerical aperture and long working distance. The minimum spot sized achieved through the 50 x objective is ~1-2 um. A photograph of the beam path system is shown Figure 12.

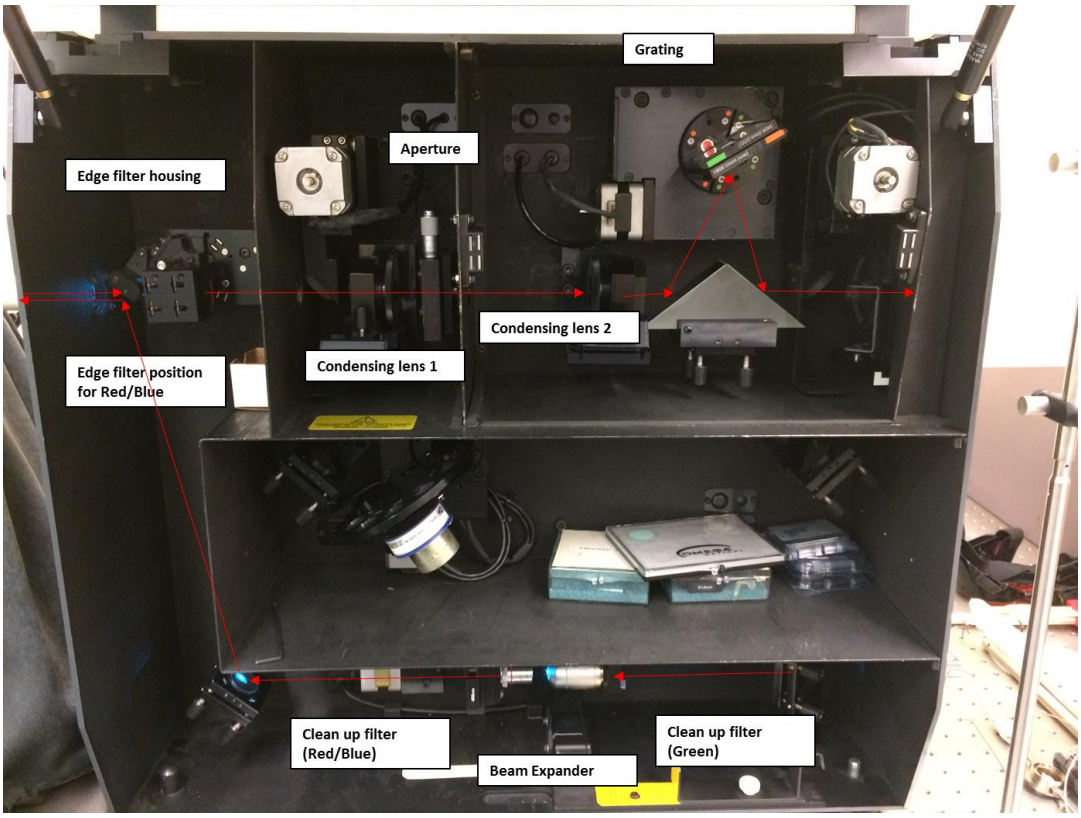

Figure 12 – Photograph of Renishaw RM1000 used in this work with key optical components and beam highlighted.

For in situ measurements, a Harrick Praying Mantis® high temperature testing chamber was used. This chamber provides a controlled atmosphere and direct heating of the material of interest, with a quartz window for optical access. Temperature of the sample was controlled via thermocouple and benchtop PID controller. A diagram of the device is shown in Figure 13.

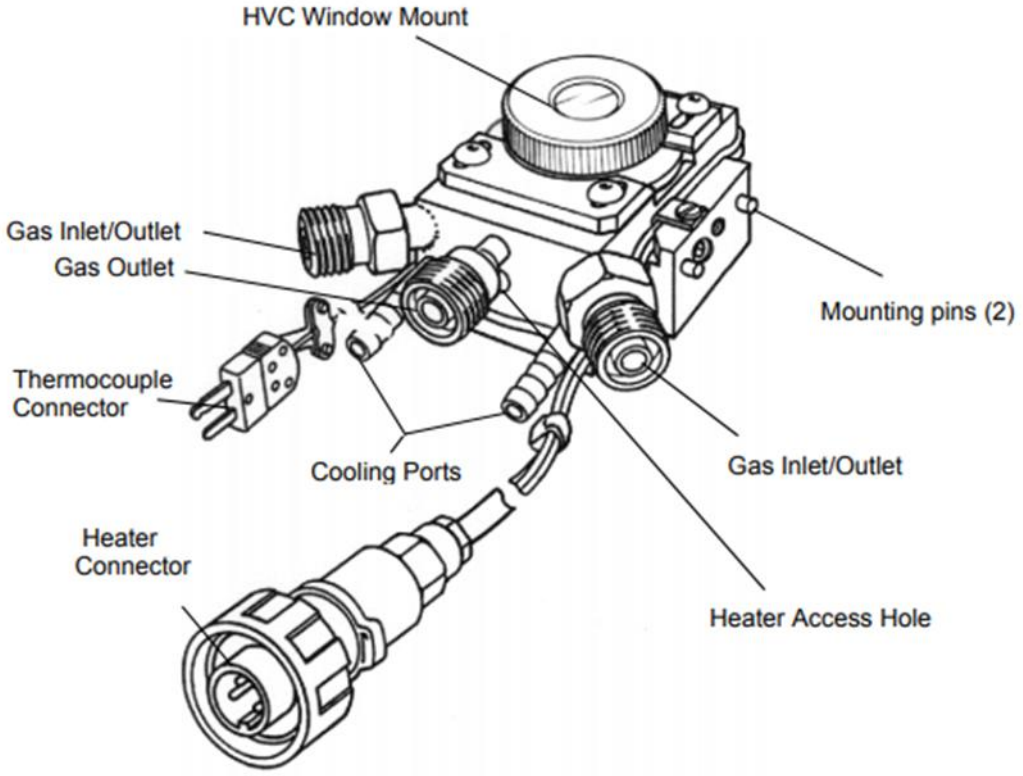

Figure 13 – Schematic of Harrick Praying Mantis ®, showing input and output fittings, water cooling channels, and connections for thermocouple and heating element. Image adapted from Harrick product manual.

These devices have been heavily used in the Liu group to study SOFC materials, most notably in the study of carbon and sulfur poisoning of Ni and Ni-YSZ cermet materials under SOFC relevant conditions. [24-26]. Although critical insights have been gained from these works, these studies were limited to in situ conditions of temperature and atmosphere (H_2 or hydrocarbon fuels). In order to observe phenomena occurring under true SOFC operating conditions, operando experiments are required which require a full cell to be mounted as a membrane assembly between the fuel and air. Under these conditions, a natural chemical potential is established and drawn current density will bring a flux of oxygen into the anode chamber, which is expected to modify the behaviour of the materials.

This possibility will be discussed further in Chapter 5, in the design and fabrication of a novel operando Raman chamber.

CHAPTER 4. DOPED CEO_2 AS AN EFFECTIVE REFORMING CATALYST FOR DIRECT METHANE SOLID OXIDE FUEL CELLS

This chapter outlines the design and development of a state-of-the-art SOFC capable of direct methane operation at temperatures as low as 500 °C. A critical component of the SOFC design was found to be a highly active Anode Reforming Layer (ARL), which enhanced the internal reforming in the anode, enriching the fuel with H_2 and CO as it entered the electrochemically active regions of the anode support. The ARL was composed of CeO_2 particles doped with ionic Ru and Ni, representative of a class of catalysts which show very high activity at relatively low temperatures by making use of precious metals stabilized in a cationic state within a CeO_2 lattice. Special focus is given to the characterization of Ru and Ni doped CeO_2 by Raman spectroscopy, and the effect of these dopants on the defect structure of the catalyst under operating conditions. Structure-property relationships observed through in situ spectroscopy are used to support proposed reaction models.

4.1 Introduction

4.1.1 Hydrocarbon fuels in SOFCs

One of the primary advantages of SOFCs over other fuel cells is their fuel flexibility.[1] Whereas Pt-based Polymer Electrolyte Membrane (PEM) fuel cells are quickly poisoned by the presence of CO, SOFCs can efficiently oxidize CO to CO_2 without degradation.

Therefore, many current SOFC systems are run in series with an external reforming unit, where the hydrocarbon fuel is mixed with steam at high temperatures (~750 °C) to create H_2 and CO, which is then piped into the SOFC stack. Alternatively, SOFCs have the potential to *internally* reform the hydrocarbon fuel, utilizing the H_2O and CO_2 exhaust products of the electrochemical reactions to drive the reforming reactions. Nickel is the primary component of the cermet anode and, in addition to being an excellent H_2 oxidation catalyst, is very active for various reforming reactions. Compared to external reforming SOFCs, internal reforming SOFCs are more commercially attractive as they avoid the significant cost of the pre-reforming unit and water management system, and allow very high concentrations of hydrocarbon fuel to the be directly fed to the device without dilution.

Due to its large domestic supply and developed infrastructure, natural gas (primarily methane) is the ideal hydrocarbon for internally reformed SOFCs. There are several possible reforming reactions for methane, such as Steam Reforming, Dry Reforming, Water Gas Shift, or Methane Pyrolysis:

$$H_2O + CH_4 = 3H_2 + CO \quad (15)$$

$$CO_2 + CH_4 = 2H_2 + 2CO \quad (16)$$

$$CO + H_2O = H_2 + CO_2 \quad (17)$$

$$CH_4 = C_{(s)} + 2H_2 \quad (18)$$

The reforming products, CO and H_2, can then electrochemically oxidized, by:

$$H_2 + O^{2-} = H_2O + 2e^- \quad (19)$$

$$CO + O^{2-} = CO_2 + 2e^-) \quad (20)$$

$$C_{(s)} + 2O^{2-} = CO_2 + 4e^- \quad (21)$$

Although a number of reactions can be written for the direct electrochemical oxidation of CH_4, these reactions are thought to be only minor pathways relative to the oxidation of H_2.[27] Kinetics play an important role within the anode, the driving forces (ΔG) for the electrochemical oxidation of CH_4 and CO are much lower than that of H_2 and the H_2 reaction is much faster, with less steps (oxidation of CH_4 would theoretically be an eight electron process). Much of the surface area of the porous anode will also interact with the fuel before reaching the electrochemically active sites, increasing the probability that the methane is largely converted to H_2 and CO before it reaches an electrochemically active site. For these reasons, it is common practice to expect the voltage of an internally reformed SOFC, regardless of fuel, is that established for the hydrogen equilibrium.

The nickel component of the anode cermet can provide adequate reforming catalysis, but is prone to degradation by carbon deposition and is less active as the operating temperatures are lowered. The same properties that make nickel an effective reforming catalyst make it an excellent catalyst for the deposition of carbon by equation (18). The growth of solid carbon decreases the number of active sites, inhibits gas flow, and causes substantial mechanical stress on the cell. These affects have been mitigated by increasing the levels of steam in the fuel, towards compositions in which Carbon formation is not thermodynamically favored, but the excessive steam required (e.g. 3:1 Steam to Carbon)

comes with the unattractive drawbacks of fuel dilution and system complexity. Therefore, considerable work has been done in studying the carbon deposition mechanisms and identifying different materials which inhibit this growth and are therefore able to tolerate low steam gas compositions.

The incorporation of reforming catalysts that can efficiently convert fuels to hydrogen, with higher activity and stability than the Ni component already present in the cermet anode, is an interesting strategy for direct methane SOFCs. Vernoux et al were the first to propose the strategy of Gradual Internal Reforming (GIR): adding a anode reforming layer optimized for hydrocarbon reforming before the porous anode support (Figure 14).[28,29]

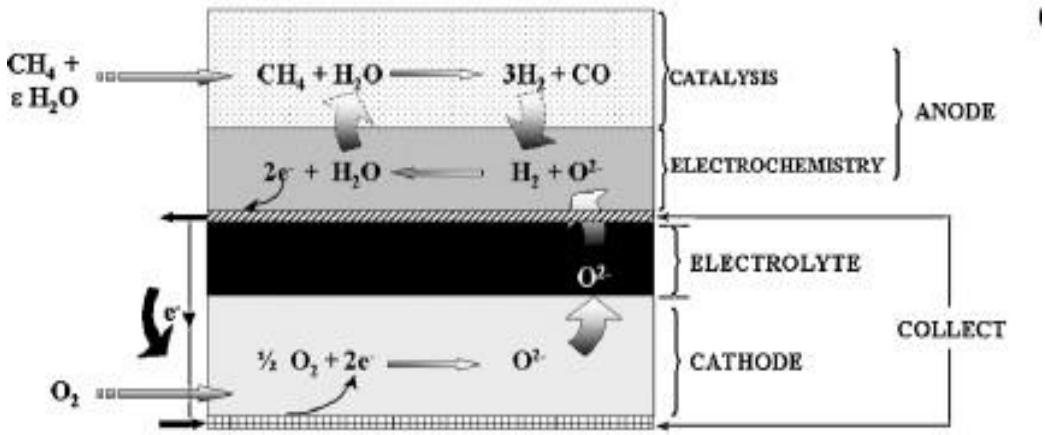

Figure 14 – Diagram showing the operating principle of gradual internal reforming by an Anode Reforming Layer (ARL). Products of electrochemical reactions diffuse into ARL layer where they drive reforming reactions. In this design, hydrogen should ideally be the only species reaching electrochemically active region. (Figure reproduced from Klein et al)[30]

The Ni-based anode is protected from coking due to large concentration gradient that is established across the anode and catalyst layers; the locally high concentration of steam produced near the electrochemically active regions prevents low steam:carbon ratio atmospheres from being established over the Ni component of the cell. Zhan et al generated renewed interested in this approach by demonstrating high performance and stability while operating dry octane fuels. This was accomplished by placing a layer of CeO_2 supported Ru on top of a conventional anode supported SOFC.[31,32] The anode reforming layer was effective enough to achieve power densities of 0.6 W/cm2 at 770 °C without significant coking, even with a relatively large hydrocarbon, octane, as fuel. A Ru/CeO_2 reforming layer has since been utilized in a number of other direct hydrocarbon SOFC designs, where the ARL is consistently found to be critical for power density and cell stability.[33-38] This strategy has demonstrated impressive internal reforming performance and the addition of active anode reforming layers to anode support cells is likely a requirement for next generation direct methane SOFCs.

There are fundamental reasons that methane fueled SOFC exhibit higher performance at high temperatures. Relevant reforming reactions, as well as their Gibbs free energy changes, are given in Table 1, and the Gibbs free energy changes and equilibrium constants for each reaction are plotted in Figure 15.

Table 1 – Calculated Gibbs free energy changes for various methane reforming reactions, calculated with HSC 5.1 software.

Name	Reaction	ΔG @200°C (kJ)	ΔG @500 °C (kJ)	ΔG @ 700 °C (kJ)
Partial Oxidation (PO)	$CH_4 + 0.5O_2 = CO + 2H_2$	-118	-175	-214
Boudouard Reaction (BR)	$2CO = C_{(s)} + CO_2$	-89	-35	0
Water Gas Shift (WGS)	$CO + H_2O = CO_2 + H_2$	-21	-10	-4
Methane Pyrolysis (MP)	$CH_4 = C_{(s)} + 2H_2$	35	5	-16
Reverse Bosch (RB)	$C_{(s)} + 2H_2O = CO_2 + 2H_2$	46	15	-4
Steam Reforming (SR)	$CH_4 + H_2O = CO + 3H_2$	102	30	-20
Dry Reforming (DR)	$CH_4 + CO_2 = 2H_2 + 2CO$	124	40	-16

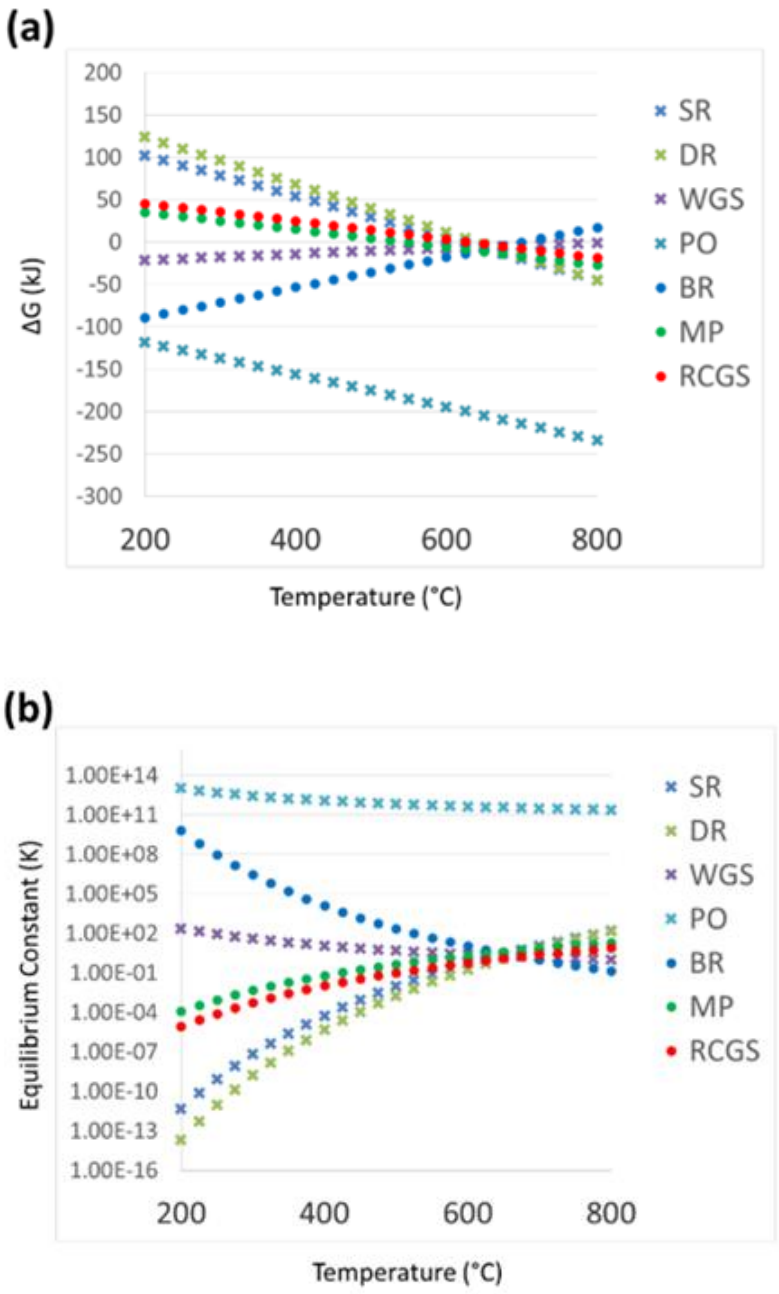

Figure 15 – Gibbs free energy (a) and Equilibrium Constant (b) of relevant reforming reactions as a function of reaction temperature. Lines marked with 'x' represent gas phase reactions, lines with 'o' represent reactions occurring between solid carbon and the gas phase. SR= Steam Reforming, DR= Dry Reforming, WGS=Water Gas Shift, PO=Partial Oxidation, BR=Boudouard Reaction, MP=Methane Pyrolysis, RCGS=Reverse Coal Gas Shift or Reverse Bosch

It's important to note the critical temperature near 650 °C, where the energy changes for many reactions reverse sign. The primary reactions which produce hydrogen from methane in internally reformed SOFCs (Steam Reforming, Dry Reforming, and Methane Pyrolysis) are only thermodynamically favored at high temperatures (>650 °C). This clearly demonstrates the inherent challenges facing internal reforming LT-SOFCs and acts a clear delineating temperature between intermediate and low temperature hydrocarbon SOFCs.

At first glance, these calculations suggest that internal reforming of methane at these temperatures is very difficult, if not impossible. In fact, the well-known Sabatier process utilizes Ni catalysts to form methane from H_2 and CO at ~350 °C, the exact opposite reaction desired in internally reformed SOFCs.[39] Fortunately, in an operating SOFC chemical species are in flux through a membrane. Oxygen is added to the system through the SOFC electrolyte and the subsequent oxidation of H_2 to H_2O or CO to CO_2. This will shift the equilibrium quotient, driving the reaction as long as the flux of oxygen remains sufficiently high, (by LeChetlier's Principle). Modern catalytic membrane reactors have demonstrated this affect, by selectively removing the product from the reactor, the steam reforming reaction can indeed be driven to near completion at 500 °C (ΔG of +30 kJ).[40]

In addition to different reforming conditions, the deposition of coke is also affected by decreasing temperatures. Traditionally, carbon deposition occurs in SOFCs by Methane Pyrolysis (eq 18), but the Boudouard reaction becomes favored at below 650 °C, and excess CO in the system may cause coking by:

$$2CO = CO_2 + C_{(s)} \tag{22}$$

Carbon deposited at low temperatures is also expected to have a different structure than the graphite, carbon nanotubes and carbon fibers commonly seen at standard operating conditions. Deposited Carbon has been reported as encapsulating polymers at low temperatures, and materials that show coking tolerance at high temperatures may not possess the same resilience to coking by CO disproportion and polymeric carbon.[41,42] Identification of coke structure and deposition kinetics is critical to engineering coking tolerant anodes, therefore the relative lack of knowledge regarding low temperature carbon deposition in SOFC is a significant obstacle to LT-SOFC design.[43]

Based on this thermodynamic analysis, the efficient transfer of species across the electrolyte and introduction into the gas phase is a critical requirement for internal reforming SOFC at low temperatures. Cathode activity and electrolyte conductivity must be high enough to facilitate this flux and shift the equilibrium in order to convert high percentages of the methane fuel. Once this high flux of oxygen is established in must be paired with a highly active reforming catalyst that can effectively utilize the flux of oxygen containing electrochemical reaction products in order to keep H_2 and CO concentrations high enough for the cell to operate efficiently.

4.1.2 Ionic precious metals as ARL catalysts

Reforming catalysts have been identified for SOFC applications largely through traditional thermal catalysts techniques, such as flowing reactive gases through a fixed bed reactor and quantifying conversion and selectivity through Mass Spectrometry and Gas

Chromatography. Unfortunately, this does not represent the actual operating environment of the catalyst in a SOFC, especially at low temperatures where reforming reactions are not favored and therefore maximum methane conversion is limited by fuel gas equilibrium. By evaluating ARL performance during SOFC operation, the thermodynamic limitations on the catalysis are shifted by the flux of oxygen into the system or hydrogen out of the system. Drastically different conversion and reforming rates are expected during SOFC operation, and the gas composition near the active sites is expected to be much different than that of the final exhaust stream.

At lower temperatures, it may be possible to make use of ionic precious metals, singly dispersed or doped within a CeO_2 support. In contrast to the metal nanoparticle active sites, the ionic precious metals (e.g. Ru, Pt, or Pd) are present as single atoms, ionically bound to the Ce and O surface species or substitutionally doped into the CeO_2 support bulk. Metiu et al found that ceria doped with 5% Ru was competitive with the best catalysts for methanation (the formation of CH_4 from syngas), and proposed that the reaction occurred on the reduced Ce-Ru-O site. In addition, the dopant dramatically enhanced the Ce^{4+}/Ce^{3+} reduction at lower temperatures relative to un-doped-ceria.[44,45] M.S Hegde pioneered the work on what he has dubbed "Noble Metal Ionic Catalysts" wherein very small amounts of oxidized noble metals are doped into support lattices, including $Pt_xCe_{1-x}O_2$, $Pd_xCe_{1-x}O_2$, and $Ru_xCe_{1-x}O_2$.[46,47] He has shown that this class of catalysts can drastically increase the oxygen storage capacity of ceria, as well as introduce new active sites due to the highly electrophilic nature of oxidized noble metals and the mobilized oxygen vacancies near these dopants. Most interesting is the possibility of a synergy between the co-dopants, which would provide optimal performance with the least amount of the precious metal

dopants, which are often cost-prohibitive.[48,49] Understanding the role of these dopants in the anode reforming layer will enable further improvements and facilitate the transfer of this relatively new class of catalyst into the SOFC field**.**

4.1.3 Rationale of observed solubility of precious metals in CeO_2

The claim that precious or noble metals (e.g. Pt, Pd, Au, Ru, Ni) can be substitutionally doped into the CeO_2 lattice requires explanation and verification, as most of these metals do not show any bulk solid solubility according to respective phase diagrams. Therefore, several works have reported extensive structural characterization of these materials to confirm that these atoms are indeed doped into the material, although the exact mechanism is still debated. Hegde et al was one of the first to report the ionic state of noble metals in CeO_2, which was confirmed by combination of XRD, XPS, HR-TEM, and XANES analysis.[50] They proposed that the mechanism for the observed solubility was due to an electronic interaction between the metal dopant and ceria redox couples, M^{n+}/M^0 and Ce^{4+}/Ce^{3+} respectively. In addition, they suggested that the relatively large difference in valence band energy between CeO_2 and the ionic dopant limit the ability of electron exchange between the two species, effectively stabilizing them in the as-synthesized oxidation state. Several works by Acerbi et al and Metiu et al have supported similar explanations, in which the electronic interaction between the redox couple of the CeO_2 and the noble metal stabilize the dopant in an ionic state under conditions which would normally cause it to reduce and precipitate as a metal.[51 52] Interested readers can find more detailed explanations of this observed solubility in these references, as the specific mechanism for this stabilization was beyond the scope of this work.

4.2 Design of high performing low temperature direct methane SOFC

From the above analysis, a high performing SOFC fueled directly by methane at 500 °C requires several components. First, in order to effectively reform the methane at the anode, the flux of oxygen to the anode compartment (baseline current density in H_2) must be very efficient and therefore a thin electrolyte with high O^{2-} conductivity must be used. In addition, the low operating temperatures will slow the kinetics of the oxygen reduction reactions occurring at the cathode, so a highly active cathode must be selected to overcome this cathodic polarization. The anode support must be able to remain stable under very low steam:carbon ratio atmospheres where coking reactions are favored. Once these factors are addressed, the cell must then be paired with a highly active anode reforming layer that will take advantage of the high oxygen flux to internally reform the methane into a H_2 rich fuel. A schematic of the proposed design is given in Figure 16.

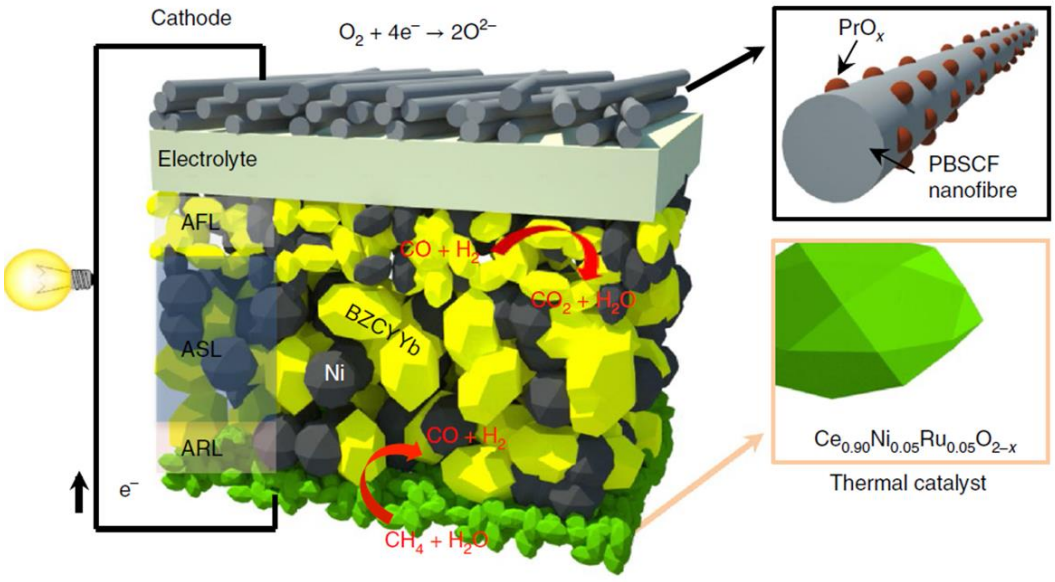

Figure 16 – Schematic of Low Temperature Direct Methane SOFC design. AFL, ASL and ARL represent Anode Functional Layer, Anode Support Layer, and Anode Reforming Layer, respectively. Figure adapted from publication, generated by Dr. Bote Zhao.[53]

A highly engineered nanofiber cathode was fabricated according to recent advancements in low temperature SOFC cathodes done within the Liu group.[54-56] An electrospun mat of PBSCF ($PrBa_{0.5}Sr_{0.5}Co_{1.5}Fe_{0.5}O_{5+\delta}$) fibers was chosen as the cathode material. PBSCF is a highly active double perovskite with high ionic and electronic conductivity at relatively low temperature (low activation energy for ORR and conduction), and recent studies performed in the Liu group have demonstrated the efficacy of the nanofiber architecture.[57] Sm-doped CeO_2 (SDC) was chosen as the electrolyte material, due to its high ionic conductivity at low temperatures and commercial availability (it is a standard material for state-of-the-art IT-SOFCs). A significant drawback from using SDC as an electrolyte is the possibility of electronic conduction under reducing conditions, which can lower the OCV

of the cell to leakage current. To address this issue, the SDC electrolyte was paired with a Ni-BZCYYb ($BaZr_{0.1}Ce_{0.7}Y_{0.1}Yb_{0.1}O_{3-\delta}$) anode support material. The BZCYYb is well-known to provide additional coking tolerance to hydrocarbon fueled cells and has the additional benefit of reacting with SDC during sintering temperatures to form a thin electron-blocking layer at the anode-electrolyte interface. [5,58,59] This blocking layer enables the cell to reach suitable OCV values and removes the deleterious effects of SDC electrolyte reduction. Due to the aggressive coking conditions at the anode, a Ni-BZZYB cermet was further protected with an infiltrated coating of SDC particles, which enhances the coking tolerance of Ni-based SOFC anodes.

By using the highest performing materials set available for the baseline SOFC performance, as described above, the current densities may be large enough to drive the reforming reactions at the ARL even at relatively low temperatures (500 C). The remaining challenge was then to design a highly active anode reforming layer catalyst. After initial screening tests conducted in Prof. Franklin Tao's group at Kansas University, a $Ru_{0.05}Ni_{0.05}Ce_{0.90}O_{2-\delta}$ catalyst was chosen as the ARL. The presence of the Ni-Ru-doped CeO_2 catalyst was observed to be a critical component for both power density and stability under direct methane operation, as outlined in the following sections, and therefore is the focus of this chapter. Inspired by the high performance of the cell, advanced characterization techniques were used to form more detailed structure-property relationships for the co-doped catalyst, as well as to support proposed reaction mechanisms responsible for the observed performance. Suggestions for further development are given at the conclusion.

4.3 Key hypotheses

1. Through incorporation of a co-doped Ru-Ni-CeO_2 catalyst into a highly active SOFC design, efficient and stable internal reforming performance can be achieved at low temperatures (500 C).

2. The defect structure of CeO_2 is modified by the presence of ionic Ni and Ru, and these modifications in structure affect the catalyst properties and operating performance.

3. There exists a synergy between doped Ruthenium and Nickel sites, where the ability of the Ruthenium dopant to enhance CeO_2 reducibility drives oxygen vacancy H_2O activation, whereas the affinity of the Nickel dopant sitefor C-H bond enhances methane activation.

4.4 Fabrication of SOFCs

SOFC devices were fabricated using methods optimized in previous works.[5,60] $BaZr_{0.1}Ce_{0.7}Y_{0.1}Yb_{0.1}O_{3-\delta}$ (BZCYYb) powder was made through solid-state reaction of stoichiometric amounts of barium carbonate, zirconium oxide, cerium oxide, ytterbium oxide and yttrium. oxide (Aldrich Chemicals). Powders were mixed by ball milling in ethanol for 48 h, followed by calcination at 1,100 °C in air for 10 h. After calcination, the powder was ball milled again for another 24 h, followed by another calcination at 1,100 °C in air for 10 h. Ru and Ni doped CeO_2 nanoparticles were synthesized according to a protocol adapted from Mai et al.[61] In a typical synthesis, stoichiometric aqueous nitrate precursors were added dropwise into a 6 M NaOH aqueous solution with vigorous stirring.

Precipitation occurred immediately as solutions mixed, forming an opaque slurry. After 30 min the slurry was transferred to PTFE lined Stainless-steel autoclaves and heated to 100 °C for 24 h. After cooling to RT, the solid product was separated by centrifugation and washed with dH_2O water until a neutral pH was observed. The product was then dried at 80 °C for 12 h, ground into a fine powder in an agate mortar, then calcined at 400 °C for 2 h in ambient air.

Cell fabrication was accomplished by first tape-casting the anode support (50:50 wt% Ni: BZCYYb), as described in section 3.1.1. The green tape was fired at 1000 °C for 2 h, then, a higher surface area Anode Functional Layer (AFL) of NiO–BZCYYb (50:50 wt%) and an SDC electrolyte were sequentially deposited on the anode support by a particle suspension coating process followed by co-sintering at 1,400 °C for 5 h to densify the electrolyte and bond the anode support to the SDC. Electrospun PBSCF nanofibers were mixed with a V006 ink vehicle (Heraeus®) to form the cathode paste.[57] After printing the cathode on the electrolyte surface, the cell was fired again at 950 °C for 2 h. SDC was infiltrated on the anode by dropping 20 μL of 0.1 M SDC nitrate aqueous solution. After drying, a single layer of the $Ni_{0.05}Ru_{0.05}$ $Ce_{0.9}O_2$ (similarly mixed with V006) was painted on the anode outer surface, forming an ~ 15 um thick layer after calcining. Finally, a 5 μL volume of 0.1 M Praseodymium Nitrate aqueous solution was infiltrated onto the fiber cathode surface. The cell with the anode infiltrate (SDC), ARL and cathode infiltrate (PrOx) was then co-fired at 800 °C for 2 h in air before mounting and testing on a standard button cell rig (as described in section 3.1.2).

An SEM cross-section of the final SOFC after fabrication is shown in Figure 17. The thickness of the electrolyte, cathode, and anode reforming layer were near the target thicknesses of 15 um, 50 um, and 40 um respectively.

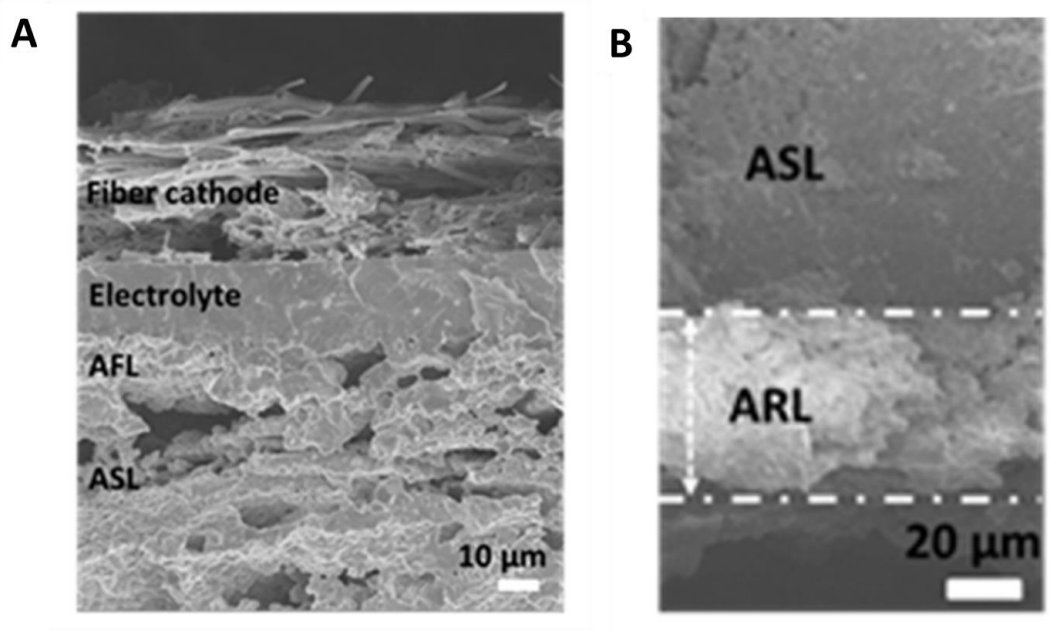

Figure 17 – SEM cross-section of (a) the anode/electrolyte/cathode interface and (b) of the ARL/anode interface (b). Figure adapted from publication.[53]

4.5 Electrochemical performance of SOFC

At the target temperature of 500 C, the optimized device achieved a peak powder density of 0.4 W/cm^2 at 0.5 V in H_2, and 0.37 W/cm^2 in CH_4 (3% H_2O). In addition, long term stability testing at 0.75 V showed complete return to baseline H_2 performance after exposure to nearly dry CH_4, and stable operation in CH_4 for 10 days. The basic device performance is described in Figure 18.

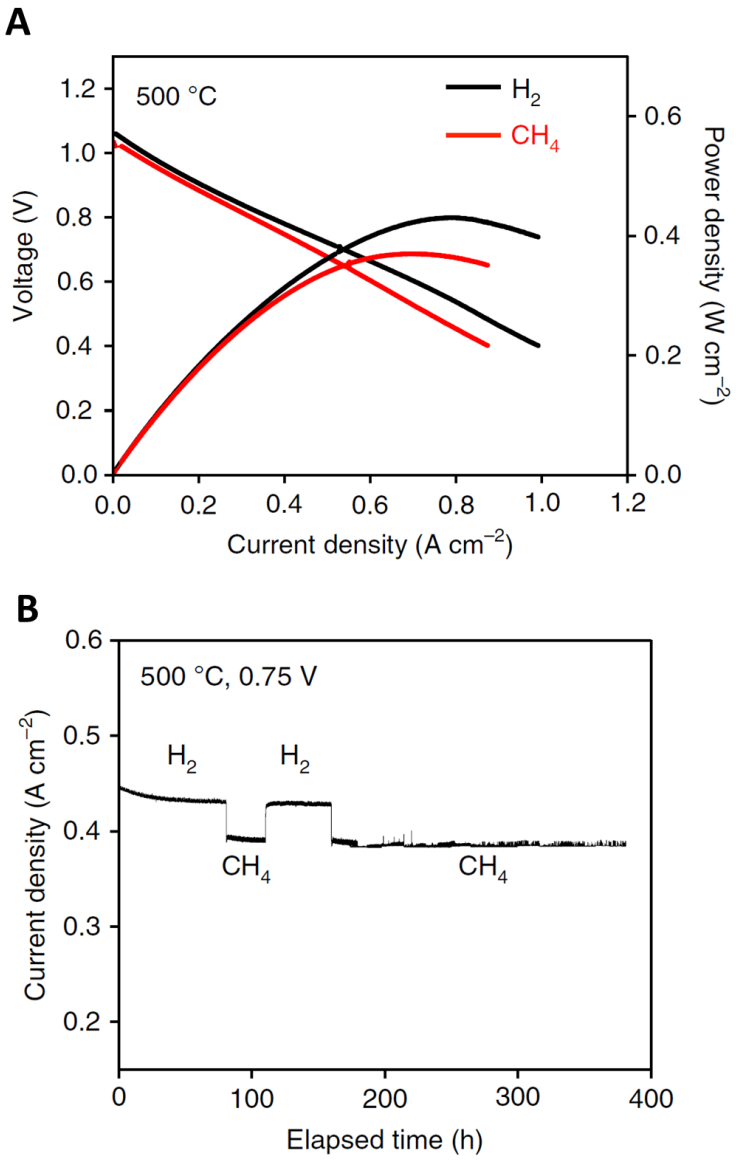

Figure 18 – (A) P-I-V curve for representative SOFC in H_2 and CH_4 fuels. (B) Long term potentiostatic testing at 0.75 V including multiple fuel transitions from H_2 to CH_4. Figure adapted from publication.[53]

This result represents a significant contribution to the current SOFC technology. The performance reported by a selection of recent works testing under similar conditions is shown in TABLE

Table 2 – Comparison of low temperature direct methane SOFC performance to similar works

Cell Design (ARL/Anode/Electrolyte/Cathode)	Fuel Composition	Temp. (°C)	Power Density at 0.75 V (Wcm-2)	Testing Time (h)	Reference
$RuNiCeO_2$/ Ni-BZCYYb/ SDC/ PBSCF	97%CH_4-3%H_2O	500	0.28	400	This work[53]
CeO_2/ Ni-GDC/ LSCF-GDC	20%CH_4-80%H_2O	500	0.12	NA	[62]
Ru(1.5%)/ Ni-BZCYYb/ BZY20/ BCFZY	28.6%CH_4-71.4%H_2O	500	0.1	200	[7]
SDC-$Ni_{0.95}La_{0.05}O$/ SDC/ SDC-SCC	97%CH_4-3%H_2O	500	0.15	0.75	[63]
Ni-YSZ/ YSZ/ GDC-LSCF	97%CH_4-3%H_2O	650	0.08	4	[64]

To determine the contribution of the Ru-Ni-doped CeO_2 catalyst, a comparison was made between cells with and without the anode reforming layer (Figure 19). The I-V-P curve of the ARL-containing cell shows significant peak power density increase in CH_4 fuel, 0.14 W/cm^2 compared to 0.10 W/cm^2. In addition, the I-V curve of the ARL-containing cell

shows a significant polarization loss at low current densities compared to the cell with the ARL, suggesting significant anodic polarization for the ARL-free cell. Clear differences were observed in the long term stability of the cells in methane, with the ARL-free sample degrading steadily in methane over 60 h until the cell became inoperable, while the power density of the ARL coated sample remained stable.

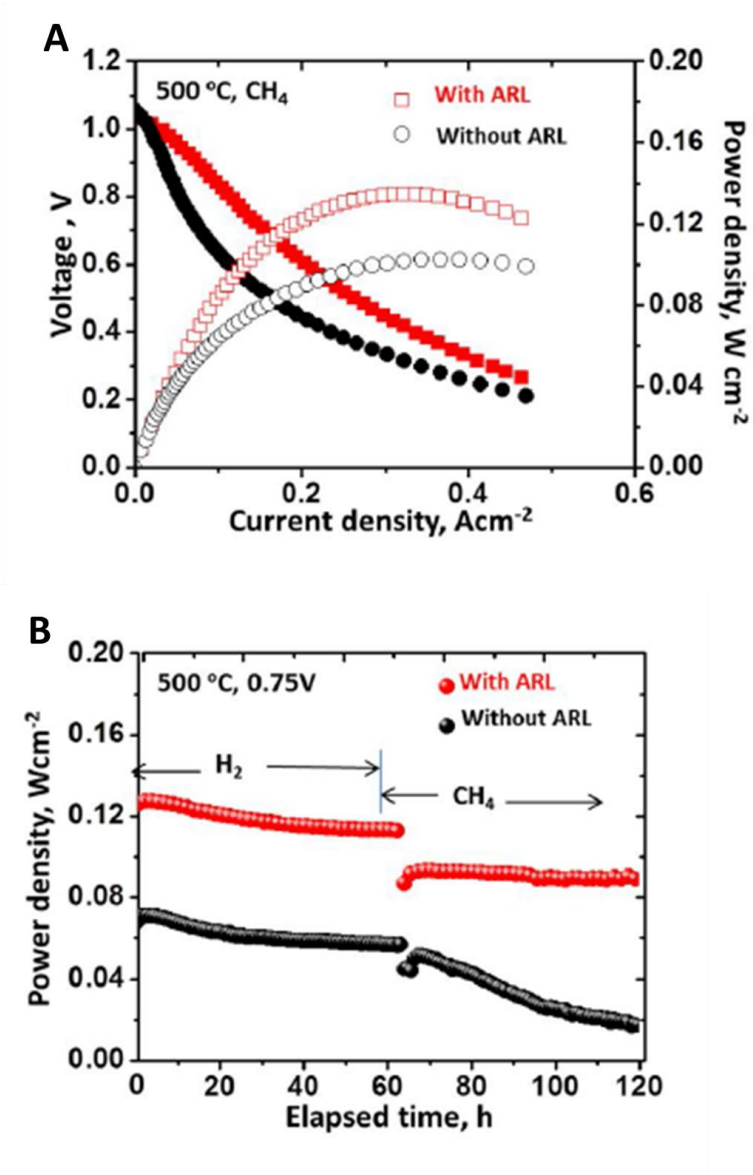

Figure 19 – P-I-V curves (a) and long-term testing (b) of SOFCs with and without the Anode Reforming Layer. Figure adapted from publication.[53] Note the difference

between data shown in fig 18 and fig 19 is due to the use of LSCF cathode rather than the electrospun fibers for the data shown in fig 19.

Post mortem analysis of the high-performance cell confirmed that no carbon was deposited after long term testing. Figure 20 shows top-down SEM images of the high performing SOFC after 250 h of operation in CH_4. Since the observation of coke can be subtle by SEM, a Ni-YSZ cell, representing the commercially available state-of-the-art anode material, was also run in CH_4. After only 24 h of operation, the Ni-YSZ cell carbon fibers were clearly visible on the Ni phase of the cermet anode, whereas the ARL coated Ni-BZCYYb cell did not show any evidence of carbon deposition by SEM.

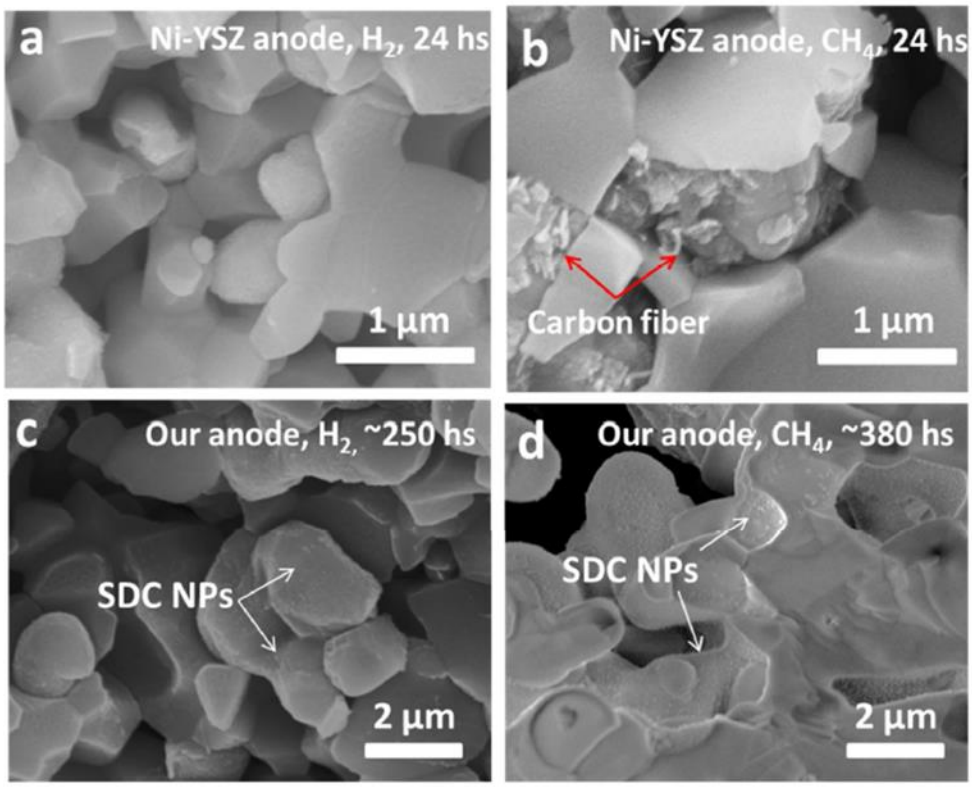

Figure 20 – Cross-section SEM of ARL coated Ni-BZCYYb (a,c) and ARL-free Ni-YSZ (b,d) after long term testing in H_2 and CH_4. Cross-sections were prepared from fractured samples. Figure adapted from publication.[53]

Raman analysis of the same two samples showed that the G band (1575-1620 cm^{-1}) and D band (1355-1380 cm^{-1}), indicative of graphitic carbon, were only observed on the Ni-YSZ samples after operation in CH_4. The ARL coated high performing SOFC did not show any carbon peaks, in fact the spectra of an ARL coated high-performing SOFC was nearly identical whether the cell was operated in H_2 or CH_4.

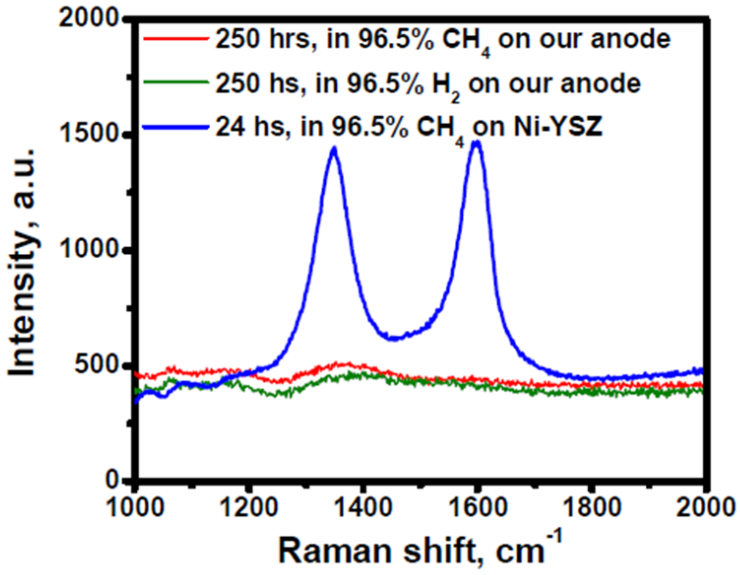

Figure 21 – Raman spectra collected from ARL coated Ni-BZCYYb (250 h) and ARL-free Ni-YSZ (24 h) anode support cross-sections after testing in H_2 and CH_4 fuels. Figure adapted from publication.[53]

As the anode reforming layer catalyst was identified as the critical component responsible for the high performance of the SOFC, and it is exposed to the most aggressive coking conditions (the lowest steam:carbon ratio occurs as the fuel enters the cell), coking on the ARL was a concern. Post-mortem XPS analysis of the catalyst (Figure 22) reveals two

important results. First, there was very little carbon signal (some adventitious carbon is expected for non-cleanroom samples) and the signal from the Ru and Ni active sites is clearly observed. If any carbon had been deposited at the active sites, the signal from the Ru and Ni would not be observed due to the high surface sensitivity of the soft-x-ray technique (only signal from the outermost 1-10 nm is detected by XPS). Therefore, the presence of clear Ru and Ni peaks confirm that no carbon was deposited during the cell operation. Second, the oxidation state of the Ru and Ni species remained cationic, even under the reducing conditions and relatively high temperatures of the anode; the oxidation state of the Ru and Ni will be further discussed in following sections.

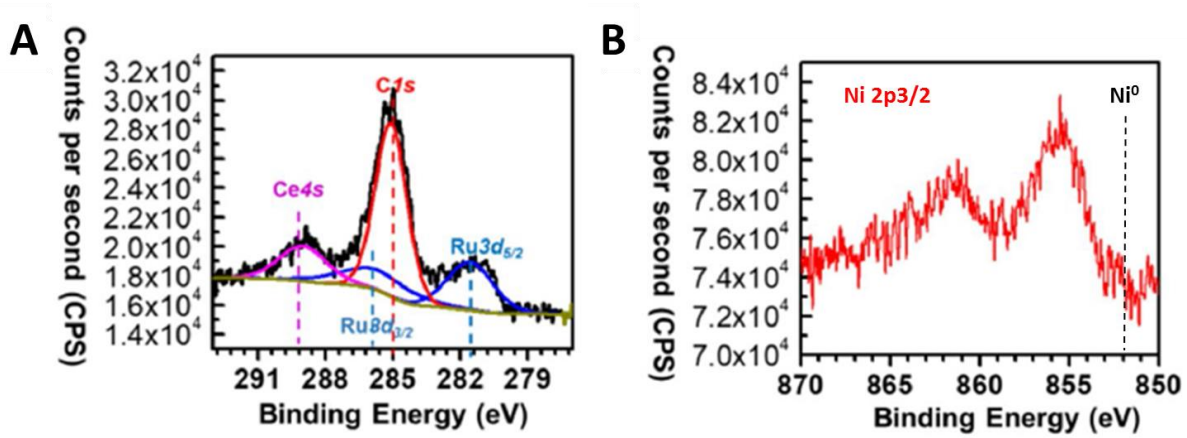

Figure 22 – High resolution XPS of the $Ru_{0.05}Ni_{0.05}Ce_{0.90}O_2$ anode reforming layer after 250 h of testing in CH_4 fuel. (a) Carbon 1s region (b) Ni 2p region. Data collected by Yu Tang at Kansas University, figure adapted from publication.[53]

Through SOFC device testing and basic post-mortem characterization, the following conclusions were made. First, this novel SOFC design (combination of PBSCF nanofiber

cathode, SDC electrolyte, Ni-BZCYYb anode, and Ru-Ni-CeO_2 ARL) was indeed able to achieve remarkable SOFC performance for direct methane operation at the low temperature of 500 °C. Second, the most critical component was identified as the $Ru_{0.05}Ni_{0.05}Ce_{0.90}O_2$ anode reforming layer, which dramatically enhanced both power density and long term stability. Third, there was no coking observed after testing on either the anode support or the ARL, which would experience the most aggressive steam:carbon ratio environment in the internally reformed cell. The performance of this device, and the critical nature of the ARL, necessitated the further characterization and mechanistic understanding of the Ru and Ni doped CeO_2, which is the focus of the remainder of this chapter.

4.6 Structural Characterization of Ruthenium doped CeO_2

4.6.1 Ex situ characterization of Ruthenium doped CeO_2

In order to understand the effect of each dopant the influence of Ru and Ni were investigated separately and compared. Ruthenium, being the most expensive dopant, and the most correlated with the high performance of the cell was investigated first.

The crystal structure and phase purity of Ruthenium doped powder were first investigated by X-ray Diffraction of the powders, using a zero-background plate and a 10% mass loading of Tungsten powder as a convenient reference. A large window scan (Figure 23) shows broad peaks corresponding to a nanocrystalline Fluorite structure (CeO_2) as well as very sharp peaks resulting from the tungsten reference (here marked with the '**#**' symbol). The XRD data suggest a single-phase material is produced, due to the absence of RuO_2 (rutile) or Ru (HCP) metal peaks in the scans. A higher resolution scan of the 2θ region including the highest intensity peaks for RuO_2 is also shown, with no evidence of RuO_2

signal even at the relatively high 10% Ru doping composition. One would reasonably expect that there would be a peak shift after any substitutional doping, and therefore high-resolution scans of the high 2θ region are included. Indeed, there is a small shift to higher angles as the Ruthenium content is increased. A shift to higher 2θ corresponds to a decrease in spacing (by Bragg's law), which is expected from addition of the relatively small Ruthenium cation. The results of a Reitfeld refinement of (courtesy of Ryan Murphy) the spectra show a shift from 5.413 Å to 5.402 Å for 0% Ru and 10% Ru, respectively.

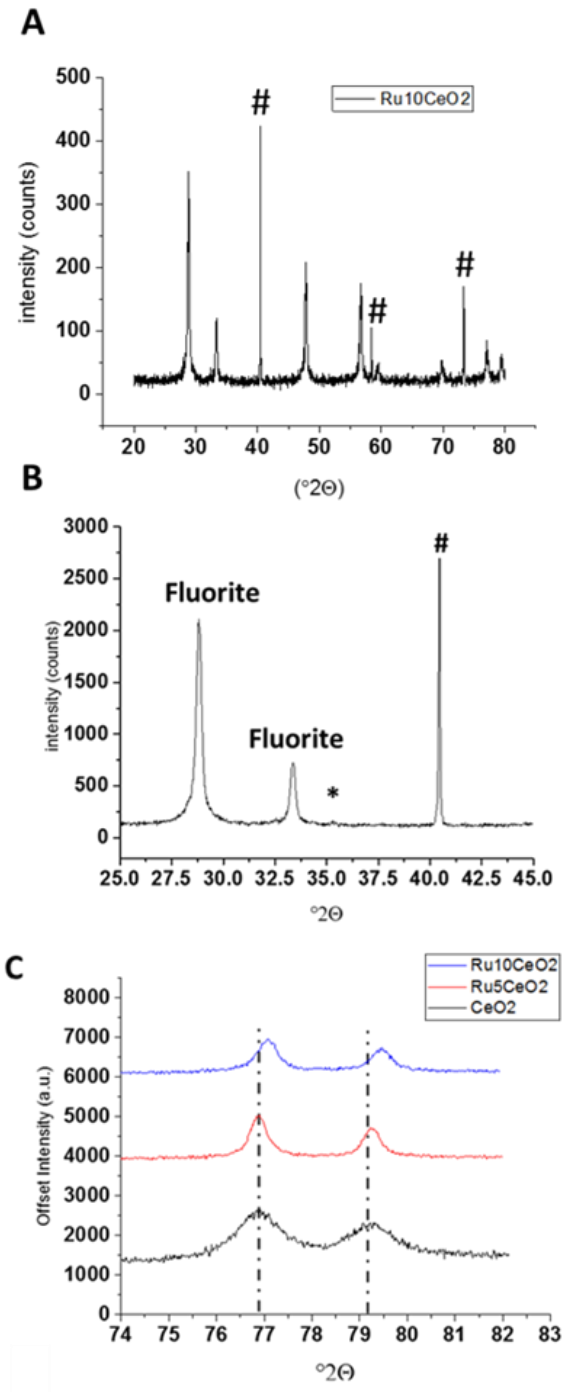

Figure 23 – X-ray Diffraction spectra of $Ru_xCe_{1-x}O_2$ collected using zero-background sample holder and tungsten reference powder (10% by mass loading, indicated by "#"). Low (A) and High (B) resolution scans of $Ru_{0.10}Ce_{0.90}O_2$, showing the presence of Fluorite (CeO_2) peaks, with no observation of RuO_2 rutile phase (35.0 °2θ). (C) High angle peak shifting as a function of Ru content, normalized to W peak position.

TEM analysis was also used to probe the composition and structure of the $Ru_xCe_{1-x}O_2$ particles. As shown in Figure 24, the majority of the particles were present as nanocubes, with the (100) facet exposed, although several smaller polycrystalline aggregates were also observed. Most importantly, no metallic Ruthenium or rutile RuO_2 secondary phases were observed on any of the particles. Energy Dispersive Spectroscopy (EDS) mapping shown in Figure 24(b-d) shows a homogeneous distribution of Ru throughout the particles, further suggesting the successful substitution of Ruthenium into the CeO_2 fluorite structure.

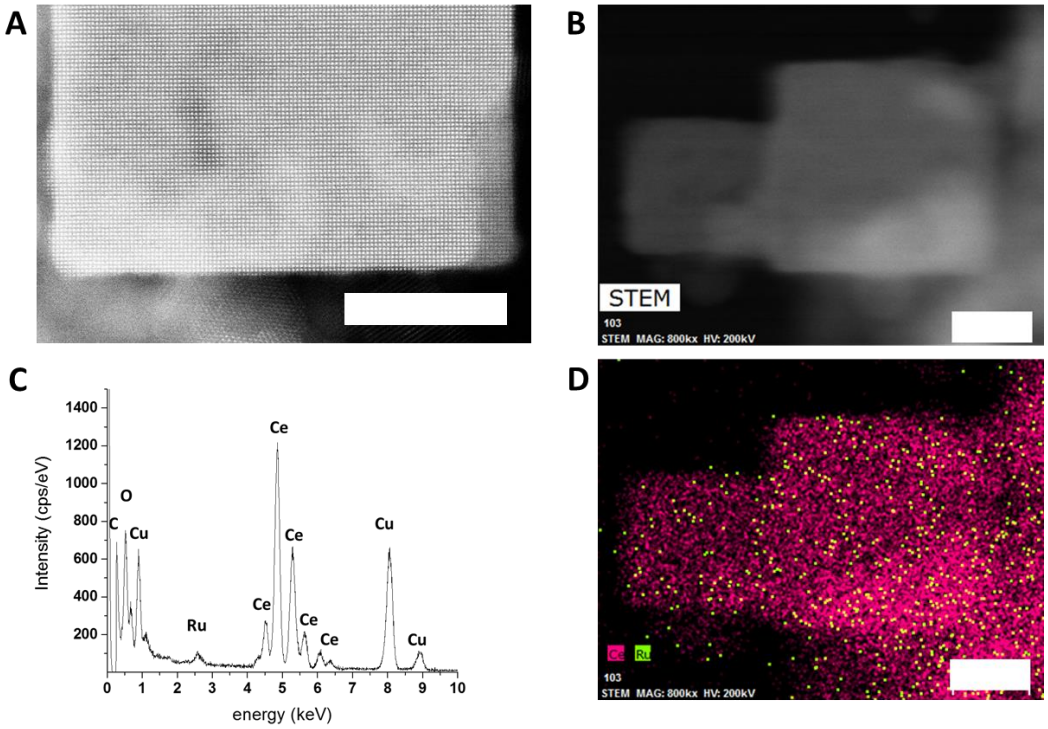

Figure 24: (A,B) representative TEM images of $Ru_{0.05}Ce_{0.95}O_2$ particles, (C, D) EDS spectrum and corresponding map collected from particle in (B), the green color in D is indicative of Ruthenium signal. Note that the Cu signal is from the Cu grid TEM support, not the sample. All scale bars are equivalent to 10 nm.

XPS analysis of the as-synthesized Ru doped CeO_2 sample is shown in Figure 25. Clear peaks corresponding to Ce, O and Ruthenium are easily observed on the sample surface, as well as a small peak from the Silicon substrate which was used to reference the peak positions. The adventitious carbon peak at 284.6 was not chosen as a reference due to the overlap from the Ruthenium 3d electron signal. The ratio of Ce:Ru atoms for a 5%-doped sample was measured as 83:17, which suggests an enrichment of Ru atoms near the surface of the particles.

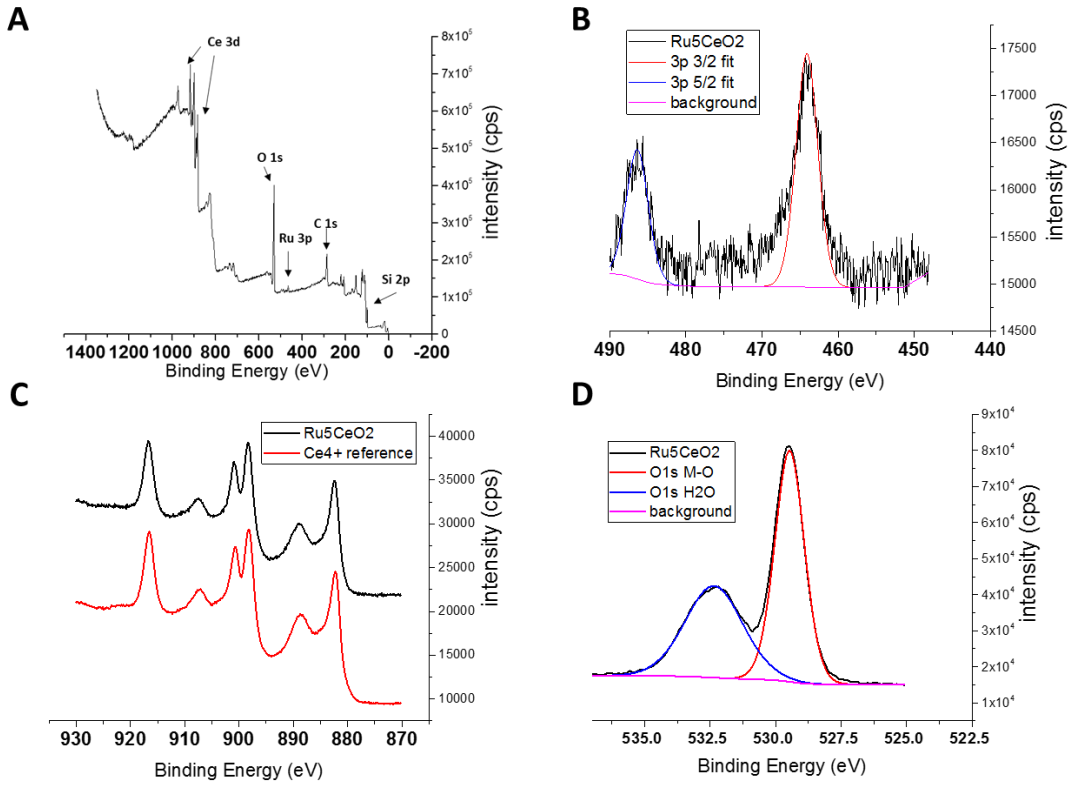

Figure 25: X-ray photoelectron Spectroscopy analysis of Ru0.05Ce0.95O2 samples, (A) survey spectra of $Ru_{0.05}Ce_{0.95}O_2$ sample (B) High resolution scan of Ru 3p region (C) overlay of $Ru_{0.05}Ce_{0.95}O_2$ 3d scan and reference 3d for Ce^{4+} (D) high resolution scan of O1s region, deconvoluted to show contribution of metal-oxygen bonding (red) and metal-hydroxyl bonding (blue).

The oxidation state of the Ru is clearly ionic, with a Ru3p binding energy 2.9 eV higher than metallic Ruthenium (464.1 eV compared to 461.2 eV, see Figure 25b). According to Morgan et al,[65] this value is most similar to the Ru^{3+} oxidation state present in $Ru(OH)_3$ (see values in Table 3).

Table 3: Measured and reference values for Ruthenium electron binding energies

	$Ru_{0.05}Ce_{0.95}O_2$	RuO_2	$RuCl_3$	$Ru(OH)_3$	Ru^0
3d 5/2	282.26	280.7	282.9	282.3	279.8
3p 3/2	464.1	462.6	464.1	464.1	461.2

High resolution scans of the Cerium 3d peak shows that the Cerium atoms are largely in the 4+ oxidation state (Figure 25c). This will be referenced in later Raman analysis explaining the presence of intrinsic oxygen vacancies observed in the material. The O 1s peak shows two distinct features: the peak at 529.5 eV corresponds to the Metal-Oxygen bonding, and the presence of a broad peak at 532.35 eV suggests the presence of strongly bound H_2O and OH groups. This suggests the Ru-doped material shows a strong affinity toward water, as the H_2O is not desorbed even under UHV conditions (<10^-8 Torr).

The cationic state of the Ruthenium dopant remained stable under operating conditions. In situ XANES and XPS spectra of the Ruthenium dopant, collected under steam reforming atmospheres (97% CH_4 3%H_2O) are shown in Figure 26. Clearly, the local bonding of the Ruthenium is dissimilar to that of the metallic reference, and the binding energy is significantly higher than that reported for the metallic state. Note that the shift in binding energy between 200 °C and 450 °C is due to the removal of bound hydroxyl species.

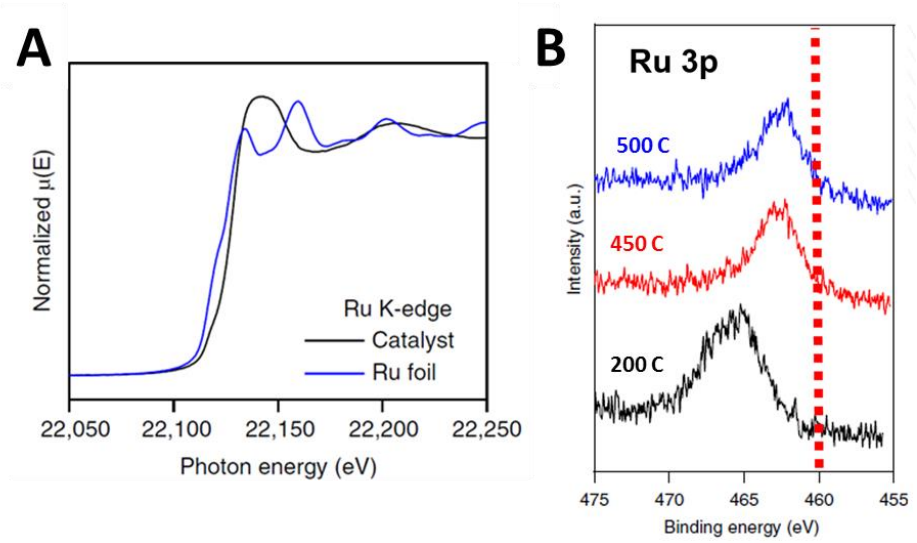

Figure 26 – (A) XANES spectra of Ruthenium doped CeO_2 and reference Ruthenium metal foil collected 200 °C under 97% CH_4 3%H_2O directly after testing at 500 °C. (B) Ambient Pressure XPS spectra of Ruthenium 3p collected at various temperatures under 97% CH_4 3%H_2O, with the B.E. of Ruthenium metal indicated by the dotted red line. Data collected by Yu Tang at University of Kansas, figure adapted from publication.[66]

4.6.2 Raman analysis of Ruthenium Doped CeO_2

Raman is ideally suited for the study of CeO_2 based materials due to the well-defined and highly active vibrational modes present, and the sensitivity of these vibrational modes to the CeO_2 defect structure. The peak assignments used in this work rely heavily on the analysis of Nakajimi et al, who provided one of the initial and most highly cited fundamental analyses of the Raman spectra for CeO_2.[67] The most intensive signal, a peak at 465 cm^{-1}, originates from the F_{2G} mode of $M^{4+}O_8$ vibrations within the fluorite lattice, representing the oxygen atoms around a Ce^{4+} cation with O_h symmetry. Two other important peaks originate at slightly higher wavenumbers resulting from defects in the fluorite structure; the α-peak is due to V_O^{**} formation and a $V_O^{**}O_6$-type configuration (also

O_h symmetry), and the β-peak results from the $M^{n+}O_8$-configuration which does not include an oxygen vacancy but includes a cationic dopant where *n* is less than four. As CeO_2 is reduced to $CeO_{2-\delta}$, V_O^{**} and Ce^{3+} species are formed, therefore the combination of the α and β peaks are commonly referred to as a broad 'Defect' peak, which is used as a measurement of the defect density of the CeO_2, as a ratio normalized to the F_{2G} peak intensity.[68,69] Trivalent dopants (e.g. Sm^{3+}, Y^{3+}, Gd^{3+}) are often added to increase the concentration of extrinsic oxygen vacancies in CeO_2, as the concentration of these dopants increases, the intensity of α and β peaks will increase, since each M^{3+} dopant requires the formation of an oxygen vacancy to satisfy the electroneutrality of the lattice. A representative Raman spectrum is shown in Figure 27 of CeO_2 and 20% Sm-doped CeO_2, in order to illustrate these fundamental Raman peaks.

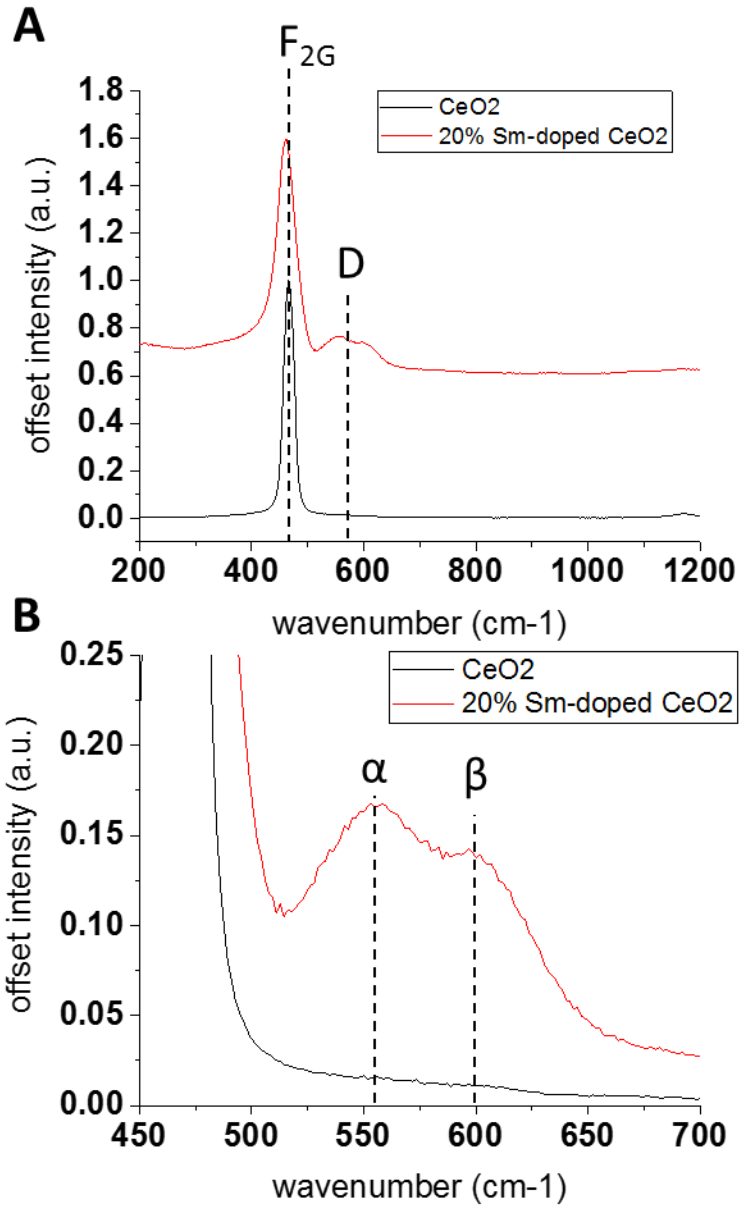

Figure 27: Representative spectra for polycrystalline CeO_2 (black) and $Sm_{0.20}Ce_{0.80}O_2$ (red) powders with illustration of key vibrational modes. The deconvolution of the characteristic defect "D-band" into it's constituent α and β peaks is highlighted in (B).

The Raman spectra for CeO_2 particles with increasing Ruthenium dopant concentration are shown in Figure 28. In addition to the F_{2G} peak and α/β defect peaks, there are several new

spectral features observed as Ruthenium is added. at ~329 cm^{-1}, ~702 cm^{-1}, and ~970 cm^{-1}. These features are not consistent with any possible secondary Ruthenium oxide phase, such as RuO_2 (522 cm^{-1}, 635 cm^{-1}, 703 cm^{-1}), RuO_3 (822-881 cm^{-1}), or RuO_4 (380-440 cm^{-1}).[70,71] In addition, a reference RuO_2 spectra was collected and compared to the Ru-doped CeO_2 spectra (under identical conditions) and intensities measured for the RuO_2 reference were negligible compared to the Ru-doped CeO_2 associated peaks. Therefore, the additional peaks present in Ruthenium doped CeO_2 can be assigned to structural distortions caused by the introduction of the Ruthenium into the CeO_2 fluorite lattice.

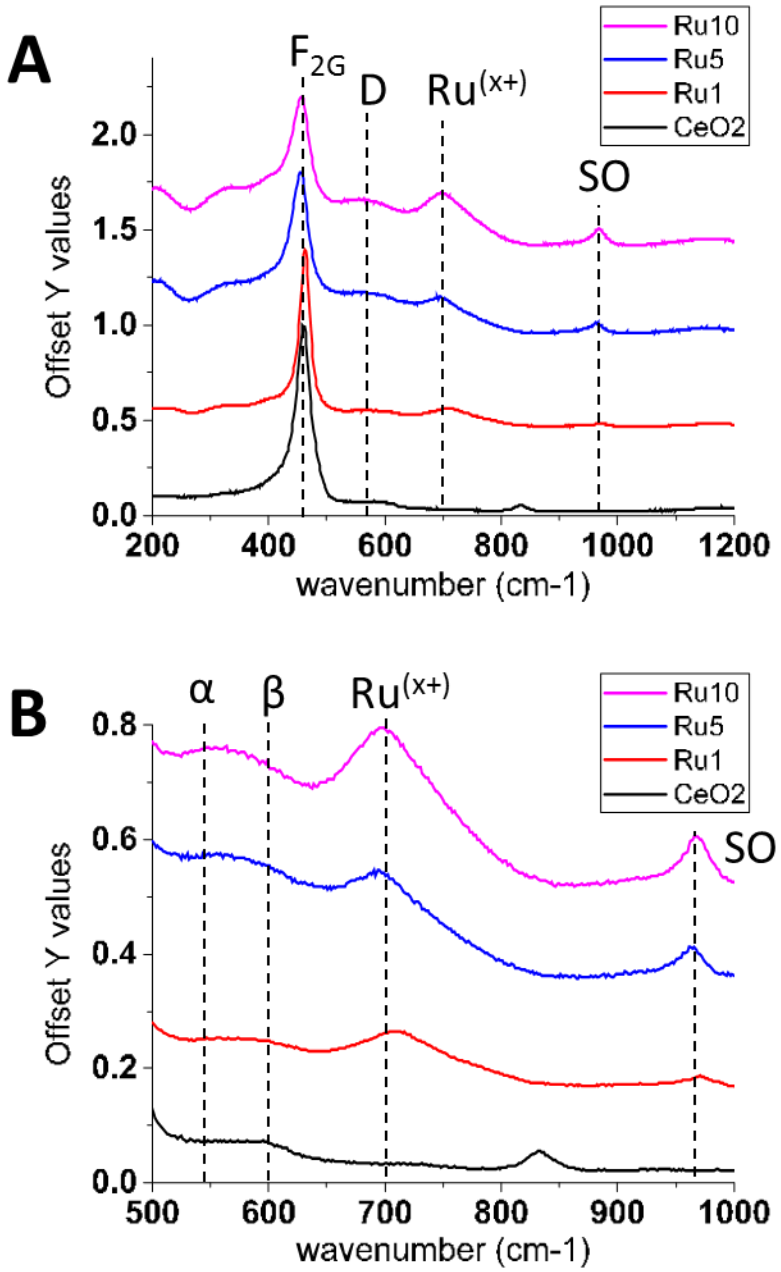

Figure 28 – Raman spectra collected for CeO_2 nanoparticles with Ruthenium dopant concentrations ranging from 0 to 10%. Spectra collected with 514 nm laser at 14 mW and normalized to the F_{2G} peak maximum. Spectra represent the average of signal from at least four separate locations on the powder sample.

These peaks have also been observed in the few other works which have used Raman spectroscopy to analyze Ru-doped and CeO_2 supported Ru catalysts showing Strong Metal

Support Interaction (SMSI).[72-75] These works have attributed these bands to bonding between the Ruthenium and Ceria, the band near 700 cm^{-1} is ascribed to the asymmetric stretching of Ru-O-Ce bonds, which occur when Ruthenium is substitutionally doped into a Ce^{4+} site or supported as a single atom on the CeO_2 surface. The Ru associated peak between 940 and 980 cm^{-1} is not well defined but has been associated with the formation of surface peroxide groups, which can be stabilized at mobile oxygen vacancies or bridged between surface Ce and Ru cations. It is possible that the peak at ~700 cm^{-1} is related to the CeO_2 β peak, since the relatively lower mass of the Ru^{3+} cation would be expected to shift the $M^{3+}O_8$-type vibration to higher wavenumbers, compared to Ce^{3+} or the heavier trivalent dopants (e.g. Sm^{3+}) mentioned above. The observation of a D band (α and β peaks between 540 cm^{-1} and 600 cm^{-1} concurrent with the 700 cm^{-1} and 980 cm^{-1} shows that the presence of Ruthenium in the lattice results in the formation of extrinsic oxygen vacancies, suggesting that the oxidation state of the Ruthenium is less than four, or that the presence of Ru^{n+} in the lattice causes the reduction of Ce^{4+} to Ce^{3+}. For the remainder of this work, the Raman band at ~700 cm^{-1} will be labeled as "Ru(x+)," and the band at ~980 cm^{-1} will be labeled as "surface oxide" or "SO" representing the presence of Ru-O-Ce bonding present in the doped CeO_2 catalyst.

The dependencies of the Ru(x+) and SO peaks on Ruthenium doping concentration are quantified in Figure 29. In order to consistently compare the relative contribution of different peaks, all intensity values were normalized to the CeO_2 F_{2G} peak, following the approach of similar works.[67,72,74] Clearly the presence of Ruthenium dopants affects the Raman spectra of the CeO_2 based catalyst, and these affects scale with amount of dopant. As Ruthenium is added, the peaks associated with oxygen vacancies and Ru-O-Ce bonding

increase. Further discussion of these peak assignments will be included along with the new information gathered from the experiments detailed in further sections.

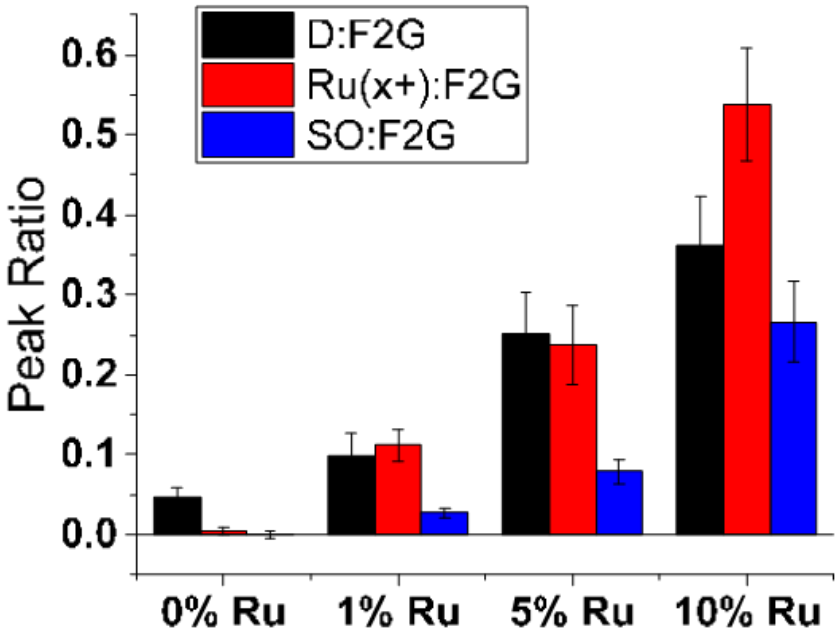

Figure 29 – Chart of Defect (D), $Ru^{(x+)}$ (ionic Ruthenium), and Surface Oxide (SO) peak ratios for samples with varying dopant concentration. Values were collected from spectra normalized to the F_{2G} peak of CeO_2. Error bars represent one standard deviation of data collected from at least four samples.

Clearly, the presence of these peaks is dependent on the amount of Ru doped into the lattice, and the presence of Ru(+) and SO peaks are associated with an increase in oxygen vacancies in the CeO_2 lattice ($D:F_{2G}$ ratio).

To form a basic structure-property relationship between these Ruthenium dopant features and catalyst activity, a steam reforming experiment was conducted. $Ru_xCe_{1-x}O_2$ samples were placed in a fixed bed flow reactor coupled to a gas chromatograph, courtesy of Yu Tang in Prof. Tao's group at the University of Kansas (Figure 30).

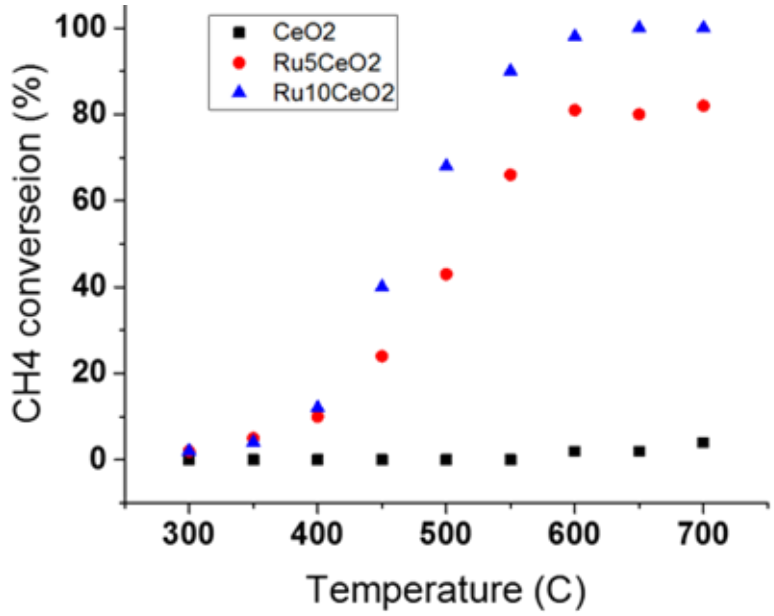

Figure 30: Conversion of methane over a fixed bed of Ru-doped CeO2 with 3:2 H2O:CH4 fuel stream. 50 mg of sample was mixed with 300 mg of purified quartz and effluent stream was monitored via gas chromatography. (Data collected by Yu Tang at Kansas University)

Although CeO_2 itself is a well-known hydrocarbon oxidation catalyst, the addition of the Ruthenium dopant dramatically improved the steam reforming performance, and the activity scaled with the concentration of Ruthenium dopant. Therefore, there is a clear correlation between the amount of ionic Ruthenium and ionic Ruthenium associated defects (observed by Raman spectroscopy) and steam reforming performance in this system.

The combination of XRD, TEM, EDS, XPS and Raman experiments support the following claims made for this Ruthenium doped CeO_2 material. First, Ruthenium was substitutionally doped into the Fluorite structure and created extrinsic oxygen vacancies and is therefore in an oxidation state greater than zero and less than four. Second, the

amount of Ruthenium dopant was directly associated with the relative number of observed defects in the CeO_2 fluorite structure (e.g. intrinsic oxygen vacancies, surface peroxides, and Ru-O-Ce bonding). The remaining sections focus on the dynamic behavior of these Raman active features, and relationships between these features and observed performance of the catalyst.

4.6.3 In situ Raman analysis of Ruthenium doped CeO_2

In situ experiments are critical for understanding the structural influence on catalytic performance under operating conditions. In this section, in situ experiments are used to show that the defect structure and surface chemistry of Ru-doped CeO_2 is dynamic under operating conditions, and that these changes are directly related to the catalytic performance of the material.

4.6.3.1 Enhanced in situ generation of vacancies due to Ru-O-Ce bonding

Raman spectra collected at 500 °C (the target operating temperature of the high performing SOFC) under H_2 atmosphere is shown in Figure 31. Under these conditions, the characteristic peaks for Ru-O-Ce bonding and surface oxygen species (bands at 640-740 cm^{-1} and between 960 and 980 cm^{-1}, respectively) are removed. In addition, there is a slight shift of the F_{2G} peak from 457 to 448 cm^{-1} (-9cm^{-1}), and the ratio between the D and F_{2G} peaks, both representative of the formation of intrinsic oxygen vacancies, are increased.

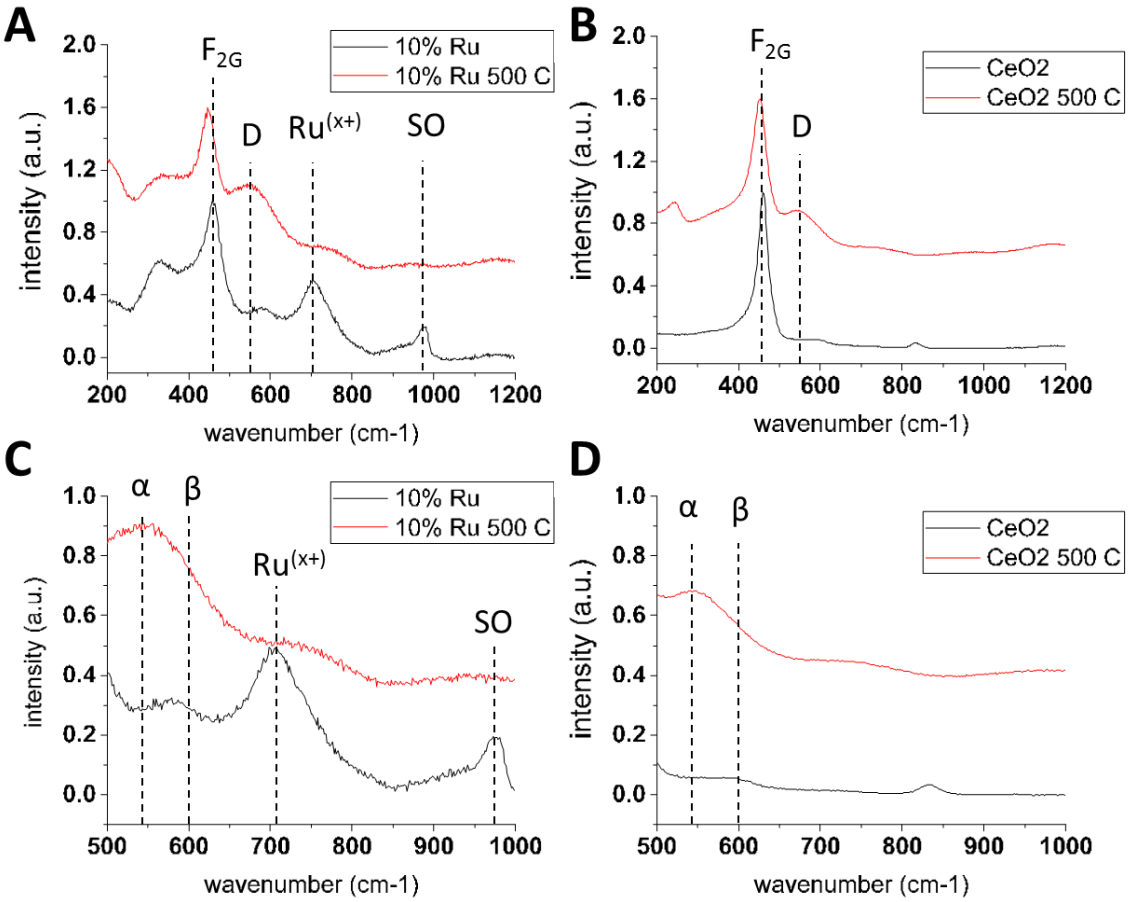

Figure 31: in situ Raman spectra for Ru-doped (A,C) and un-doped (B,D) CeO_2 nanoparticles. Red lines represent spectra acquired while holding the stage at 500 °C in 40 sccm H_2 humidified with 3%H_2O. All spectra are normalized to the F2G peak. Dotted lines are shown to guide the eye to changes in key peak positions and relative intensities

The shifting F_{2G} peak and increased defect band are expected for non-stoichiometric $CeO_{2-\delta}$ as Ce^{4+} is reduced to Ce^{3+} but the degree to which the Ru-doped catalyst is reduced is much greater than the pure CeO_2 case both at room temperature and in H_2 at 500 C. This affect is quantified in Figure 32. The intensity ratio (D:F_{2G}) of the Ru-doped sample is much larger than the undoped sample. In addition, the shift of the F_{2G} peak under H_2 for

the CeO_2 sample is 460.2 to 454.7 cm^{-1} (-4.5 cm^{-1}), which is half the magnitude of that observed for the Ru-doped samples. The greater F_{2G} shift and lower peak ratios are measures of enhanced reducibility at this temperature, and a greater concentration of oxygen vacancies formed by H_2 exposure.

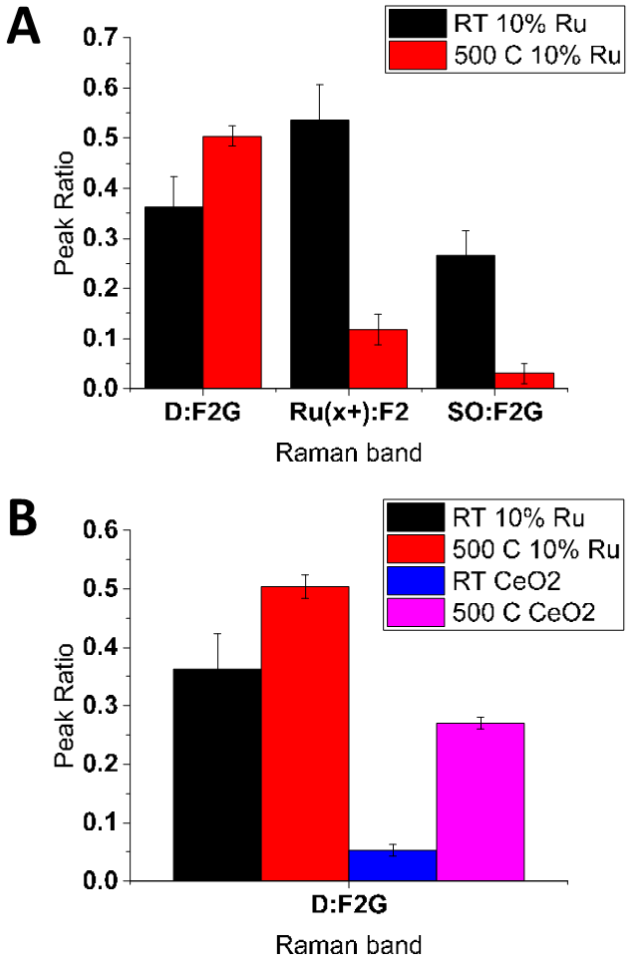

Figure 32 – (A) Chart of Defect (D), Ru(x+) (ionic Ruthenium), and Surface Oxide (SO) peak ratios for a 10% Ru doped sample collected at room temperature and at 500 C under H_2. (B) Comparison of D:F_{2G} ratios at RT and 500 C in H2 for undoped and 10% Ru-doped CeO_2. Values were collected from spectra normalized to the F_{2G} peak. Error bars represent one standard deviation of data collected from at least four samples.

The amount of Ruthenium dopant determines the degree of this enhanced reduction. As shown in Figure 33, the ratio (I_D:I_{F2G}) under reducing atmosphere at 500 °C is lower for the 5% Ru sample than the 10% Ru sample.

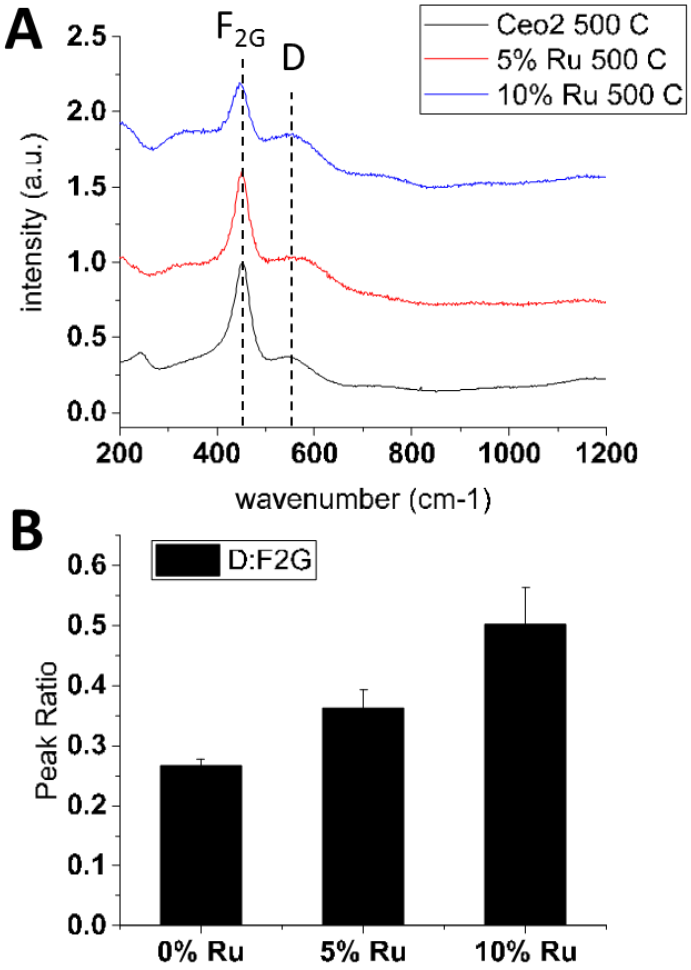

Figure 33: In situ analysis of Ru-doped CeO2 at 500 °C in humidified (3%H_2O) H_2 atmosphere. The spectra in are presented in A, the D:F2G peak ratios are quantified in B. Error bars represent one standard deviation of ratios collected over four positions on the powder samples.

This in situ analysis clearly shows that the initial presence and relative magnitude of the of the Ru-O-Ce associated peaks predicts the presence and magnitude of $CeO_{2-\delta}$ defect species under in situ conditions (H_2 atmosphere, 500 C). It is likely that the Ru-O-Ce bonding reduces to Ru-[V_O]-Ce under hydrogen, forming active oxygen vacancy sites. The activity and role of these active sites will be discussed in a later section along with DFT simulation results.

4.6.3.2 Thermal stability of Ru-O-Ce bonding and relation to performance

Although enhanced reducibility is well-known predictor of catalytic activity for several CeO_2 supported catalysts, direct relationship between the observed Ru-O-Ce structural features and catalytic properties must be made. The previous section showed that the presence of Ru-O-Ce bonding predicts enhanced reducibility of the CeO_2 support, but questions remain concerning the presence and role of any metallic Ru^0 NPs which are reasonably expected to form at elevated temperatures. Raman analysis supports the stability of the ionic Ru, and its ability to enhance the reduction of the CeO_2 bulk, at 500 °C, but at higher temperatures it is reasonable to expect exsolution of the Ru to the surface and the precipitation of metallic Nanoparticles. As Ruthenium cations are converted to metallic ruthenium nanoparticles, the concentration of Ru-O-Ce type bonding will decrease (limited only to the interface between the Ru particles and the CeO_2 support). Therefore, with the goal of producing two samples with identical composition but different surface chemistry (different concentrations of Ru-O-Ce bonding), $Ru_{0.05}Ce_{0.95}O_2$ powder was treated to two separate brief high temperature reductions 900 °C, 2 h, 4% H_2/Ar, and 500 °C, 2 h, 4% H_2) and these two groups were

Indeed, after the high temperature reduction the CeO_2 particle morphology was relatively unchanged, but several Ruthenium nanoparticles exhibiting metallic (HCP) crystal structure were observed on the sample which were not observed on samples tested at 500 °C, as shown by high resolution TEM and EDS mapping of each sample (Figure 34).

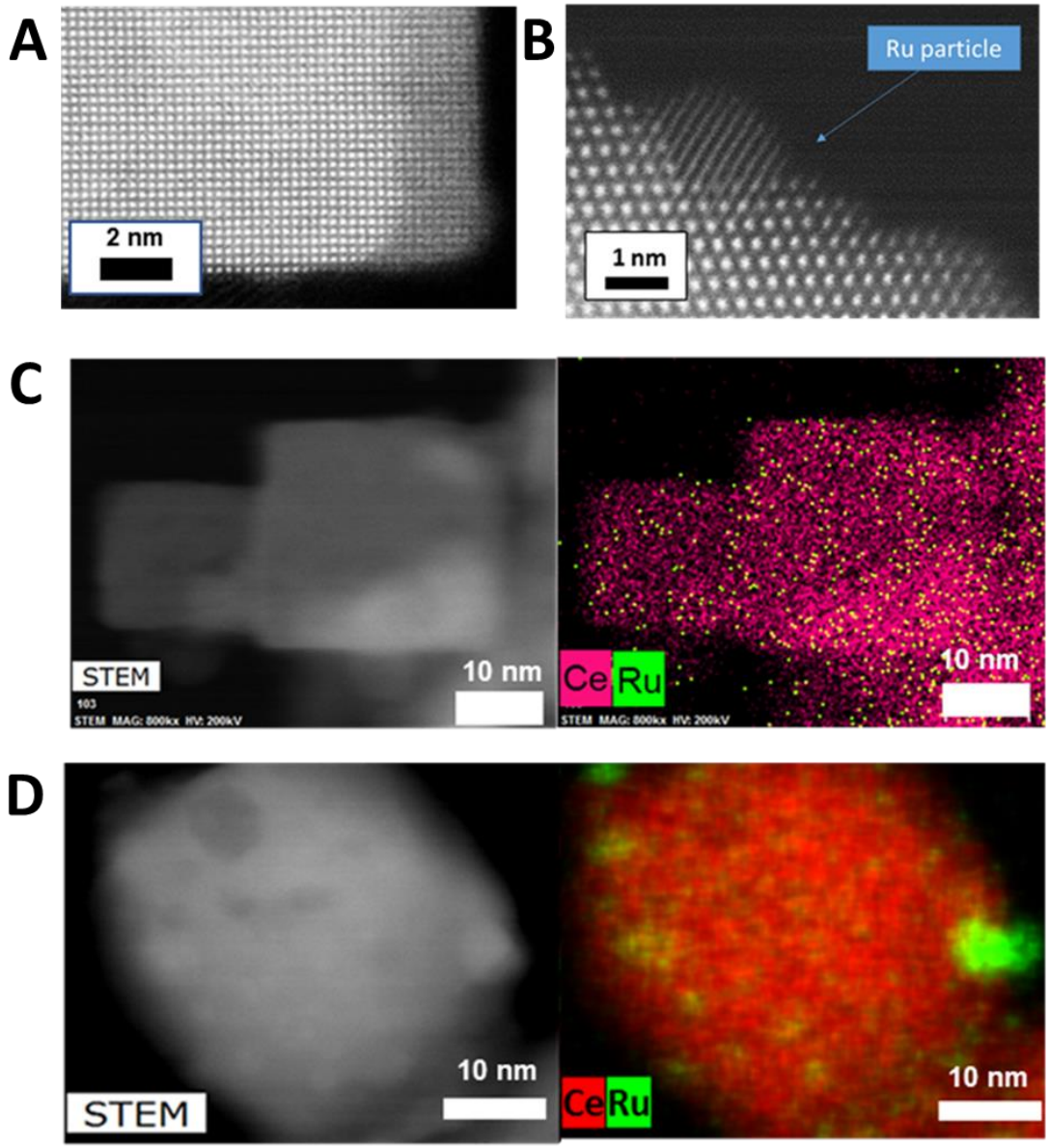

Figure 34: Aberration corrected HRTEM of the $Ru_{0.05}Ce_{0.95}O_2$ sample after exposure to (A) 500 C, 4%H_2/Ar, 2 h and (B) 900 C, 4%H_2/Ar, 2h. A STEM image and the corresponding EDS maps for the 500 C and 900 C samples are shown in (C) and (D) respectively.

In addition to the newly observed metallic nanoparticles on the surface, the chemical state of the Ruthenium was altered by the higher temperature treatment as well. As shown in

Figure 35, the reduction treatment shifts the B.E. of the Ruthenium 3p electrons ~1.55eV (464.1 eV – 462.56 eV). Although metallic Ruthenium was observed in the HR-TEM images, the observed BE on the sample were still higher than that expected for pure Ru^0 (461.2 eV). This can possibly be explained by an electronic interaction which remain between the CeO_2 support and metallic Ruthenium NPs, due to the relatively high number of Ru/CeO_2 interface that exists between the precipitated Ruthenium nanoparticles and the CeO_2. Regardless, there is a significant shift in both the Ru 3p and 3d peaks towards a lower BE for precipitated Ru/CeO_2 compared to the as-synthesized Ru-doped sample.

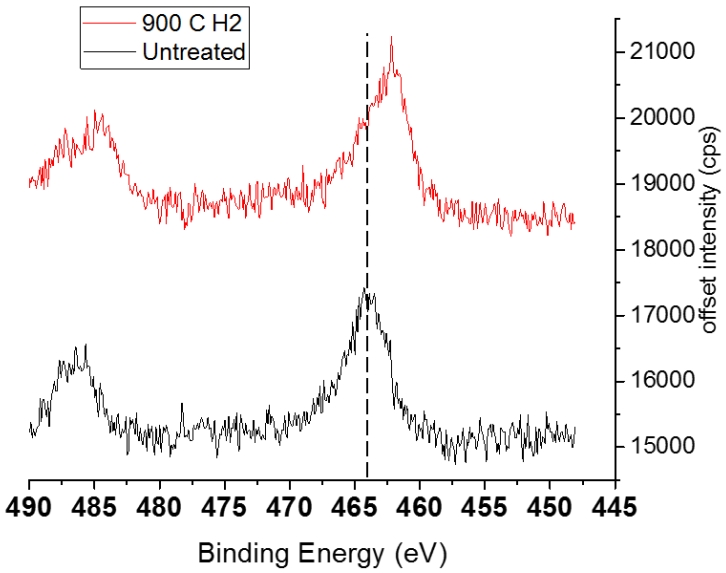

Figure 35: XPS analysis of Ru 3p peak for a Ru0.05Ce0.95O2 sample before (black) and after (red) exposure to high temperature reduction treatment (900 °C, 4%H2/Ar) . Both peaks are referenced to the elemental Si 2p peak (powders were placed on a Si wafer for this reason).

In addition, the Raman spectra affiliated with the Ru-dopant are absent in the high temperature treated, Ru-precipitated sample. A comparison between the room temperature

Raman spectra of Ru "doped" (treated to 500 C in H_2) and Ru "precipitated" (treated to 900 C in H_2) samples are compared in Figure 36. There is a small defect peak, as expected for CeO_2 exposed to these conditions, but the features at, ~700 cm^{-1} and ~980 cm^{-1} are absent after the high temperature reduction.

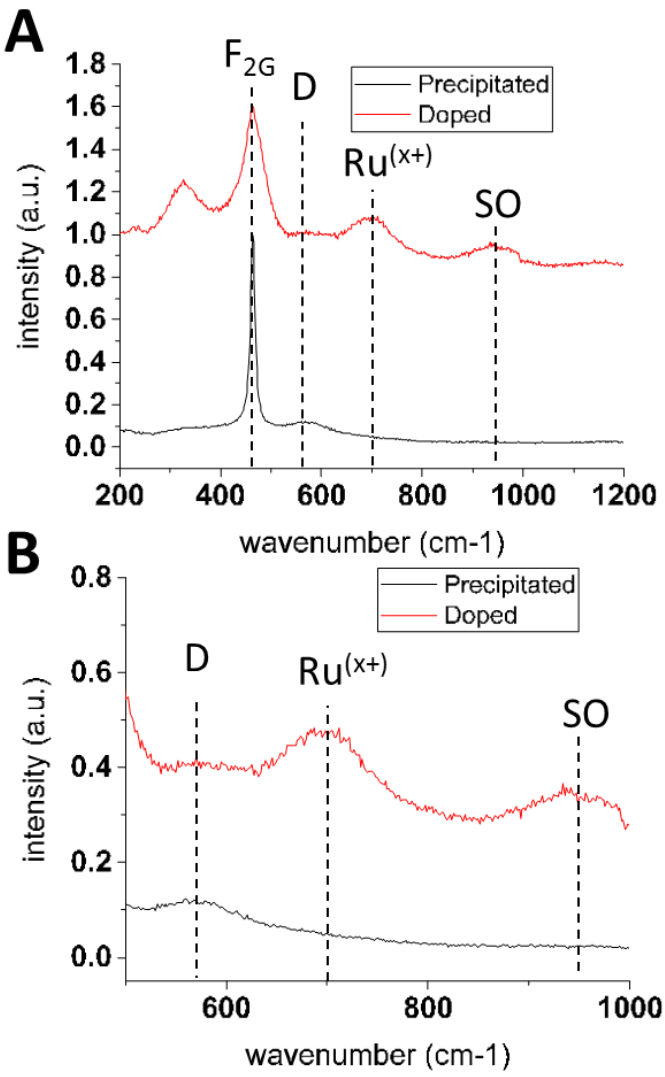

Figure 36 – Raman spectra collected at room temperature in ambient air $Ru_{0.05}Ce_{0.95}O_2$ samples as synthesized (red) and after a previous reduction treatment to form Ru0 particles on the surface (black). Data shown has been normalized to the F_{2G} peak

The presence of precipitated Ru^0 nanoparticles also affected the Raman spectra observed in situ, relative to the Ru-doped samples. Samples with exclusively ionic Ru species, showed much higher D:F_{2G} peak ratios, and therefore showed increased formation of oxygen vacancies and Ce^{3+} (Figure 37). As before, the ionic Ruthenium associated bands (640-740 cm^{-1}) and surface oxygen bands (960-980 cm^{-1}) were removed as the sample was heated in H_2, while the D band increased, relative to the main F_{2G} CeO_2 peak. The sample with the precipitated Ruthenium particles showed little evidence of ionic ruthenium associated bands, and a much lesser degree of reduction upon heating to 500 °C.

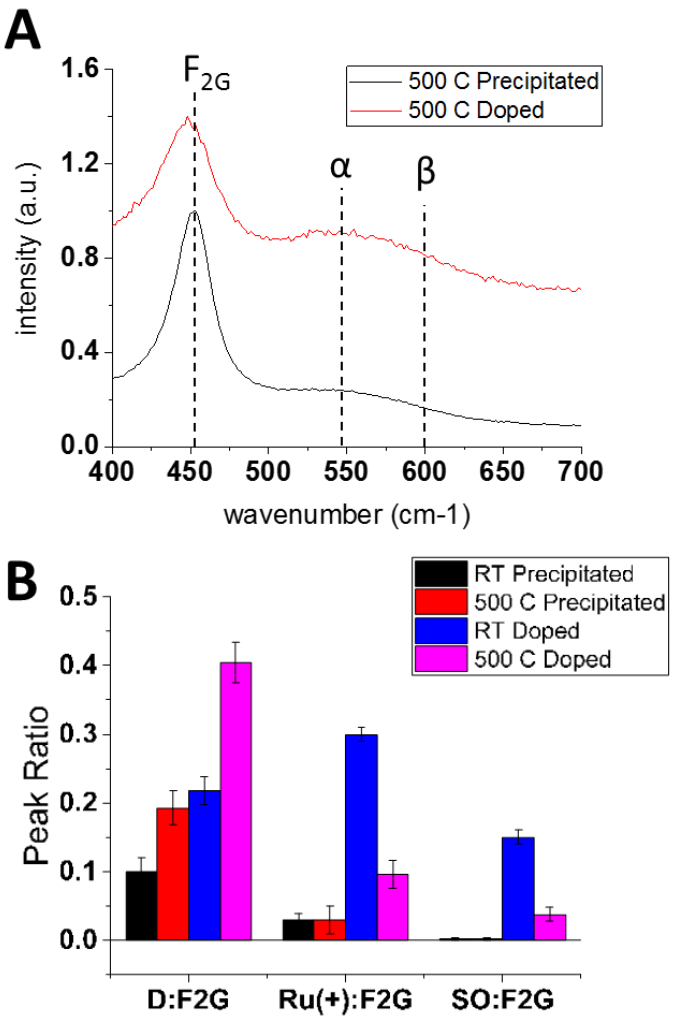

Figure 37 – (A) Raman spectra collected at 500 °C in H_2 for $Ru_{0.05}Ce_{0.95}O_2$ samples as synthesized (red) and after a 900 C reduction treatment (4%H_2/Ar) to form Ru^0 particles on the surface (black). (B) Peak ratios collected from at least four locations on each sample, error bars represent one standard deviation.

Next, while the Ru-doped and Ru-precipitated samples were held at 500 °C, the atmosphere was cycled between H_2 and Ar, both humidified to 3% H_2O. A clear difference was observed between the Ru-precipitated and Ru-doped samples, in that the Ru-O-Ce bands (640-740 cm^{-1}) and associated surface oxygen band (960-980 cm^{-1}) were regenerated in the Ru-doped sample when exposed to the oxidizing humidified Ar, whereas these bands were entirely absent in the Ru^0 precipitated sample and only the D band was variable with the

atmosphere (Figure 38). Only the doped material was able to regenerate the Ru-O-Ce bonding through reaction with the steam, whereas the bands were irreversibly removed in the sample with the precipitated metallic Ru nanoparticles.

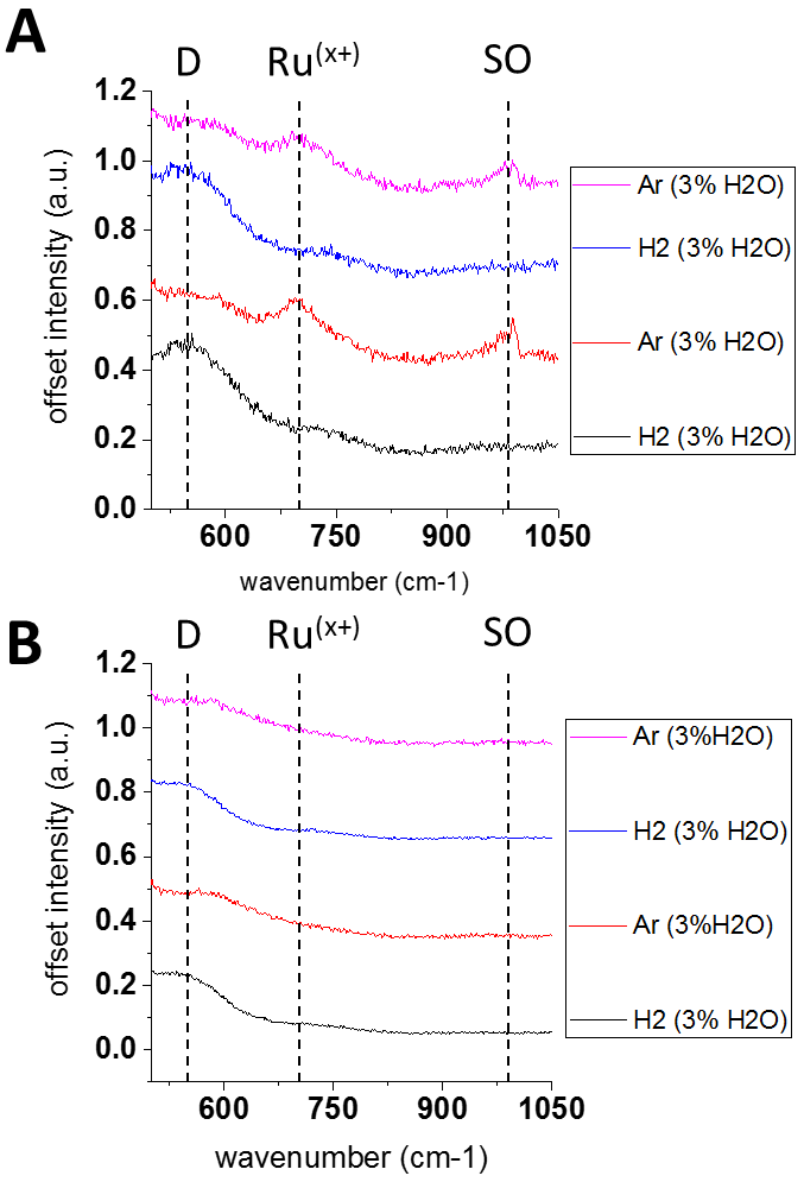

Figure 38 – Raman spectra collected at 500 °C while cycling between 3% H_2O humidified H_2 and Ar atmospheres. Spectra in (a) were collected from the as-synthesized, $Ru_{0.05}Ce_{0.95}O_2$ powder, whereas spectra in (b) were collected from an aliquot of that powder that had been exposed to 4%H_2 at 900 °C for 2 h, forming metallic Ru nanoparticles on the CeO_2 surface. The powders were equilibrated for 30 min in each atmosphere before spectra were collected.

From this experiment several claims can be made. First, the spectral features assigned to Ru-O-Ce are largely removed by exposure to a short high temperature reduction treatment (2 h in 4% H_2 at 900 °C) which causes the precipitation of metal Ru nanoparticles on the surface of the $Ru_xCe_{1-x}O_2$ material. Second, the lack of Ru-O-Ce associated Raman features was correlated to a lower relative intensity of the CeO_2 defect peak when under operating conditions (500 C, H_2). Therefore, metallic Ru nanoparticles are not as effective as ionic Ruthenium dopants in enhancing the formation of oxygen vacancies in CeO_2. This analysis suggests that the more Ru-O-Ce bonding that is present in the material, the more reducible the material will be at intermediate temperatures, and the more effective the catalyst. Indeed, the steam reforming performance of the precipitated Ru/CeO_2 sample is markedly decreased compared to the doped, $Ru_{0.05}Ce_{0.95}O_2$ sample (Figure 39).

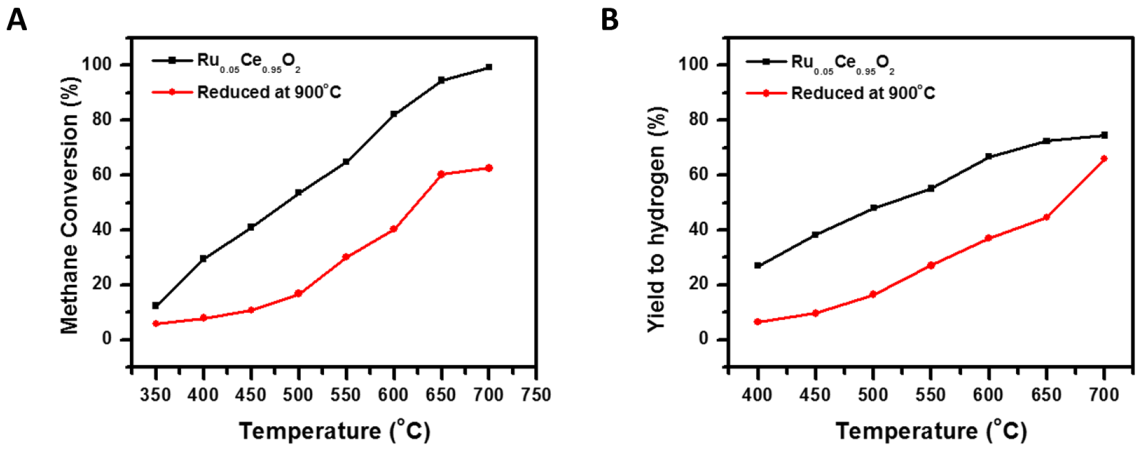

Figure 39: Methane conversion (A) and % Yield to Hydrogen (B) under steam reforming conditions (3:2 H_2O:CH_4 ratio) comparing Ru-doped and Ru-precipitated samples. (Data collected by Yu Tang at Kansas University)

It's important to note that high temperature treatments are commonplace in SOFC fabrication (e.g. sintering Ag paste connections, sintering glass seals, NiO reduction, and electrode sinter-bonding), so this result has immediate relevance to the implementation of ionic Ruthenium catalysts in SOFCs. To preserve the high activity ionic species, the catalyst must be added to the assembly after such high temperature treatments, or the processing temperatures may need to be lowered for optimized ARL performance.

4.7 Synergistic effect of Nickel co-dopant in $Ru_xCe_{1-x}O_2$

4.7.1 Thermal catalysis of $Ru_xCe_{1-x}O_2$, $Ni_xCe_{1-x}O_2$, and $Ru_xNi_yCe_{1-x-y}O_2$

During initial steam reforming screening experiments conducted by collaborators at Kansas University, it was observed that a combination of Ruthenium and Nickel dopants was more effective than a molar equivalent of pure Ruthenium or Nickel doped into the CeO_2 catalyst. Figure 40, shows that the catalytic performance, as quantified by CH_4 conversion and Turn-over-frequency (per Ni and Ru atom) of the Ruthenium doped CeO_2 is higher than that of the Ni doped CeO_2, and made higher still by replacing half the Ruthenium atoms with Nickel dopants.

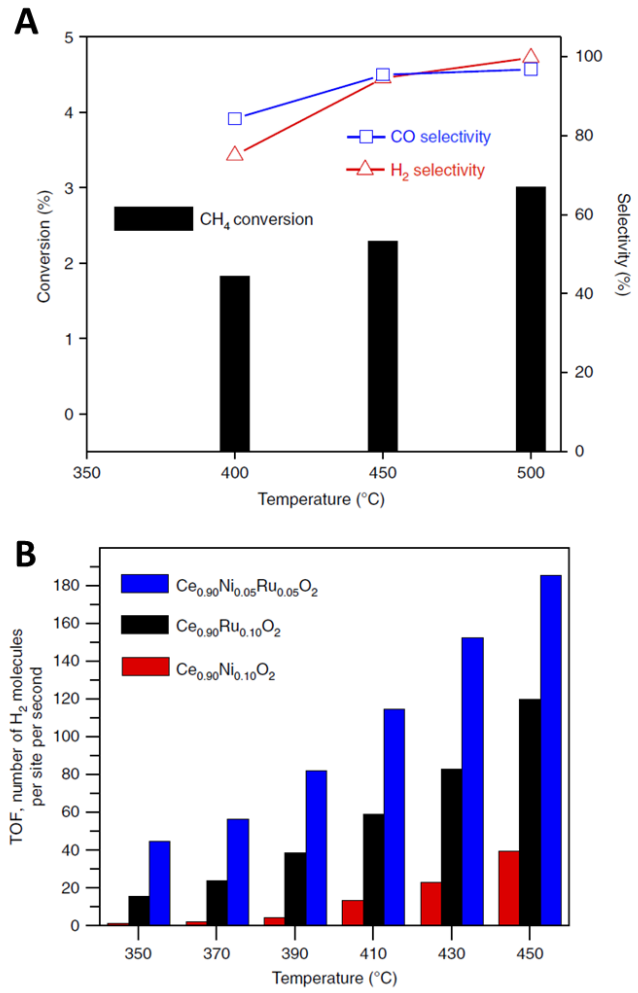

Figure 40 – (a) CH_4 conversion with selectivity to H_2 and CO, and (b) Turn-over-frequency of steam reforming reaction for singly doped and co-doped Ru-Ni-CeO_2 catalysts with molar equivalent doping concentration. (Data collected by Yu Tang at Kansas University), figure adapted from publication.[53]

In addition, the activation energy of the catalysts was variable between the Ru, Ni, and co-doped catalysts, with the lowest E_a for the co-doped case (Figure 41). Even though the Ni doped catalyst showed only modest activity on its own, it was able to significantly promote the activity of the Ruthenium doped catalysts (as measured by CH_4 conversion, TOF, and E_a). The remainder of this section explores this promotion effect, keeping in mind the results of the previous analyses of the Ruthenium doped case.

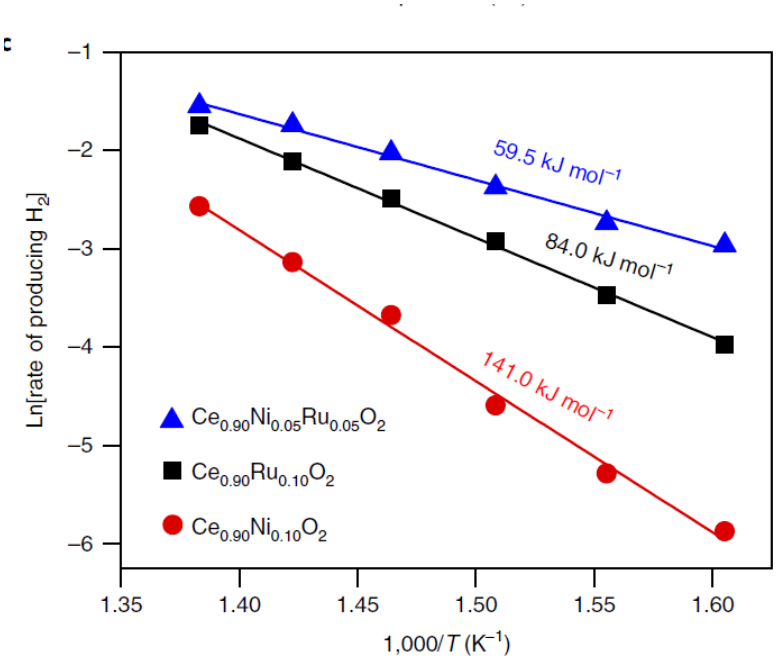

Figure 41 – Arrhenius plot of H_2 production rate, with activation energy (calculated from linear fit slope), for singly doped and co-doped Ru-Ni-CeO_2 catalysts. Data collected by Yu Tang at Kansas University, figure adapted from publication.[53]

4.7.2 Materials Characterization of Ni and Ru-Ni co-doped CeO_2

First, in a similar fashion to that used for the Ruthenium doped CeO_2 analysis, a basic materials characterization was made for the substitutional doping of Ni cations into CeO_2. Again, there was no evidence of secondary phase formation (Figure 42). Significant peak shifting observed in XRD suggests that the Ni is indeed substitutionally doped into the CeO_2 bulk, contracting the lattice CeO_2 parameter. Similarly, XPS analysis of the Ni dopant shows that the Ni is clearly non-metallic, and most similar to a (II) oxidation state. TEM analysis of the particles confirmed that only single-phase nanoparticles were present, with no evidence of metallic Ni or secondary NiO.

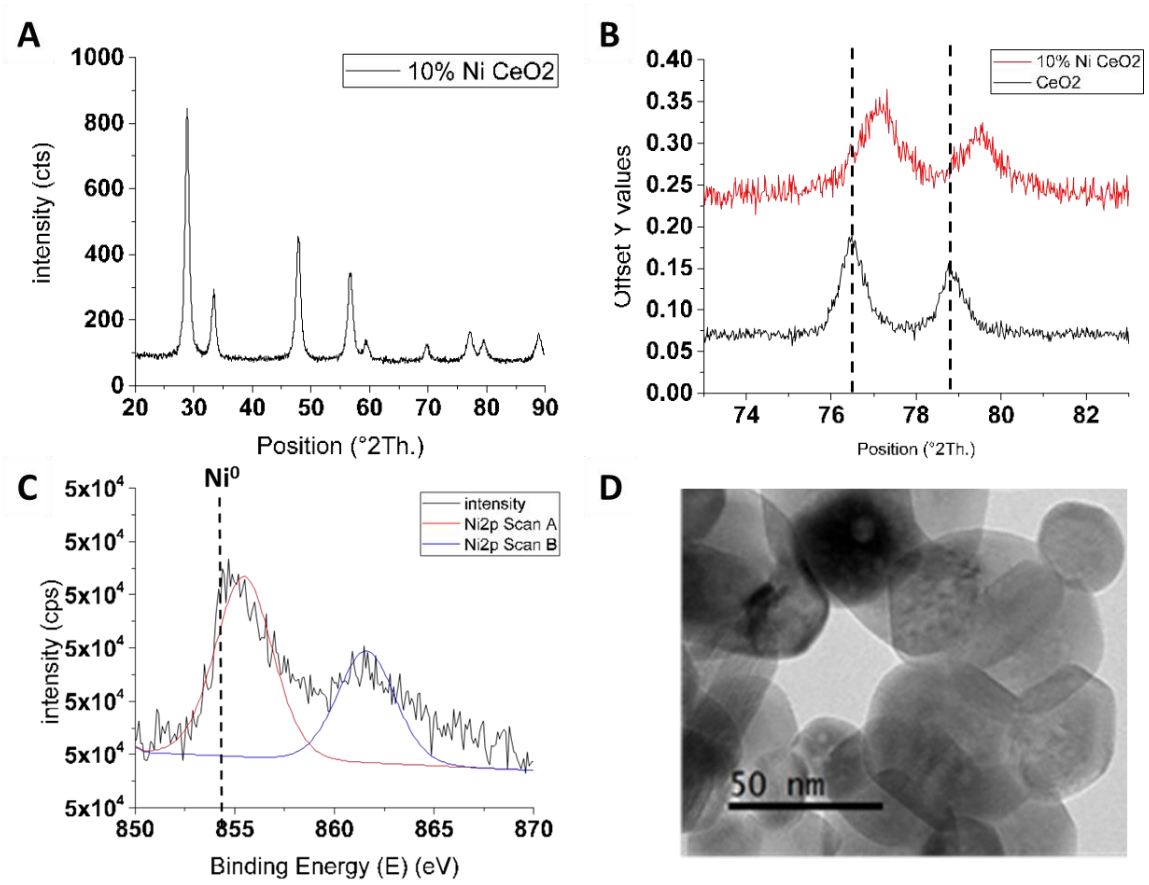

Figure 42 – (a) XRD pattern collected for 10% Ni doped CeO_2. (b) high resolution scan of high angle peaks highlighting the contraction of the CeO_2 lattice due to the substitutional doping of the Ni cations. (c) High resolution XPS spectra of Ni 2p region showing the binding of the 10% Ni doped sample, the location of metallic Ni is shown to highlight the fact that the Ni in the sample exhibits a higher BE and therefore is in a non-metallic state. (D) TEM image of Ni-doped CeO_2 particles

The cationic state of the Nickel dopant remained stable under operating conditions. In situ XANES and XPS spectra of the Nickel, collected under steam reforming atmospheres (97% CH_4 3%H_2O) are shown in Figure 43. Clearly, the local bonding of the Ruthenium is dissimilar to that of the metallic reference, and the binding energy is significantly higher than that reported for the metallic state.

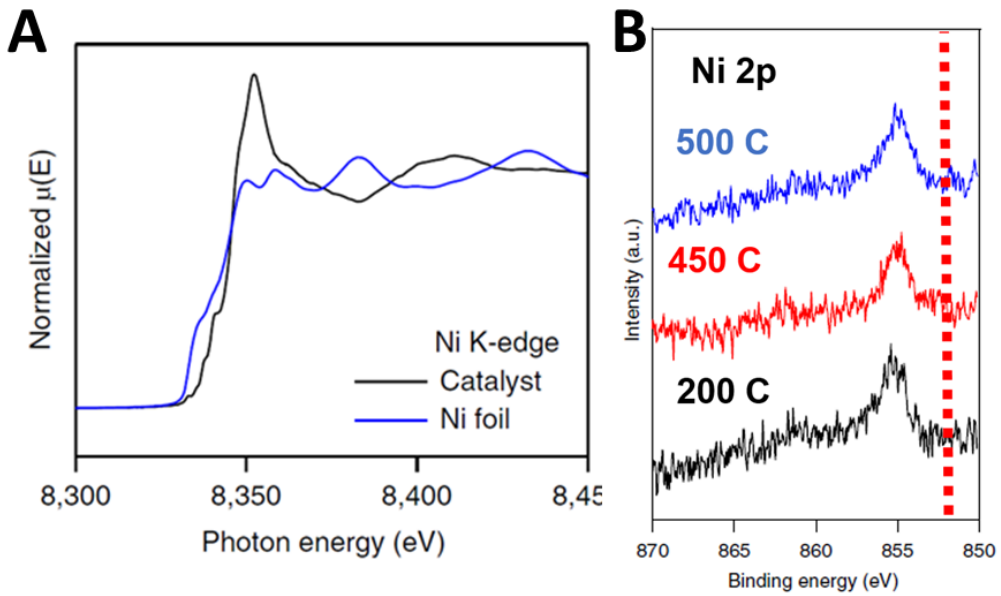

Figure 43 – (A) XANES spectra of Ni doped CeO_2 and reference Ni metal foil collected 200 °C under 97% CH_4 3%H_2O directly after testing at 500 °C. (B) Ambient Pressure XPS spectra of Ni 2p collected at various temperatures under 97% CH_4 3%H_2O, with the B.E. of Ni metal indicated by the dotted red line. Data collected by Yu Tang at University of Kansas, figure adapted from publication.[66]

Raman analysis was used to determine the effect of the Ni-dopant on the CeO_2 defect structure (Figure 44). In contrast to the Ruthenium dopant, the affect was subtler for the Ni addition, as Ni content increased there was only a slight increase in the D band, representative of oxygen vacancies (α peak), and with lower valence dopants (β peak). The presence of both α and β peaks confirms that these peaks are indicative of Ni cations doped into the structure, and the formation of oxygen vacancies to accommodate the (II) valence of the Ni cations, although the magnitude of the effect was less than that observed for Ru. The β peak could also be explained by the presence of Ce^{3+} cations, but this is not likely since the XPS analysis of these samples showed Ce primarily in the (IV) oxidation state. This observation is in agreement with a number of DFT works of ionic Ni in CeO_2, which

concluded that the incorporation of Ni^{2+} into the CeO_2 lattice resulted in the creation of oxygen vacancies without requiring the reduction of Ce^{4+} to Ce^{3+}.[76] [76,77].

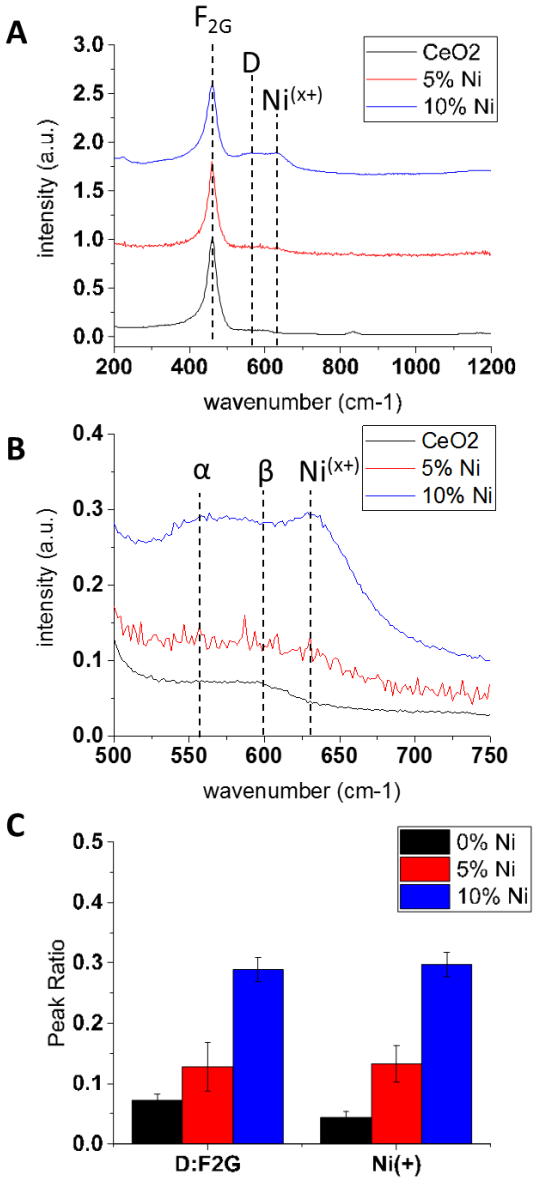

Figure 44 – (a) Raman spectra of CeO_2 with varying Ni dopant content, (b) chart of D:F_{2G} intensity ratio as a function of Ni dopant concentration. Error bars represent one standard deviation of the data collected from four locations on the sample.

It was also observed that the characteristic D band (made up of α and β peaks) included a distinct shoulder or peak between 610 cm^{-1} and 640 cm^{-1}, which was directly correlated with the presence of ionic Ni dopant. This observation has not been discussed specifically in the literature, although similar widening of the D peak with Ni doping can be seen in the spectra of other works.[78,79]. Andriopoulou et al, through a rigorous in situ Raman analysis of various rare earth dopants in CeO_2, observed a similar peak near 650 cm^{-1} which they attributed to highly detachable oxygen species located at interstitial sites, accessible due to structural distortions caused by the inclusion of the various rare earth dopants.[80] The presence of these Frenkel defects in CeO_2 has also been proposed by Mamontov et al, who correlated the presence of these oxygen interstitials to the activity and oxygen storage capacity of doped CeO_2.[81]

Here, this additional shoulder will be labelled as the "Ni(+)" peak, and tentatively assigned to Ni-O-Ce bonding, analogous to the Ru-O-Ce case discussed earlier, although the presence of the Frenkel defect remains a possible assignment. It is clear that this peak is directly related to the amount of ionic Ni doped into the structure, as well as with extrinsic oxygen vacancies in the CeO_2 lattice, although a specific vibration assignment is not detailed in this work. Further discussion on the assignment of this peak will be included in the conclusion of this chapter, in light of the new information gained through the included experiments.

4.7.3 In situ Raman analysis of Ni doped CeO_2

Under in situ conditions (500 C, H_2), the Ni dopant showed a subtler effect on the Raman spectra, relative to that of the Ruthenium dopant (Figure 45). The D:F_{2G} peak ratio of Ni-

doped CeO_2 was similar to the undoped case, although though the band associated with ionic Ni-O-Ce was largely removed. In contrast to the behaviour of the Ruthenium doped samples, the presence of ionic Ni in the CeO_2 did not seem to significantly enhance the reducibility of the catalyst under in situ conditions.

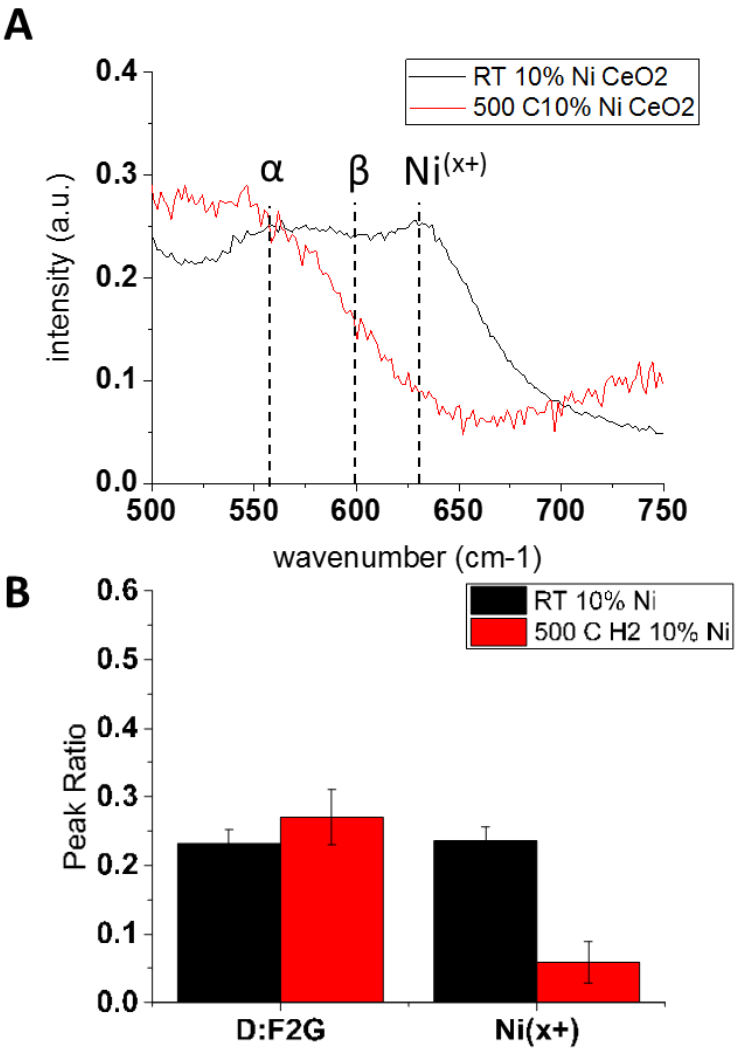

Figure 45 – (a) Raman spectra collected from 10% Ni doped CeO_2 at Room temperature and at 500 °C in H_2. (b) Chart of values comparing D and $Ni^{(x+)}$ peak intensity values at room temperature and at 500 °C in H_2. Error bars represent one standard deviation of data collected from four locations on the sample.

The degree of reduction was also not dependent on the concentration of Ni dopant. Figure 46 shows that the in situ D:F_{2G} ratio is similar for 0%, 5% and 10% Ni dopant. Although the presence of ionic Nickel increases the extrinsic oxygen vacancies measured at room temperature, the amount of vacancies formed under reducing conditions was similar to that of undoped CeO_2.

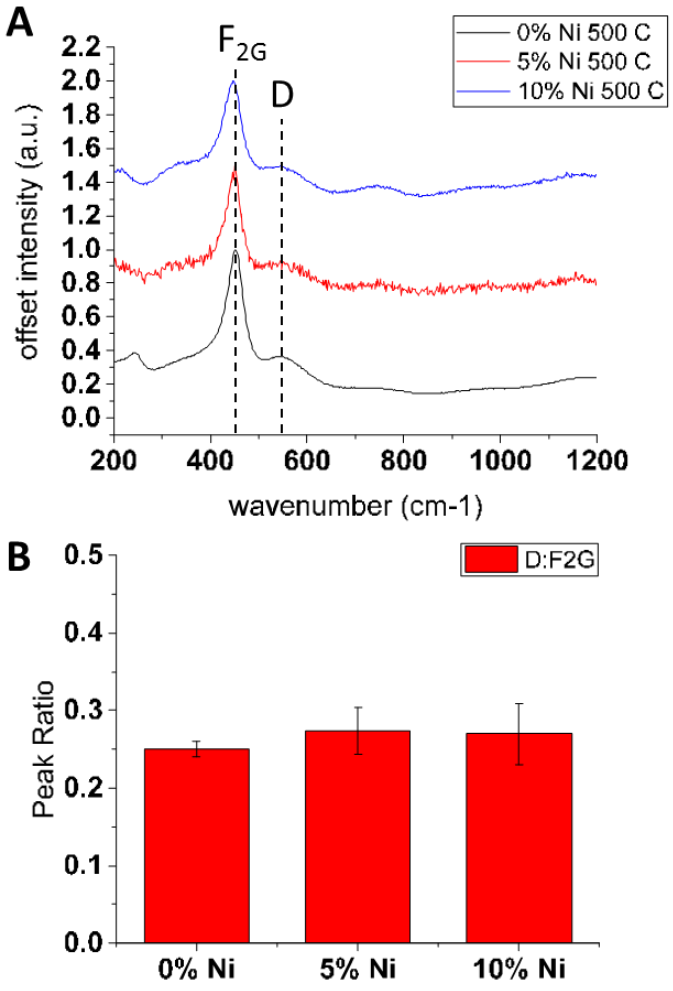

Figure 46 – (A) Raman spectra collected at 500 C in H_2 for varying concentrations of Ni doped in CeO_2 (B) Chart of D:F_{2G} ratios measured from the spectra shown in (A), error bars represent one standard deviation of data collected from four locations on the sample.

4.7.4 In situ Raman comparison of Ru, Ni, and co-doped CeO_2

Now that the in situ Raman behaviour of Ni and Ruthenium doped cases has been described, these observations will be used to better understand the behaviour of the co-doped case. Although H_2 testing revealed several dynamic structural changes, the true operating conditions of the catalyst is under methane fuel, therefore in situ Raman experiments were continued under this condition and compared to the information gained in previous sections.

The Raman spectra of undoped CeO_2 and samples with direct equivalent total dopant concentration level (10% Ni, 10% Ru, 5%Ru+5%Ni) under ambient, 500 C H_2, and 500 C CH_4 (3% H_2O) are shown in Figure 47. The co-doped sample shows similar peaks as those observed in both the singly doped cases, including a relatively high extrinsic oxygen vacancy peak as well as the bands associated with Ni and Ru ionic bonding, as described in earlier sections. As before, after the co-doped sample is heated to 500 C in reducing H_2 condition, the bands associated with the ionic dopant are largely removed, and the D band is increased.

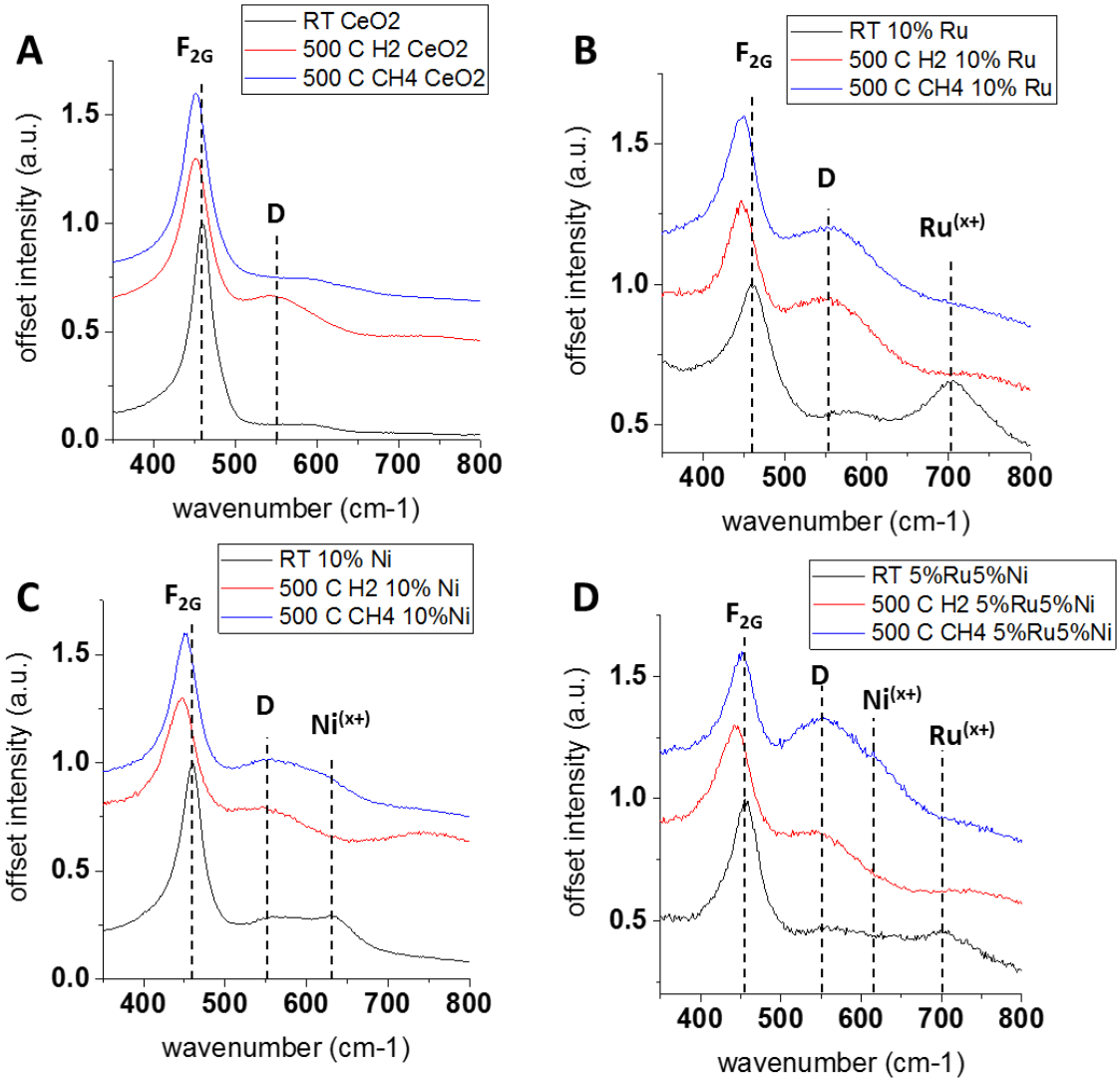

Figure 47 – Raman spectra collected at room temperature, 500 °C in H_2, and 500 °C in CH_4, for (A) undoped CeO_2, (B) 10% Ru doped CeO_2, (C) 10% Ni doped CeO_2, and (D) 5%Ru 5%Ni co-doped CeO_2

When the atmosphere is switched from H_2 to humidified methane, several interesting comparisons can be made. First, the D:F_{2G} ratio of the undoped CeO_2 sample is dramatically reduced when after switching from H_2 to humidified CH_4. It's likely that the decrease in intrinsic defect concentration is due to the relative inertness of methane at these temperatures compared to H_2 and resulting in a less reducing atmosphere. The Ruthenium

doped samples showed similar behavior as the undoped samples when switched from H_2 to CH_4, in that the D:F_{2G} peak was reduced, although to a much lesser degree. In contrast, the Ni doped samples showed a slight increase in defect density during the switch to CH_4. In addition, the intensity of the ionic Ni band increased in methane relative to H_2, whereas the intensity of the ionic Ruthenium band was stagnant. The co-doped sample shows the largest change between H_2 and CH_4, with a dramatic increase in D:F_{2G} ratio as well as an increase in the ionic Ni band intensity. These results are quantified in Figure 48, and an alternative presentation of Figure 47 is given in Figure 49, plotting each composition together under the three different conditions (Room Temp, 500 °C H_2, and 500 °C CH_4).

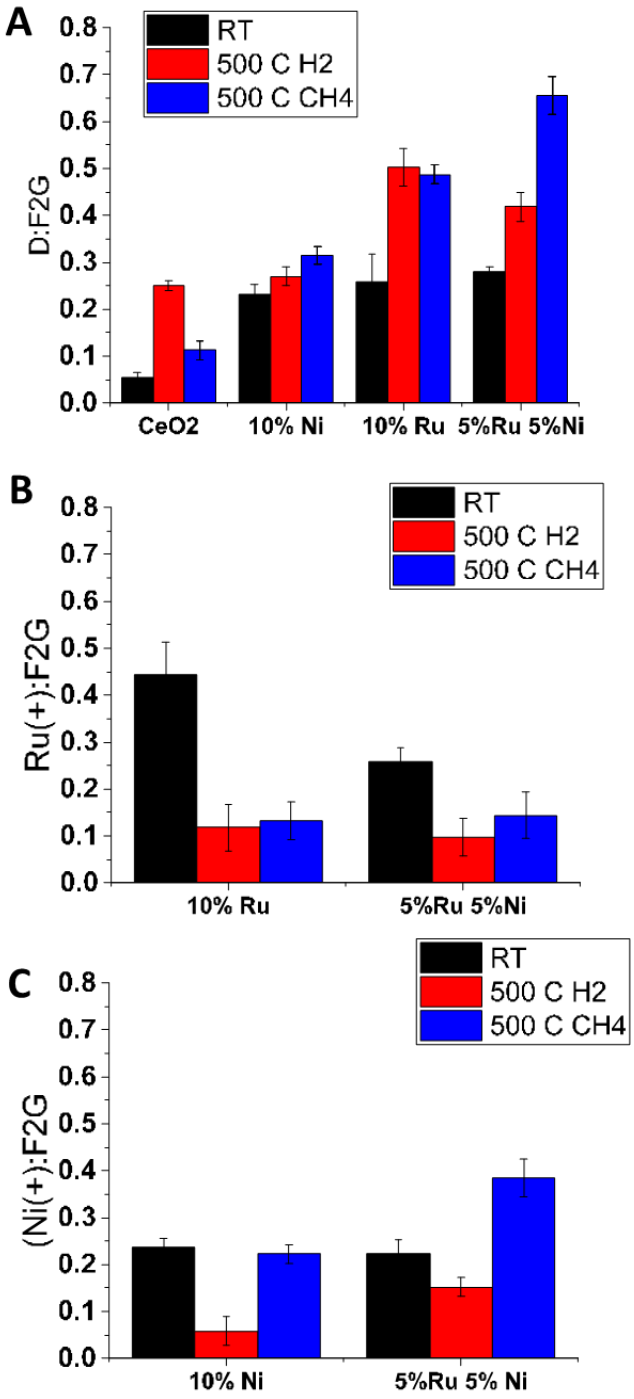

Figure 48 – Ratios of (A) Defect to F_{2G}, (B) Ru(+) to F_{2G}, and (C) Ni(+) to F_{2G} peaks observed for CeO_2, 10% Ni doped CeO_2, 10% Ru doped CeO_2, and 5%Ru 5% Ni co-doped CeO_2, as sample was heated from room temperature to 500 °C in H_2, and after switching to CH_4 at 500 °C. Error bars represent one standard deviation of the data.

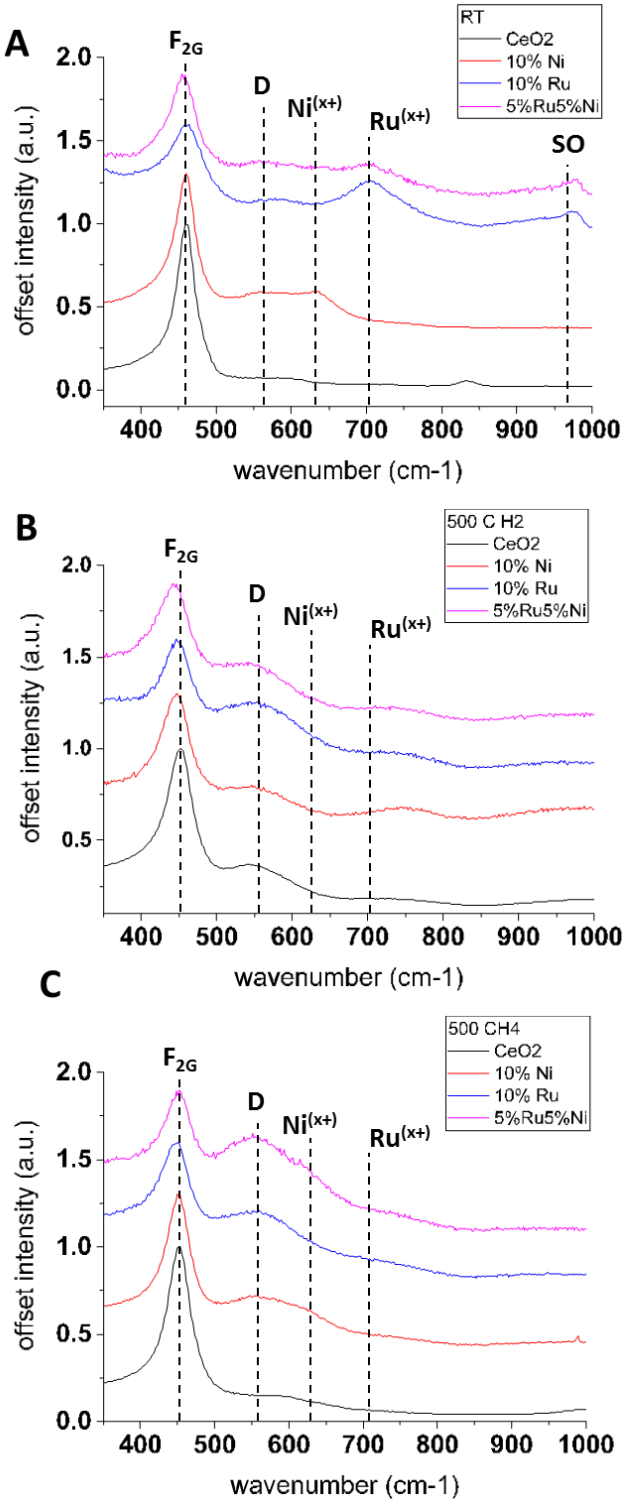

Figure 49 – Alternative presentation of Figure 47 in which each doping variation is compared under the same temperature and atmosphere, rather than following each doping variation individually through each atmosphere and temperature conditions.

Although the 10% Ruthenium sample showed the highest in situ oxygen vacancy concentration ($D:F_{2G}$) in H_2, the concentration of the co-doped sample was highest in CH_4. This could be explained by a possible higher activity of the Ni site for the activation of methane. Under the current testing condition, the steam:carbon ratio was very low (3:97), to simulate the most aggressive conditions that would be encountered in an operating SOFC. Under these conditions, the ability of the ionic Ni site to crack the C-H bond would correlate with increased reducing power of the atmosphere; i.e. a more active catalyst is more likely to be reduced through the oxidation of methane.

The in-situ Raman analysis shows that the presence of a Ruthenium cationic dopant dramatically enhances the reducibility of the CeO_2 lattice, whereas the Ni-dopant provides enhanced activity for the C-H bond in methane. This possibility will be discussed further in the next section, with the help of DFT computational analysis of the system.

4.8 DFT Analysis of Ru and Ni doped CeO_2

To better understand the possible reaction mechanisms at play in the co-doped catalyst, and how these mechanisms relate to the materials defect structure, DFT was used to simulate the surface of Ru and Ni doped CeO_2 under steam reforming conditions. A periodic slab model (periodic six-layer model with three inner layers fixed and three surface layers relaxed) of the (100) CeO_2 surface of CeO_2 was used through the Vienna ab initio simulation program (VASP) with a generalized gradient approximation (GGA). There are strong correlation effects for the partially filled 4f orbitals in CeO_2, therefore a Hubbard parameter was used to estimate the coulombic interaction (DFT+U). The

adsorption geometry of reactive molecules was optimized used using a force-based conjugate gradient algorithm, and their transition states by a constrained minimization technique. These calculations were carried out with the help of Dr. Ziyun Wang and Dr P. Hu at Queen's University Belfast, whose experience was invaluable in collecting and analyzing these results.

The Ru-O-Ce and Ni-O-Ce surface site geometry was first determined by a free energy minimization of each surface. The resulting, most stable, site is shown in Figure 50, with a Coordination number of three for Nickel and four for Ruthenium. The calculated bond lengths were shorter for Ni-O than Ru-O, at 1.89 A and 2.15 A, respectively. Next, the energy barrier for the initial CH_4 disassociation step was calculated for the ionic Ru and Ni sites, 2.01 eV and 1.88 eV, respectively. This suggests that the ionic Ni is the primary active site on the co-doped catalyst, since the initial dissociation of CH_4 is often the rate-limiting step for steam reforming reactions.

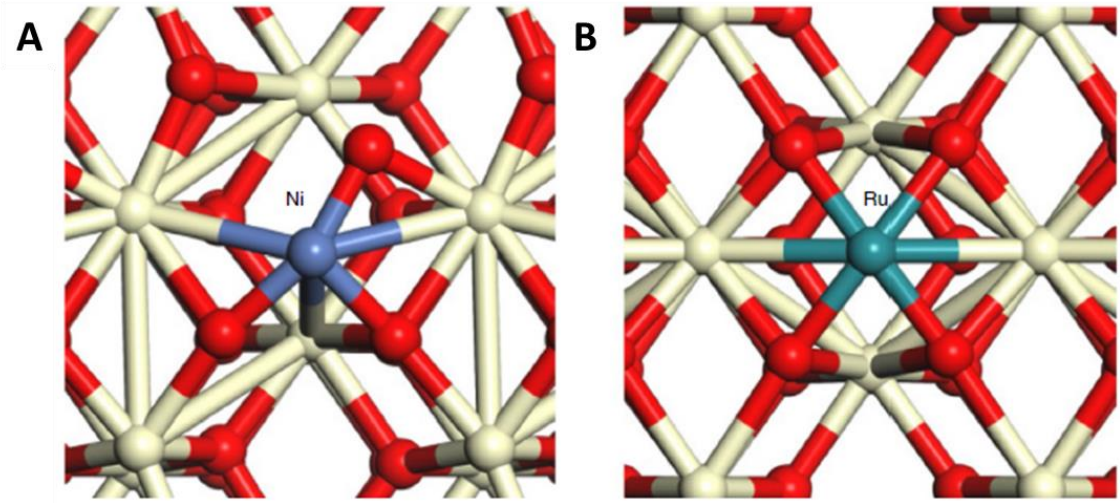

Figure 50 – Thermodynamically favored sites for (a) Ni and (b) Ru cations substitutionally doped into the surface layer of CeO_2. DFT calculations provided by Dr. Ziyun Wang at Queen's University of Belfast, figure adapted from publication.[53]

Fundamentally, steam reforming of methane requires four dehydrogenation steps and a carbon oxidation to fully activate the methane reactant. Two possible reaction paths were considered after the initial dissociation step, dehydrogenation of CH_3 to CH_2 + H and oxidation of CH_3 to CH_3O. In the Nickel doped case the activation energy for dehydrogenation and oxidation were 1.39 and 1.33 eV, respectively. In addition, the calculated enthalpy change for the dehydrogenation and oxidation were 0.5 eV and -0.03 eV, respectively. Therefore, it is highly likely that over the ionic Ni site, the oxidation of CH_3 to CH_3O occurs after the initial CH_4 activation. In contrast, the dehydrogenation step is more favored over the ionic Ruthenium site, with activation energies of 1.73 eV and 0.6 eV for dehydrogenation and oxidation, respectively, with enthalpy changes of 2.22 eV and 0.58 eV. Therefore, the two sites have distinctly different reaction pathways, with oxidation occurring immediately after the initial activation for the ionic Ru site, and dehydrogenation for the Ni site. The following reaction steps between $CH_4 \rightarrow CO$ were similarly calculated and are listed in Table 4.

Table 4 – Activation energy and Free energy changes associated with CH_4 oxidation over ionic Ru and Ni sites (calculations provided by Dr. Ziyun Wang at Queen's University of Belfast)

Ni-doped CeO_2			Ru-doped CeO_2		
Reaction Step	**E_a (eV)**	**ΔG (eV)**	**Reaction Step**	**E_a (eV)**	**ΔG (eV)**
$CH_{4(g)} + 2* \leftrightarrow CH_3* + H*$	1.88	0.94	$CH_{4(g)} + 2* \leftrightarrow CH_3* + H*$	2.01	1.86
$CH_3*+O* \leftrightarrow CH_3O* + *$ ($CH_3*+* \leftrightarrow CH_2* +H*$)	1.33 (1.39)	-0.03 (0.50)	$CH_3*+* \leftrightarrow CH_2* +H*$ ($CH_3*+O* \leftrightarrow CH_3O* + *$)	1.73 (2.22)	0.06
$CH_3O*+* \leftrightarrow CH_2O*+H*$	1.52	1.04	$CH_2*+O* \leftrightarrow CH_2O*+*$	1.30	-0.33
$CH_2O*+* \leftrightarrow CHO*+H*$	0.01	-0.03	$CH_2O*+* \leftrightarrow CHO*+H*$	0.48	0.44
$CHO*+* \leftrightarrow CO*+H*$	0.17	-0.20	$CHO*+* \leftrightarrow CO*+H*$	0.00	-1.29
$CO* \leftrightarrow CO_{(g)}+*$	0.07	0.64	$CO* \leftrightarrow CO_{(g)}+*$	0.12	-0.13

From this analysis it's clear that the ionic Ni site provides a lower activation energy for the initial methane dissociation step, and generally shows lower E_a values for the remaining steps relative to the Ruthenium doped case. Therefore, the ionic Ni site seems to be more active towards the conversion of CH_4 to CO, but recall that steam reforming requires the presence of steam to provide the lattice oxygen used in these reactions so a similar simulation was conducted investigating the activation of water over each site.

When the CO* is removed as $CO_{(g)}$, there must be an oxygen vacancy left in the lattice. For the reaction to repeat itself, this vacancy must be filled through the dissociation of an H_2O molecule (the oxidizing reactant in steam reforming). After H_2O adsorbs onto the oxygen vacancy site, two hydroxyl species are formed on the surface. The dissociation of a water molecule onto an oxygen vacancy had no energy barrier for either the Ni or Ru doped cases, although a significant difference in free energy change was calculated, 0.11 eV and -1.00 eV for Ni and Ru sites, respectively. After the vacancy has been filled by the dissociation of H_2O, the lattice oxygen has been replenished, but the hydrogen must be coupled and desorbed before the oxidation step of the CH_4 intermediate (CH_3*+O*↔CH_3O* + * for the ionic Ni and CH_2*+O*↔CH_2O*+* for ionic Ru) can occur. The energy associated with this step was then calculated for each site, with activation barriers of 1.96 eV and 0.65 eV, and free energy changes of 0.63 eV and 0.26 eV, for ionic Ni and Ru, respectively. The thermodynamic values are summarized in Table 5.

Table 5 – Activation energy and Free energy changes associated with H_2O dissociation at ionic Ru and Ni sites, calculations provided by Dr. Ziyun Wang at Queen's University of Belfast.

Ni-doped CeO_2			Ru-doped CeO_2		
Reaction Step	**E_a (eV)**	**ΔG (eV)**	**Reaction Step**	**E_a (eV)**	**ΔG (eV)**
$H_2O_{(g)} + V_O^* \leftrightarrow O^* + 2H^*$	0	0.11	$H_2O_{(g)} + V_O^* \leftrightarrow O^* + 2H^*$	0	-1.00
$2H_2^* \leftrightarrow H_{2(g)}$	1.96	0.63	$2H_2^* \leftrightarrow H_{2(g)}$	0.65	0.26

The basic conclusions from this DFT analysis is illustrated schematically in Figure 51. The results support the following basic conclusions: First, the ionic Ni site shows the higher activity toward methane activation than ionic Ru; second, the ionic Ni and Ru sites likely have two different reaction pathways; third, the ionic Ru site is much more active for the dissociation of H_2O and coupling of H_2; and fourth, the presence of ionic Ruthenium significantly lowers the E_a for oxygen vacancy formation. It is proposed that the synergistic effect of the co-doped catalyst is due to the combination of a strong CH_4 activating site and a strong water activating site (the oxygen vacancy). As CH_4 is chemisorbed to the ionic Ni site it is oxidized by lattice oxygen to the CH_3O^* intermediate and eventually the oxygen is desorbed as $CO_{(g)}$. The role of the Ruthenium site is to ensure the efficient creation and refilling of the oxygen vacancies which result from the oxidation of CH_4, through its higher activity toward H_2O dissociation and H_2 coupling, relative to the ionic Ni site.

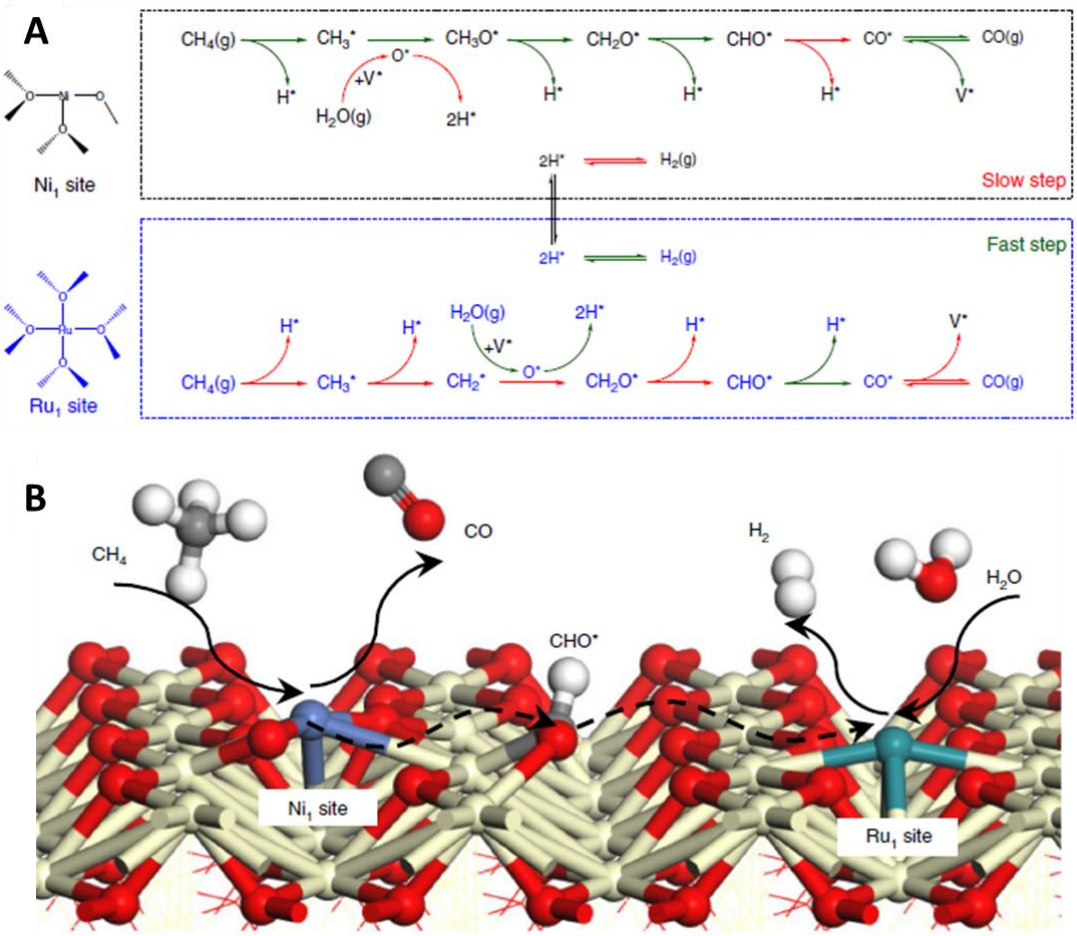

Figure 51 –(a) Proposed reaction mechanism sequence over ionic Ru and Ni sites. Slow steps (as predicted by DFT simulation) are shown in red, whereas fast steps are shown in green. (b) Schematic of synergy occurring when Ru and Ni sites occur nearby on the doped CeO_2 surface. calculations provided by Dr. Ziyun Wang at Queen's University of Belfast, figure adapted from publication.[53]

This DFT analysis provides a mechanistic explanation for the observed synergy in the co-doped Ru-Ni-CeO_2 catalyst. Considering the results of the in situ Raman analysis, it is proposed that the Ruthenium is enhancing the catalysis through multiple phenomena, first by enhancing the reducibility of the CeO_2 lattice, and second by providing efficient dissociation of H_2O and coupling of H_2. Since the Raman analysis did not show that the presence of ionic Ni increased the number of oxygen vacancies formed under operating

conditions, it is proposed that the primary role of the Ni dopant in the catalysis is to provide a highly active site for CH_4 oxidation.

4.9 Conclusions

Through the combination of experimental evidence presented in this chapter, several claims can now be made and supported.

First, it's been demonstrated that Raman spectroscopy is a powerful tool in the identification and characterization of Ru and Ni-doped CeO_2. Evidence of α and β peaks with increasing dopant level, confirm that the substitution of these cations into CeO_2 results in the formation of oxygen vacancies and other structural defects. Unique Raman bands were also observed, attributed to ionic Ru and Ni bonding. These modes were dependent both on testing conditions and pre-processing. Under reducing conditions, these Ru-O-Ce bonds are reduced to Ru-V_O**-Ce bonds, and this band is removed as the Defect band is increased. Upon re-oxidation, the vacancies are filled and the Ru-O-Ce signal returns. The relative concentration of oxygen vacancies (as determined by the relative ratio of the D band) is dramatically enhanced by the presence of ionic Ruthenium, showing that the oxygen storage capacity and overall reducibility of CeO_2 is enhanced by the presence of ionic Ruthenium, whereas this enhancement is not observed in Ni-doped CeO_2.

The dramatic enhancement in reducibility is unique to the case of ionic Ruthenium doped into the CeO_2; a sample which had been pre-annealed at high temperature (900 C 4% H_2, 2h) and had precipitated its Ruthenium content as metallic nanoparticles on the surface did not show the characteristic Ru-O-Ce Raman peaks and did not show as high of concentration of oxygen vacancy defects during in situ measurements. In addition, by

comparing the steam reforming performance of the as-doped samples to precipitated samples (with identical Ruthenium loading), a clear connection was made between the Ru-O-Ce bonding observed by Raman and the improved final catalyst performance.

Raman is a relatively simple technique, which doesn't require complex sample preparation, high vacuum, or beam-line access, therefore this study provides a more accessible strategy to other groups seeking to study ionic noble metal doped CeO_2. This work has confirmed that Raman spectroscopy is able to predict whether these precious metals are successfully doped into the lattice or simply supported as metallic nanoparticles on the CeO_2 particles and has revealed unique Raman bands resulting from the presence of noble metals stabilized in a cationic state in the CeO_2 lattice. These bands remain poorly defined, and the results of this work warrant further analysis and more accurate assignments of Raman bands present in these materials.

Second, a synergy was observed between ionic Ruthenium and Nickel dopants in CeO_2 for intermediate temperature steam reforming. By combining information gained from in situ Raman spectroscopy and DFT simulations, a mechanism for the synergy was proposed: ionic Ni was found to be highly active for the activation and oxidation of CH_4 to CO, whereas ionic Ru provided enhanced ability to dissociate H_2O and couple H_2. Both sites required the presence of mobile lattice oxygen and oxygen vacancies for the reactions to proceed, and the ionic Ruthenium was found to increase the number of these oxygen vacancies present under operating conditions relative to Ni doped or undoped CeO_2. This mechanism of synergy suggests that a similar strategy may be used for the future rational design of other anode reforming layer materials, adding multiple dopants which each have a specific role in the reaction, such as increasing oxygen storage capacity, defect

concentration, and activity for different reactants. Ionic Ruthenium doped into CeO_2 is a relatively under-studied catalyst, and further application of this material for intermediate temperature and low temperature reactions is suggested, especially in combination with highly active surface sites, due to its ability to simultaneously increase in situ vacancy concentration and surface activity. Although Ruthenium is a relatively expensive metal, the loading amounts used in the SOFC are small (0.005 mg/cm^2, Ru), and the material cost of the Ruthenium is expected to be negligible relative to the bulk materials used in the SOFC and the various components required for balance of plant. Still, since a likely mechanism has been constructed for Ruthenium's ability to promote the Ni-site, it is possible another, less expensive, dopant could be identified which also increases the formation of CeO_2 defects and water activation with similar efficiency as the ionic Ru dopant.

Finally, this work has directly contributed to the advancement of current SOFC technology, demonstrating that through the development of highly active materials direct methane operation is possible at low temperatures (500 °C). Through the advanced characterization of the critical Anode Reforming Layer (ARL) catalyst, a co-doped $Ru_xNi_yCe_{1-x-y}O_2$, new strategies have been proposed for enabling the efficient internal reforming of fuels at low temperatures. The knowledge gained through this work has the potential to improve not only SOFC technologies, but CeO_2 based catalysis for a number of possible processes, through the incorporation of ionic noble metal dopants and use of in situ Raman spectroscopy as a strategy to analyze and design these materials.

CHAPTER 5. FABRICATION AND VALIDATION OF NI-SDC MODEL SOFC ANODES

5.1 Summary of chapter

Due to the complicated processes required to fabricate small scale prototype SOFCs, and the large number of different factors that influence cell performance, it is difficult to rigorously compare the performance of different anode materials. A model cell was developed which limits the cell performance to the anodic processes, while providing an open architecture for simplified characterization of the electroactive anode surface. Through Electrochemical Impedance Spectroscopy (EIS), the activity of the anode can be quantified and normalized to the active triple phase boundary of a Ni-SDC anode. These cells were used to make basic comparisons between Ni-YSZ and Ni-SDC systems, and to evaluate the basic anodic behavior of the Ni-SDC anode system. The effect of several functional coatings on cell activity was evaluated, demonstrating the use of this platform for the quantitative screening of candidate materials for high performing SOFC anode coating materials. In addition, an operando Raman spectroscopy chamber was designed and fabricated, capable of button-cell testing and uniquely suited to further characterization of SOFC anode materials and model cells.

5.2 Patterned Model Electrodes

A solid oxide fuel cell is a complicated device, with several different materials and architectures working in unison to produce electricity. This implies that the relative

performance of a cell is dependent on several losses occurring throughout the cell, described by various overpotentials associated with phenomena such as ohmic resistance to ion or electron conduction, activation barriers for reactions at anode or cathode, and mass transport limitations. In addition, less obvious losses occur from the difficulties in assembling the cell, such as poor lead connections, current leakages, or inadequate sealing between the anode and cathode atmospheres. The objective of a model cell is to simplify the analysis of SOFC devices by focusing on just one of these losses. By limiting the number of active sites of the anode, relative to the cathode, the mass transport and activation losses occurring at the cathode can be disregarded when analyzing the cell performance. Similarly, by replacing the complicated porous anode with a two-dimensional interface, diffusion limitations at the anode are also negligible. This results in a cell's performance being controlled by only the ohmic resistance of the electrolyte, and the electrochemical reactions occurring on the anode.

Using Electrochemical Impedance Spectroscopy (EIS), the anodic polarization can be separated from the ohmic polarization by applying a simplified Randles cell circuit model. The ionic impedance of the electrolyte will have no capacitive response, and therefore can be determined by the x-axis intercept of the Nyquist plot. By subtracting this ohmic impedance from the x-axis, the spectra can finally be reduced to a single representation of the anodic impedance. This is the main objective of the pattern model anode, to reduce the impedance contributions from every phenomenon except for the anodic reactions. This enables impedance spectroscopy to compare and analyze the anodic behavior of an SOFC under different temperatures, fuel compositions, and voltages, independent of complicating factors occurring on other cell components.

The electrochemical reactions occurring at the anode require a combination of electrons, ionic species (O^{2-}) and gas species (H_2) and therefore the reaction can only occur where all of these species coexist. This is defined as the Triple Phase Boundary (TPB), where the electronically conductive phase (Nickel), ionically conductive phase (ceramic electrolyte) and fuel meet, as illustrated in Figure 52. The length of the TPB, or L_{TPB}, is the region of the anode that is electrochemically active, and therefore the performance of SOFC anodes scales with this length. This is one of the fundamental reasons why the SOFC architecture affects the performance, anodes with an optimized microstructure with greater TPB length will show higher performance independent of the inherent catalytic activity of the anode materials.

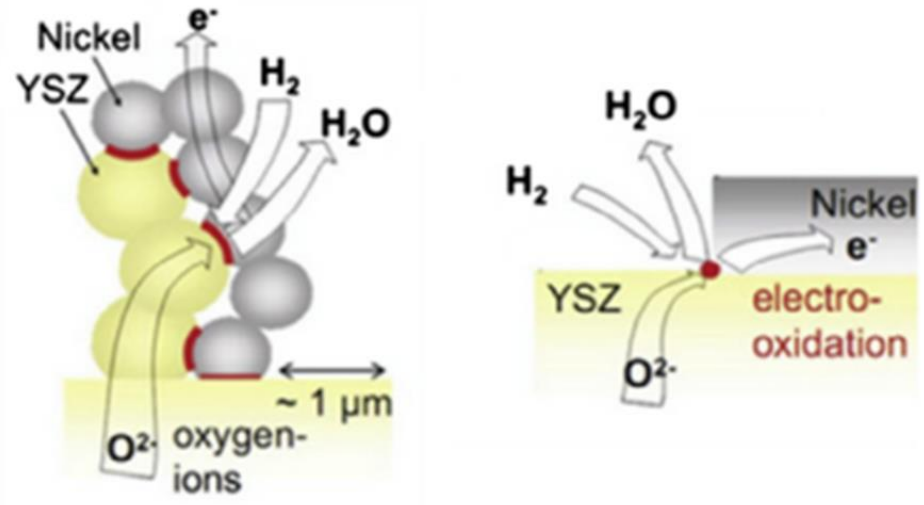

Figure 52 – Macro and micro-scale illustrations of the Triple Phase Boundary (TPB) active site for a Ni-YSZ SOFC. Figure adapted from Bessler et al[82]

In order to control for these microstructural effects, the L_{TPB} length in a model anode must be well-defined. By fabricating a controlled pattern of Ni onto an electrolyte, the L_{TPB} is limited and easily quantified. By pairing a well-controlled, two-dimensional anode with a standard high surface area cathode, the cell can be tested in a simple two-electrode set up, using the counter electrode as the reference, as illustrated in Figure 53. Since the density of active sites is much greater on the porous cathode, the cathodic contribution to the total cell impedance is negligible. This most resembles the operating condition of a true SOFC device and avoids the placement of reference electrodes on a solid electrolyte, which is highly sensitive to errors and a correct position of reference electrode remains a contentious topic.

Previous work with patterned model anodes has increased the fundamental understanding of the reactions and processes occurring over SOFC electrodes. Mizusaki et al was the first to use this technique, using photolithography to deposit a Ni pattern on a polished YSZ substrate.[83,84] They found that the impedance of the anodic reaction over Ni-YSZ produced one symmetric semicircle (on a Nyquist plot), and the activity of the cell was promoted by increased pH_2O in the fuel, independently of the pH_2. They confirmed that the activity of the cell was directly proportional to the triple phase boundary length (L_{TPB}) and proposed a reaction mechanism in which the rate limiting step was the dissociative adsorption of hydrogen occurring over the Ni component, with significant contributions from surface diffusion. Similar work has been done with pattern anodes to build on this work, most notably by Bieberle et al and Besseler et al, confirming the TPB dependence as well as proposing mechanisms for the observed activity improvement in the presence of increased pH_2O through hydrogen spillover from the Ni component to hydroxyl species on the YSZ

surface.[85,86]. Patterned model anodes have been largely been limited to the study of the Ni-YSZ system, although more recent work done by Chueh et al has included the study of Ni-SDC patterned anodes.[87,88] Due to the mixed ionic and electronic conduction of reduced CeO_2, the fundamental behavior of these anodes is different than that of Ni-YSZ, with evidence of rate-limiting reactions occurring on the ceramic phase several microns away from the TPB interface, as well as a lower dependence of the anodic activity on the L_{TPB}.

An attractive and relatively unexplored use for these patterned anodes is to study the effect of various surface modifications and coatings on the anode performance. Recently, Choi et al used solution based electrochemical deposition techniques to show that the addition of a porous, nanostructured SDC coating significantly improved the activity and stability of a patterned Ni-YSZ anodes.[89] Although, the ability of infiltrated catalyst coatings to dramatically improve performance and stability of SOFC anodes has been well demonstrated in full cells, there is a need for suitable testing platforms to quickly and quantitatively compare and study candidate coating materials for real-cell application, without the complications of a porous microstructure and poorly defined architectures inherent to prototype button cell SOFCs. Application of these modifications on patterned Ni anodes on SDC is limited, and further exploration of this system needed, as Ni-SDC anodes exhibit dramatically improved stability and performance compared to Ni-YSZ anodes for intermediate and low temperature SOFC applications.

5.3 Embedded Ni-mesh Model Cells

Deposition of Ni patterns by standard lithography techniques can provide very high levels of control, but cells fabricated in this manner require cleanroom processing and are plagued by a number of failure modes which can convolute the results.[90-92] Under moderate temperatures, the thin Ni films can coalesce into several large particles, creating voids and disconnections in the pattern during testing. Delamination of the film is also common, due to the combination of CTE mismatch and to Nickel's relatively weak ability to adhere to ceramic substrates. Grain coarsening is also a common artifact, as the temperatures increase the TPB length can increase as line-edge of the pattern is roughened by facet formation. Poor adhesion of the Ni to the electrolyte can lead to delamination and buckling. These challenges can be lessened by careful control of Ni film thickness, annealing above temperature of interest, and optimization of sputtering conditions. Other strategies have been proposed to avoid these issues, most commonly point electrodes. In this approach a single wire of Ni pressed against the electrolyte during testing, forming a single TPB site on the surface. This technique can yield important fundamental data but has its own drawbacks due to the low L_{TPB} and difficulty in accurately estimating the L_{TPB} resulting from the contact of the wire to the surface.

An alternative strategy is to embed a section of nickel mesh within a pressed pellet of the electrolyte powder, sintering until dense, then polishing to reveal the Nickel surface. Features between 20 and 100 μm, readily available mesh sizes, are able to provide suitable L_{TPB} for electrochemical measurements. The embedded mesh is mechanically supported within the electrolyte, and sintered to temperature well above operating, therefore the Ni pattern is very robust compared to those deposited by photolithographic techniques. In addition, these feature sizes are within the spatial resolution of standard optical

microscopes, and therefore are ideal for in situ and operando spectroscopy, as well as optical measurement of L_{TPB} and post mortem characterization of the electrochemically active region. This strategy has been used in several works for in situ spectroscopy studies of Ni-YSZ as well as in fundamental investigations of Pt-BZZYb reaction mechanisms.[93,94] Recently, Blinn et al used the embedded mesh cell to relate the electrochemical impedance spectra of these embedded mesh cells to observed in situ Raman spectra, demonstrating the ultimate potential of this platform for true operando spectroscopy of the electrochemically active sites in SOFC anodes.[95]

Therefore, the fabrication of embedded mesh Ni-SDC model cells was investigated in this work. This design, shown schematically in Figure 53, satisfies the major goals of this work, to find a suitable platform for investigating the inherent activity of Ni-SDC anodes, and to develop this platform for the screening and quantitative analysis of different functional coatings applied to Ni-SDC anodes. Through the development of this model cell, a novel tool for exploring active coatings can be achieved, providing a more rigorous testing bed for SOFC anode coating materials development than that provided through current button-cell methods.

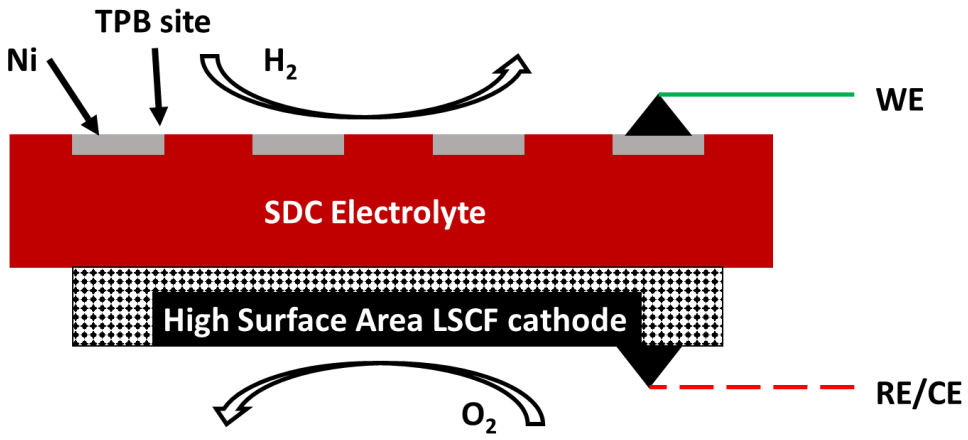

Figure 53 – Schematic of embedded Ni-mesh model cell, showing limited TPB sites on the polished planar anode and high surface area porous cathode.

5.3.1 Fabrication of Ni-SDC model cells

Circles of Ni-mesh were first punched out of a sheet of Ni (alfa aesar 40 mesh woven from 0.13mm dia wire). To flatten the mesh, each circle was placed in a 13 mm pellet die and pressed to 1 ton. This created a simple 2D pattern and avoided any curvature inherent to the Ni-sheet after punching. After preparing the Ni patterns, 0.3 g of SDC powder was added to a 13 mm pellet die, then pressed to 1 ton and held for 1 min. This flattened the powder so that the Ni-mesh would lie flat. A pre-pressed Ni pattern was then placed in the center of the powder at the bottom of the die and then pressed again to 1.5 ton and held for 1 min. This step embedded the SDC within the first half of the powder. The mesh pattern was then covered with another 0.3 g of SDC powder and then pressed to 5 ton and held for 2 min. After ejecting the pellet, it was placed in an alumina crucible with a clean SDC powder bed. The pellets were then fired to 1400 °C according to the following schedule (1 C/min to 400 C, 30 min soak, 1C/min to 800 C, 30 min soak, 3 C/min to 1400

C, 10 h soak, 1 C/min to 1000 C, 3 C/min to RT). A reducing 4% H_2 balance Argon gas was used to protect the Ni phase from NiO formation. Due to the reducing conditions, the pellets were calcined to 400 °C for 30 min in air after the sintering treatment, to remove the oxygen vacancies formed by the reducing atmosphere in the SDC electrolyte. The mesh was then revealed through systematic polishing. A 8 mm diameter LSCF cathode was applied to the opposite face through screen printing three layers of a commercially available ink (FuelCellMaterials ®) to reach ~ 50 um thickness after drying for 4 h in a 80 C oven. Electrical connections were made using Ag wire and Ag paste before sealing the cell to the end of a 0.5" diameter alumina tube using Ceramabond 552 (Aremco), as detailed in section 3.1.2. A basic summary of the fabrication process is shown in Figure 54, and the polishing protocol is detailed in Table 6.

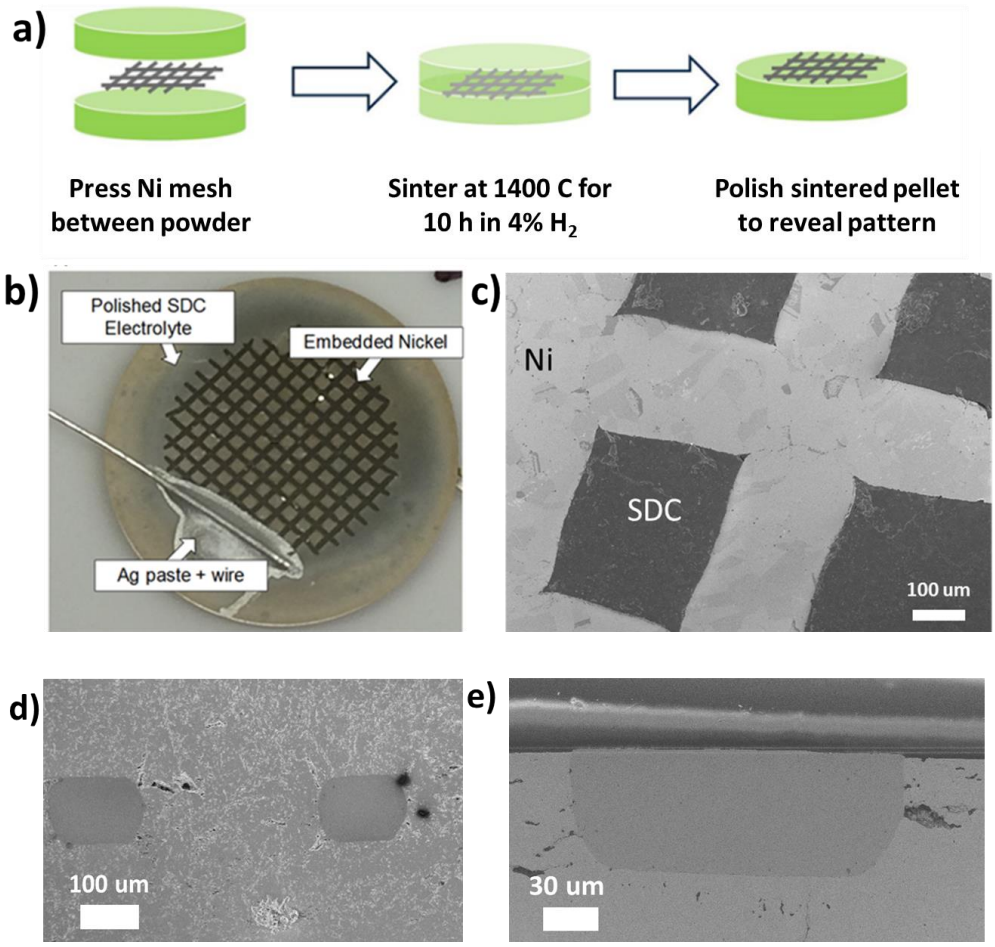

Figure 54 – (a) illustration of embedded Ni mesh fabrication process (b) optical image of cell after polishing and addition of Ag wire connection (c) top-down SEM of Ni-SDC interface. (d) Cross-section of embedded mesh after sintering at 1400 °C, before polishing to reveal mesh. (e) Cross-section of embedded mesh after polishing to reveal mesh. Schematic in (a) is modified from that presented in Blinn et al[95]

Table 6 – Polishing protocol used to reveal Ni-mesh embedded in sintered SDC pellets

Polishing compound	Force (N)	Cloth	Platen RPM	Sample RPM	Time (s)
Green Lube	9	15 um Diamond Grid	350	150	15
6 µm	9	Diamat	350	150	60
3 µm	4	Gold Label	350	150	240
1 µm	4	White Label	350	150	120
0.1 µm	4	Final A	350	150	120

The embedded mesh method provides relatively fast fabrication, good thermal stability of pattern during in situ analysis, and has been used successfully in previous in situ spectroscopy work (using YSZ electrolytes). Unfortunately, there is an inherent lack of control over pattern morphology in this approach since it depends directly on the mesh patterns available, the alignment of the Ni mesh within the pellet and the degree of polishing. In addition, the standard sintering temperature for SOFC electrolyte materials,

such as YSZ, are 1450 °C, very near the melting temperature of Ni, 1455 °C, and pellets can fracture during sintering, likely due to the voids around the Ni mesh and the large thermal expansion associated with heating and cooling Ni to such temperatures. Pattern morphology and choice of material is limited in this approach, but the trade-offs are in final thermal stability and more robust embedded planar interface.

The key assumptions of the model cell are that the polarization of the anode dominates the non-ohmic impedance of the cell (due to the asymmetry of surface area between cathode and anode) and that there are no mass transport limitation (due to the non-porous, planar architecture of the anode). These assumptions are tested in the following section.

5.4 Electrochemical behavior of model cells

The embedded mesh model cells were able to function as SOFCs, able to produce current and sustain a reasonable OCV under H_2 fuel. The representative baseline open circuit voltage, impedance and I-V-P curves are shown in Figure 55. The overall performance of the cells is relatively low, as expected for a planar anode with limited triple phase boundary active sites. The observed voltage was consistently lower than the theoretical Nernst potential, due to the electronic conductivity of partially reduced SDC electrolyte. This result is not surprising, and the degree of leakage current is reasonable for these conditions.

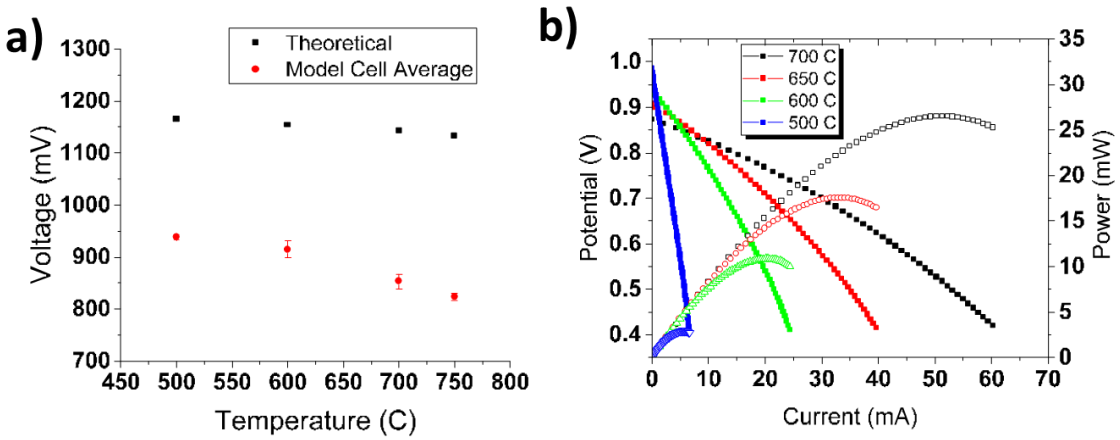

Figure 55 – (a) Average measured OCV values for Ni-SDC model cells compared to theoretical OCV for 97% H_2/3% H_2O anode with ambient air cathode. (b) I-V-P curves collected between 550 °C and 650 °C for Ni-SDC model cells

The most critical requirement for the application of the model cell is the relative impedance of the anode, which is assumed in this model to be much larger than that of the cathode or any mass transport limitations. Figure 56 shows the relative impedance of an analogous symmetric LSCF cell, overlaid with that of the representative Ni-SDC-LSCF model cell. The impedance contribution of the cathode is consistently less than 10% of the total impedance of the model cell, consisting of a single depressed arc, and therefore we can confidently disregard the contribution of the cathode in further analysis.

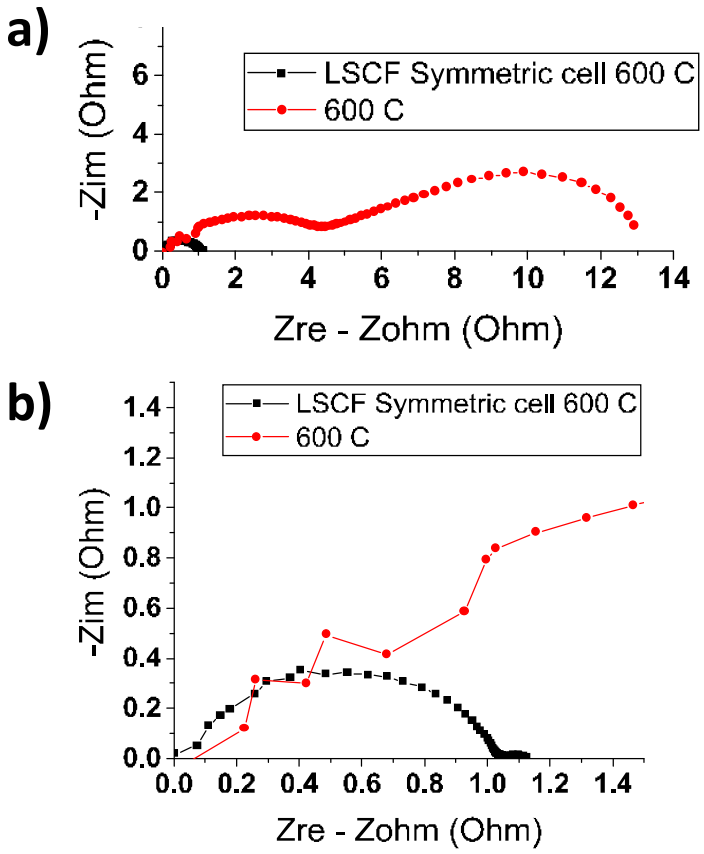

Figure 56 – (a) Representative impedance spectra of an embedded mesh Ni-SDC model cell and a symmetric LSCF/SDC/LSCF cell, measured at 600 C (b) Rescaling of the spectra in (a) highlighting the spectra from the symmetric cell.

Due to the low active site density of the embedded Ni-mesh, it is important to avoid any other sources of anodic reaction that may effectively short the anodic impedance. Ag paste was required to form electrical connections to the cell, and may have some inherent activity toward H_2 oxidation, obscuring the model cell measurement. To test this effect, cells were fabricated without a Ni-mesh component (only Ag paste on the SDC surface) and compared to two groups of embedded mesh cells, one with a bare Ag paste connection and another with the Ag paste covered by high temperature sealant used to affix the cells (Ceramabond 552®). The impedance of these cells is shown in Figure 57.

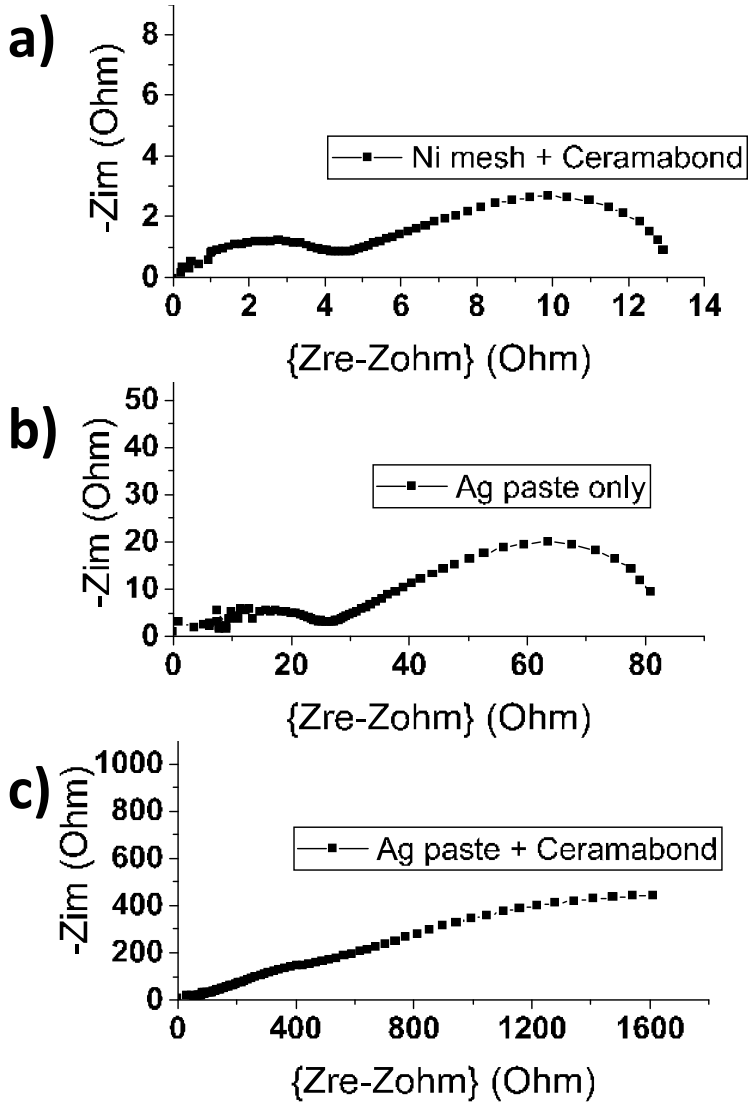

Figure 57 – Representative impedance spectra of (a) embedded mesh Ni-SDC model cell with Ag paste connection covered by Ceramabond sealent (b) Ni-free model cell with Ag paste on a polished SDC surface, and (c) Ni-free model cell with brush painted Ag paste on a polished SCD surface, covered with Ceramabond sealant. Measurements were collected at 700 C with 60 sccm H_2 flowing over anode and ambient air over cathode (screen-printed LSCF).

The impedance of the Ni-mesh cell is considerably lower than that of the Ag paste only cell, although the Ag-paste cell was able to provide a reasonable OCV. (~926 mV at 600 °C in H_2). The OCV of the Ag paste cell with the Ceramabond sealant was effectively zero (-1.22 mV), which confirmed that the addition of the Ceramabond sealant to the Ag paste connection effectively separated the connection from the experiment. Under this condition, we can confidently assume that the contribution of the Ag paste is negligible in this cell and can be disregarded in further analysis.

To make rigorous calculations of polarization between cells, it is critical that the cells are stable over the long periods of time and exposure to high temperatures required for these experiments. To demonstrate the stability of the embedded mesh architecture, cells were heated to 750 C under 60 sccm H_2 and held for three days. Impedance spectra were collected at 4 h, 28 h, and 72 h, as shown in Figure 58. There was a slight change in Rp after the first 4 h, but the cell quickly stabilized at the spectra remained unchanged after 72 h. This result demonstrates that there is no significant degradation of the cell during the relevant testing periods used in this work, and indeed no stability issues were observed during further testing of model cells in H_2.

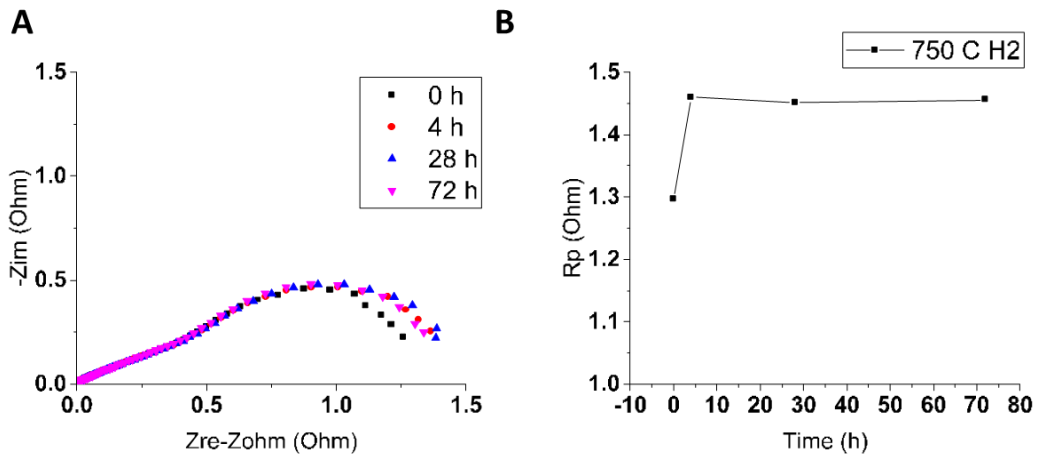

Figure 58 – (a) impedance spectra collected after heating the cell to 750 C under 60 sccm H_2 (3%H_2O) with ambient air over the cathode. (b) Rp values of the cell collected at various times during the three day test.

The contribution of any mass transport limitations was tested by varying the flow rate over a model cell from 15 to 120 sccm while collecting I-V-P curves and impedance spectra at operating potential (0.6 V). Current density and impedance at higher potentials were unchanged while decreasing flow rate from 120 sccm to 60 sccm, but there was some effect at lower flow rates. Similarly, the impedance spectra collected at 600 mV (-273 mV from OCV), was not strongly affected by flow rate until the flow was decreased below 15 sccm. Based on these results, flow rates above 60 sccm were used for all further testing to avoid any concentration polarization due to gas diffusion. .

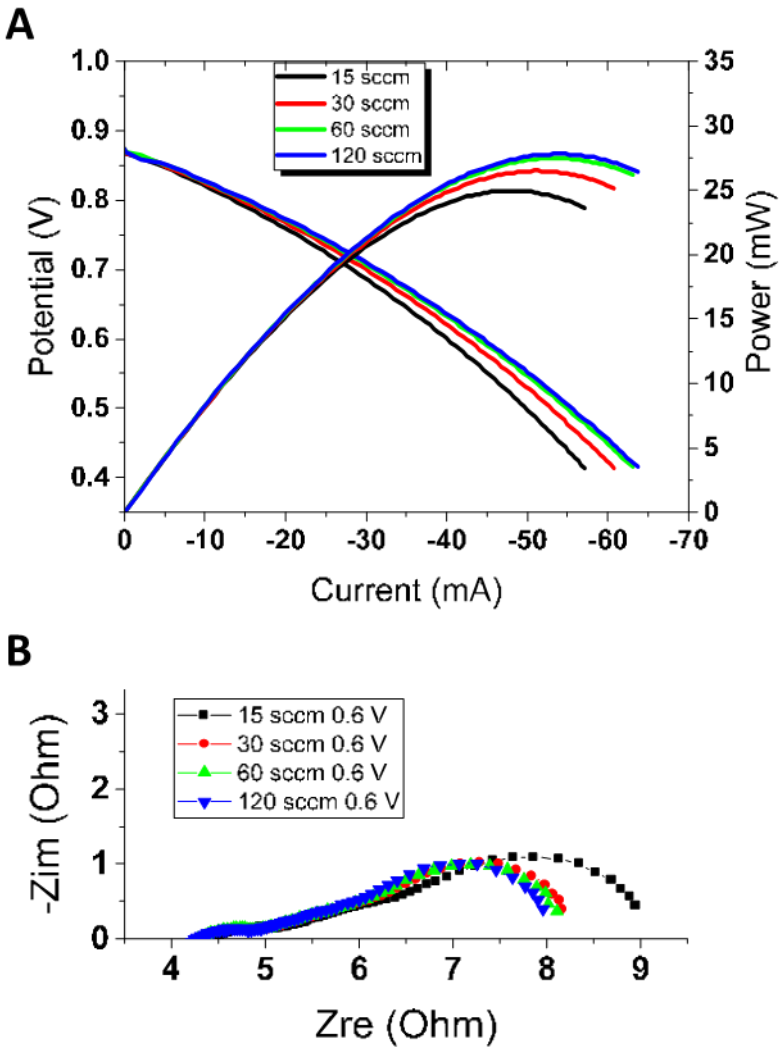

Figure 59 – (a) Representative I-V-P curves for Ni-SDC model cell collected at increasing flow rates (b) impedance spectra collected 0.6 V at each of the flow rates shown in (a). Data was collected at 700 C while flowing humidified H_2 (3% H_2O) over the anode and ambient air over the cathode.

Through these observations we can now make the following conclusions for the Ni-SDC model cell: Impedance contributions from cathodic processes are negligible, impedance contributions from mass transport limitations are negligible, and the presence of Ag-paste connections do not interfere or amplify the anodic processes over the Ni-SDC interface

With the assumptions of the cell validated, experiments were continued to analyze the baseline anode electrochemical behavior using the model cells.

5.4.1 Analysis of embedded mesh impedance spectra

Representative impedance spectra of Ni-SDC model cells are shown in Figure 60. Temperature has a clear effect on the shape of the impedance spectra, with a low frequency arc dominating at higher temperatures, and a high frequency arc contributing more to the spectra as the temperature is decreased.

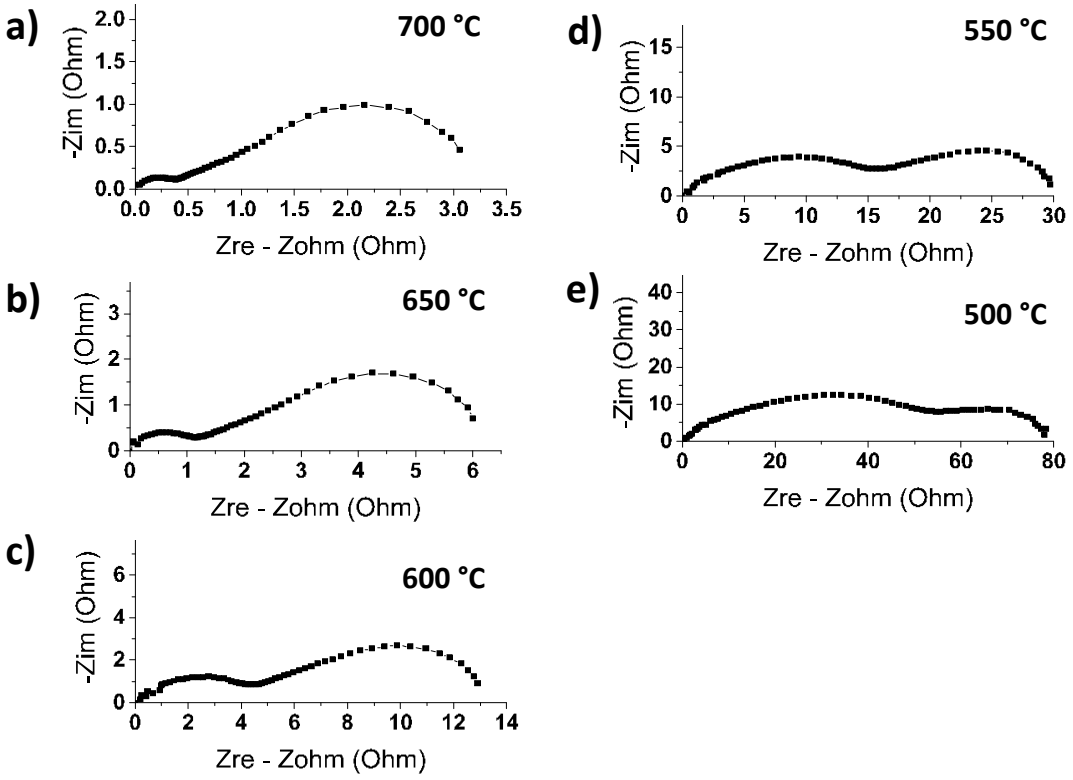

Figure 60 – Impedance spectra for Ni-SDC model cell collected between 500 °C and 700 °C (a-e). 60 sccm H_2 (3%H_2O) was used as fuel with ambient air at the cathode.

This behaviour is in stark contrast to that observed in the Ni-YSZ model cells, shown in Figure 61. The shape of the impedance curve is clearly made up of multiple arcs, but the general shape (relative contribution of LF and HF arcs) does not change dramatically as the temperature is decreased from 750 °C to 600 °C.

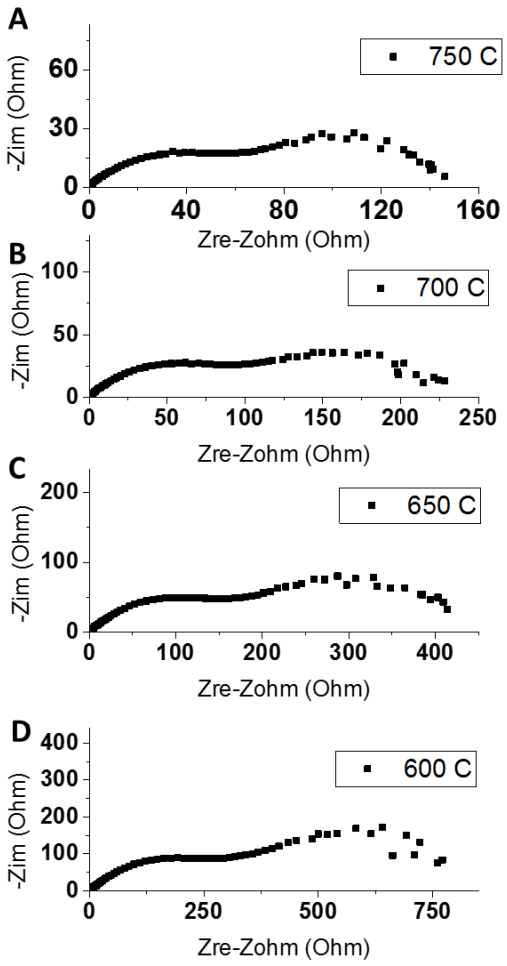

Figure 61 – Representative impedance spectra for embedded mesh Ni-YSZ cell collected between 750 °C and 600 °C (a-d). 60 sccm H_2 (3%H_2O) was used as fuel with ambient air at the cathode

5.4.2 Voltage dependent electrochemical performance of model cells

The embedded mesh model cell operates as a SOFC, in contrast to a symmetric cell, with two different atmospheres over the electrodes, therefore the application of voltage to the model cell provides a more realistic environment for analysis of the anode under operating conditions. Impedance and I-V-P curves were taken for both Ni-YSZ and Ni-SDC embedded mesh model cells. In the Ni-YSZ cells, the resistance of the cell decreases with increased applied potential, and produces the expected curvature transition from activation region (dominated by charge transfer) to the linear ohmic region (dominated by electrolyte resistance). Notice that there is no mass transfer limited region observed in the Ni-YSZ model cell, as expected for the 2D planar surface and 60 sccm flow rate used. In contrast, the Ni-SDC model cell shows an inverse curvature to that of the Ni-YSZ cell, with the impedance of the cell smoothly increasing with applied potential. Since the Rp does not decrease with applied potential, the impedance of the Ni-SDC model cell is likely not dominated by a charge transfer process.

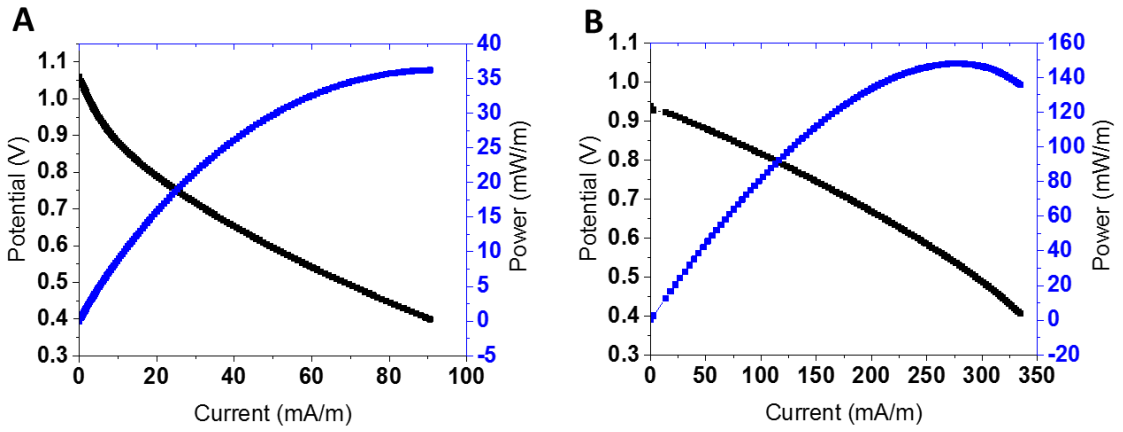

Figure 62 – Representative I-V-P curves for Ni YSZ (a) and Ni SDC (b) model cells collected at 600 °C. Current density has been normalized by the length of the Ni-Electrolyte interface (L_{TPB})

This voltage dependency is also observed when collecting impedance spectra under applied potentials. For the Ni-YSZ case, the application of voltage decreases the anodic polarization, as expected, with no change in the ohmic polarization. In contrast, the Ni-SDC model cells show an increase in both Rp and Rohmic as potential is applied to the cell, as shown in Figure 63.

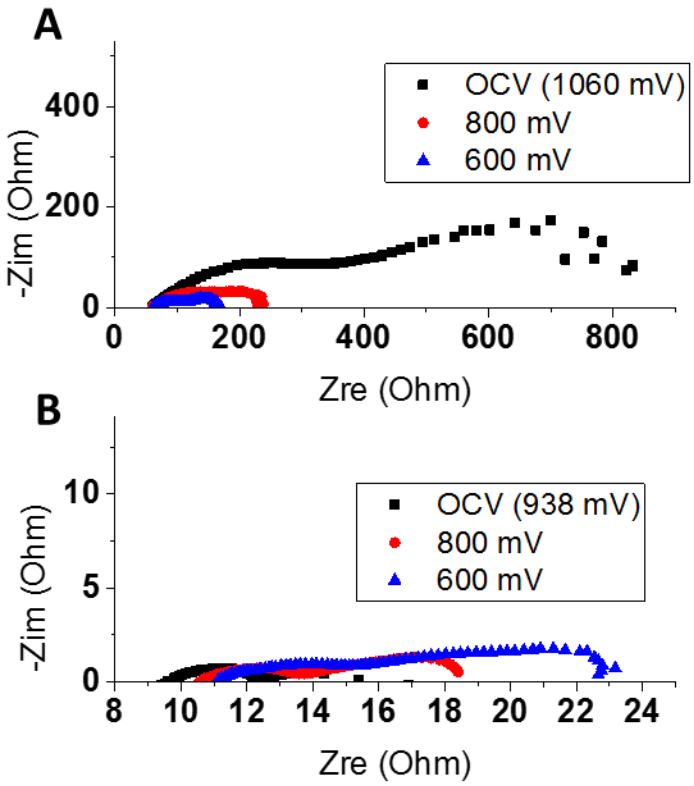

Figure 63 – Impedance spectra collected from (A) Ni-YSZ and (B) Ni-SDC model cells as a function of applied voltage (OCV, 0.8 V, and 0.6 V), collected at 600 °C with 60 sccm H_2 flowing over anode and ambient air over cathode.

A common explanation for increased polarization with applied potential is that the impedance is due to concentration polarization, caused by insufficient flow of reactants to the active site on the Ni-SDC surface, but the effect of gas flow rate was previously shown to have no effect above 60 sccm, as shown earlier in Figure 59. One possible explanation for this behaviour is that there is a solid state diffusion limitation of the oxygen anions and/or electrons to the active sites. It has been hypothesized by several authors that reduced CeO_2 and SDC have significant activity toward H_2 oxidation, independently of the presence of the Ni component.[87,88,96] In combination with the mixed ionic electronic conductivity of reduced SDC, this activity can effectively widen the triple phase boundary with a limited active double phase boundary near the Ni current collector. Chueh et al proposed that the

width of this double phase boundary site was found to be limited by the electronic conductivity of the reduced CeO_2 near the Ni-SDC TPB sites, and that the majority of the H_2 oxidation occurred on the SDC surface near the TPB interface.

Although these proposed explanations may help explain the behaviour observed on the Ni-SDC model cells, further mechanistic understanding of the Ni-SDC interface is not within the scope of this work. These observations are made primarily to set a baseline performance of the Ni-SDC model cell, for its potential use as a screening tool for different functional coatings, as will be described in later sections. By comparing these model cells, the fundamental differences in the anode behaviour are made clear: (i) Ni-SDC shows increased Rp as current is drawn, whereas Ni-YSZ shows decreased Rp, (ii) Rohmic remains constant with voltage in the Ni-YSZ cell, but is increased in the Ni-SDC cell. These observations suggest that the oxidation reaction is fundamentally different at the Ni-SDC interface compared to the Ni-YSZ interface, and in order to effectively identify functional coatings for intermediate temperature SOFC anodes, a Ni-YSZ model electrode will not be sufficient. .

5.4.3 Dependence of Rp on pH_2 and pH_2O

Empirical reaction orders can be determined by plotting the measured activity as a function of the partial pressure of each component on a double logarithm diagram. Then a reaction order can be calculated by fitting the following equation:

$$ln\left(\frac{1}{R}\right) = ln(1/R_0) + n * ln(p_x) \qquad (23)$$

Where R represents the anode polarization, p_x represents the partial pressure of *x* component (H_2 or H_2O) and n is the empirical reaction order. The impedance spectra of Ni-SDC model cells were collected while independently varying the pH_2 and pH_2O composition of the gas over the anode. Three mass flow controllers were used to mix N_2, 3% H_2O humidified N_2, and H_2, at 100 sccm total flow, with ambient air over the cathode. The *n* calculated for the pH_2 variation was 0.24 (standard deviation of 0.04), whereas there was essentially no dependence of impedance on pH_2O variation, with an *n* of -0.0017 (standard deviation of 0.00007). The impedance spectra and logarithmic plots are shown in Figure 64.

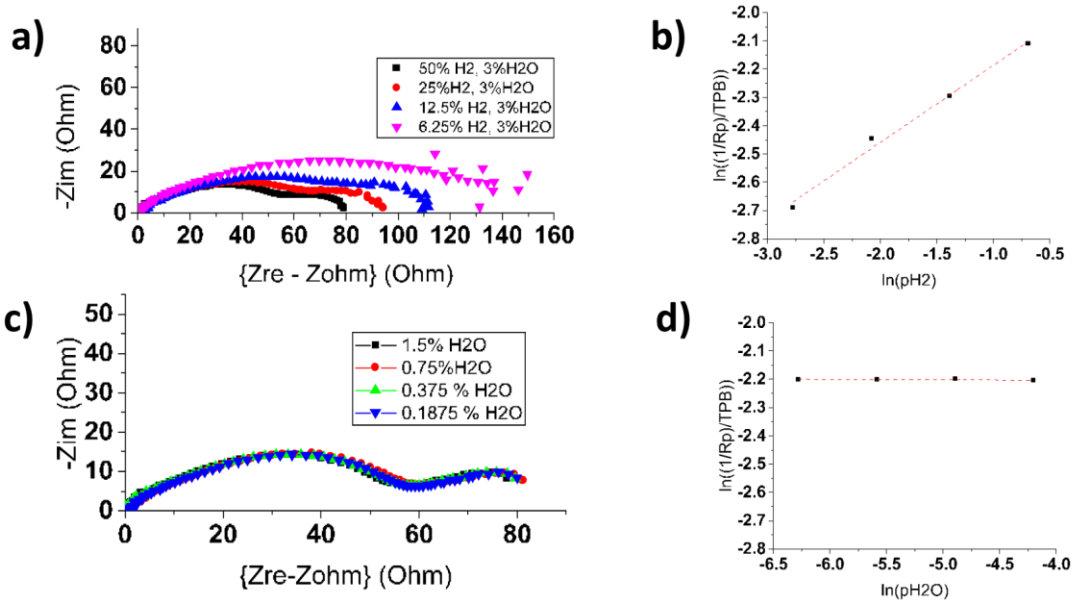

Figure 64 – Dependence of anodic polarization on pH_2 (a,b) and pH_2O (c,d). The slopes of the linear fits, representative of the reaction orders, in (b) and (d) are 0.24 and -0.0017. with R^2 values of 0.94 and 0.96, respectively. Impedance spectra were collected at 500 C while gas compositions over the anode was controlled by three mass flow controllers mixing N_2, 3%H_2O humidified N_2, and H_2 at 100 sccm total flow, with ambient air over the cathode.

The significant dependence of the impedance on the pH_2 supports the assumption that the cell impedance is dominated by the anodic processes; impedance due to cathodic processes should not be effected by the gas composition on the anode side of the cell. Jung et al also observed that bare SDC model anodes showed a strong dependency on pH_2 (0.72), with near negligible dependence on pH_2O (0.09).[97] They proposed that this dependency, in contrast to Ni-YSZ, suggested that the rate-limiting process for H_2 oxidation occurred on the SDC surface near the TPB site, and that hydrogen spillover or proton transfer through adsorbed hydroxyl species were not likely mechanism. Although there are several reports reporting the reaction of SOFC anodes as calculated with various pH_2 or pH_2O, there is little agreement on what mechanisms are responsible for these orders, and therefore assignment of specific reaction mechanisms over Ni-SDC was determined as outside of the scope of this work. This observation is primarily presented to show that changes in anodic atmosphere will adjust total impedance of the cell which supported the assumption of anode dominated impedance.

5.4.4 Calculation of Rp and E_a from impedance spectra

With the key model cell assumptions now validated, the impedance curve can be defined as only the polarization resulting from the anodic processes, allowing a more simplified interpretation of the impedance spectra. Typically, the polarization resistance (Rp) is simply calculated as the difference between the high and low frequency real axis intercepts on a Nyquist plot, but an additional correction was required for these Ni-SDC model cells. The OCV of the cells were substantially lower than the predicted Nernst

potential, because CeO_2 based electrolytes will become partially reduced when exposed to low pO_2 fuels, producing oxygen vacancies and increased electronic conductivity. This electronic leakage current lowers the observed OCV and complicates the measurement of the true interfacial resistance. Impedance spectra collected from a cell with a mixed ionic/electronic conducting electrolyte will exhibit a smaller impedance curve, and therefore calculation of Rp by a simple difference between the high frequency and low frequency intercepts will underestimate the true value.

Following the approach of Liu et al, the Rp values were corrected by applying the measured OCV under the conditions of the impedance scan, and comparing that to the theoretical Nernst potential.[98] This correction stems from the derivation of a transference number expression, which considers the effect of a cell's interfacial polarization.

Briefly, the ionic transference number of a material is defined as:

$$t_i = \frac{I_{ion}}{\sum I_i} = \frac{\sigma_{ion}}{\sum \sigma_i} = \frac{\sigma_{ion}}{\sigma_{ele} + \sigma_{ion}} = \frac{R_{ele}}{R_{ele} + R_{ion}} \qquad (24)$$

These polarization values can be related to the open circuit potential and Nernst potential by:

$$t_i = \frac{V_{oc}}{E_N}\left(1 + \frac{R_p}{R_{ion} + R_{ele}}\right) \qquad (25)$$

By considering the impedance spectra as shown by Nyquist plot, the bulk ohmic resistance (Rohm) can be defined as the high frequency intercept of the impedance loop with the real axis:

$$R_{bulk} = \lim_{\omega \to \infty} \{Z\}G = \frac{R_{ionic}R_{electronic}}{R_{ionic} + R_{electronic}} \quad (26)$$

Similarly, the total impedance, R_T, can be defined as the low frequency intercept of the real axis:

$$R_{total} = \lim_{\omega \to 0} \{Z\} = \frac{(R_{ionic}+R_p)R_{electronic}}{(R_{ionic} + R_{electronic}) + R_{electronic}} \quad (27)$$

Through combination of the above equations, relations for the R_{ele}, R_{ion}, and most importantly, for the R_p of the cell can be calculated from the observations of a standard EIS measurement, namely, the open circuit potential (V_{OC}) and the high and low frequency intercepts of the real axis of a Nyquist plot (R_{bulk} and R_{total}, respectively).

$$R_p = \frac{R_{bulk}-R_{total}}{\frac{V_{oc}}{E_N}\left(1 - \frac{R_{bulk}}{R_{total}}\left(1 - \frac{V_{oc}}{E_N}\right)\right)} \quad (28)$$

Indeed, the ionic transference numbers ranged from ~0.80 to ~0.96, with higher t_i observed at lower temperatures (Figure 65). This highlights the need for the Rp correction shown in Equation 28, as without this correction the anodic Rp would be largely underestimated (for example, a cell presenting an OCV of 849 mV at 750 C would underestimate the Rp as 0.116 Ohm, when the corrected value would be 0.195 Ohm). All R_p values presented in this work, or used for further calculations, have been subjected to the equation above.

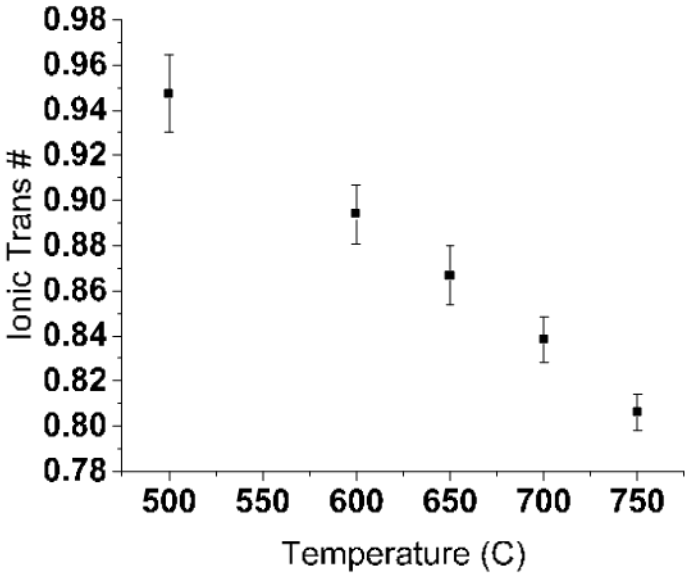

Figure 65 – Calculated ionic transference numbers for Ni-SDC model cells between 500 C and 750 C, measured with 60 sccm humidified H_2 flowing over the anode, and ambient air over the cathode. Error bars represent one standard deviation of the calculated results.

Collecting Rp values at different temperatures, and applying the values to an Arrhenius plot, activation energies can be measured for the dominant anodic process, as shown in Figure 66. The activation energy for the ohmic resistance was calculated as 0.74 eV (σ = 0.05), in agreement with several conductivity studies for SDC electrolytes, representative of the diffusion of oxygen anions through the lattice.[99] The activation energy calculated for the Rp was and 1.09 eV (σ = 0.13). This value is within the broad range of values reported for H_2 oxidation over Ni based anodes, although is higher than that measured for Ni-YSZ in this work (0.86 eV . σ = 0.03) suggesting that there may be a different rate limiting processes for Ni-SDC compared to Ni-YSZ anodes.

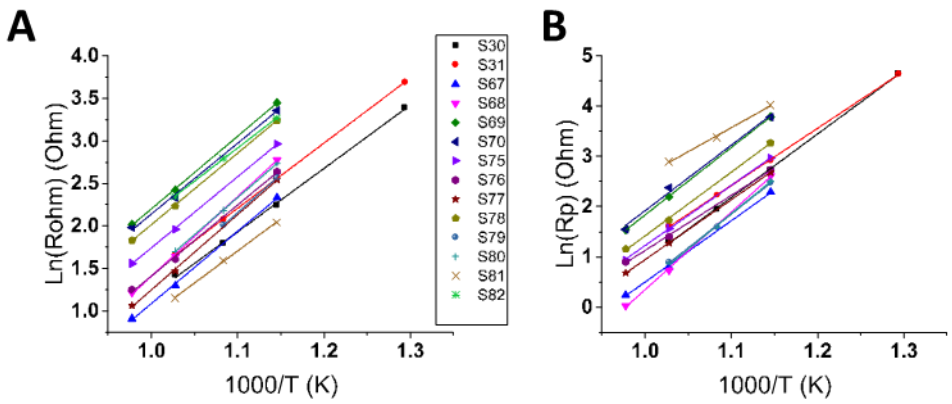

Figure 66 – Arrhenius plots for R_{OHMIC} (a) and R_{ANODE} (b) collected from several embedded mesh model cells. Humidified hydrogen was flowed over the anode at 60 sccm or above, with ambient air over the cathode. Linear fits were used to calculate the slope for each sample, yielding 0.74 eV (σ = 0.05) for R_{OHMIC} and 1.09 eV (σ = 0.13) for R_p.

5.5 Use of embedded Ni-mesh model anode to investigate anode activity

5.5.1 Quantification of anodic activity as function of L_{TPB}

The activity of an SOFC anode will scale with the number of active sites, therefore in order to quantify the catalytic activity of a specific material, the activity must be normalized by the relative amount of these active sites. One of the main advantages of the embedded mesh architecture is the straightforward observation and estimation of the L_{TPB}. With this information, the inverse of Rp, here defined as activity ($1/R_p$) following the approach of Jung et al[97,100] can be normalized by the number of active sites (assuming the active sites are limited to the interface of Ni and SDC, the triple phase boundary), and the performance of individual materials can be more rigorously compared across different cells with different L_{TPB}.

In Figure 67, the process for calculation of the L_{TPB} is described. Since the measurement of length will change with magnification, a simple 5X optical image was used to estimate the length. This reduces the resolution of the measurement but avoids measurement defects and anomalies that may occur at the interface. Using the open source imageJ software package, the image is converted to 32 bit greyscale. By adjusting the thresholding of the image, the Ni mesh is first defined as a single particle and with a defined geometry (perimeter, area, etc). Then the electrolyte regions fully enclosed by Ni-mesh are redefined as several particles, and their perimeters are summed and added to the bulk mesh perimeter. This results in values of anode area and triple phase boundary length.

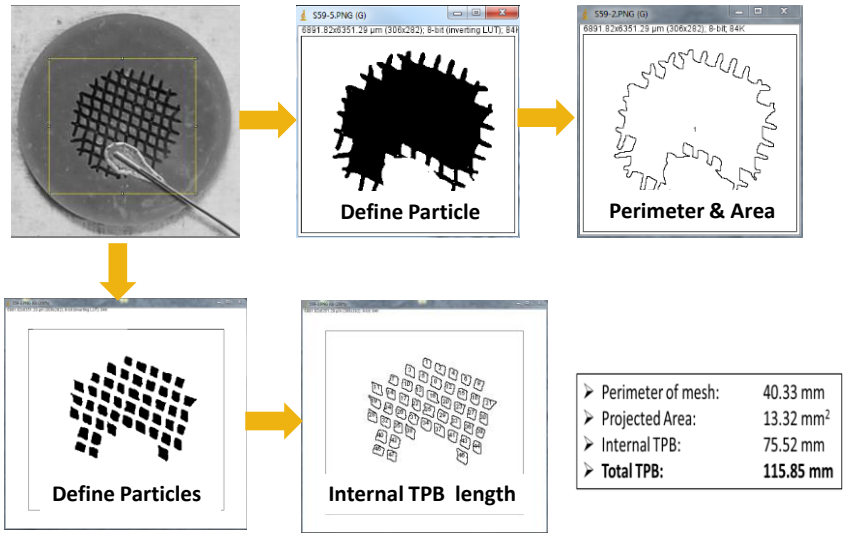

Figure 67 – Process of L_{TPB} estimation using ImageJ software package. An optical image is first translated to a 32 bit grey scale. Then the mesh is defined through contrast definition to form particles, whose perimeters combine to give the L_{TPB}.

To calculate the normalized activity of the triple phase boundary, the activity value ($1/R_p$) was divided by the measured L_{TPB} of that cell. Average activity values for both Ni-SDC and Ni-YSZ embedded mesh cells are charted in Figure 68 as a function of temperature..

It's important to note the y-axis scale difference between, the Ni-SDC and Ni-YSZ data, as the Ni-SDC anode exhibits roughly two orders-of-magnitude higher L_{TPB} normalized anodic activity.

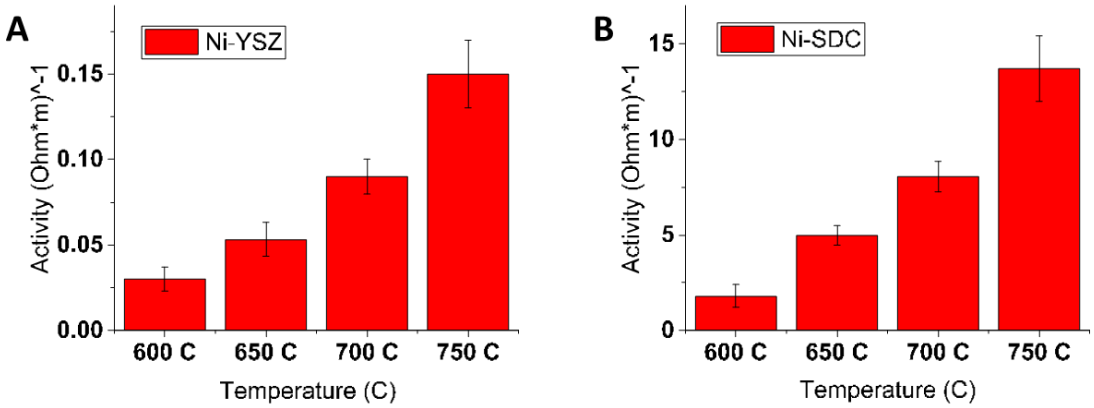

Figure 68 –L_{TPB} normalized activity values for (A) Ni-YSZ and (B) Ni-SDC model cells with 60 sccm H_2 at anode and ambient air over porous LSCF cathode. Error bars represent one standard deviation of the data. Please note the different y-axis scale between (a) and (b).

Clearly, the inherent activity of the Ni-SDC interface is higher than that of the Ni-YSZ interface. This result further supports the transition away from YSZ based anodes for intermediate temperature use, and suggests that significantly higher activity may be achieved for cells with Ni-SDC anodes compared to Ni-YSZ.

5.5.2 Observation of Triple Phase Boundary length dependence for model cells

Previous studies utilizing patterned model anodes have consistently concluded that the hydrogen oxidation reaction occurs only at the triple phase boundary site by measuring the Rp of cells with varying L_{TPB} and applying the following equation:

$$R_p = R_{p,0} * l_{TPB}^{-\alpha} \quad (29)$$

Where the exponent α should yield a value of 1 if the rate limiting step of the reaction is limited to the TPB.[84,86,92] Previous works often give results short of this value, explained by the difficulties in preventing the TPB of a Ni thin film from changing during exposure to the high temperature reducing atmospheres required for testing (e.g. delamination, grain coarsening, or void formation can all increase the true TPB length).

This relation was applied to the data collected from the embedded mesh cells, in order to confirm the assumption that the model cell anode was indeed limited by the TPB. The R_p of bare Ni-mesh cells were plotted as a function of the measured L_{TPB}, and this data was fit to an Allometric equation (y= aX^b) using OriginPro 2016. From equation (29), if the site is limited to the triple phase boundary location, the α value should be equal to 1. An alternative approach is to plot the data in log-log plot and run a linear fit. The rational for this method is that the slope of the linear fit should be equivalent to the negative of this α term. Both plots and the calculated values are shown in Figure 69.

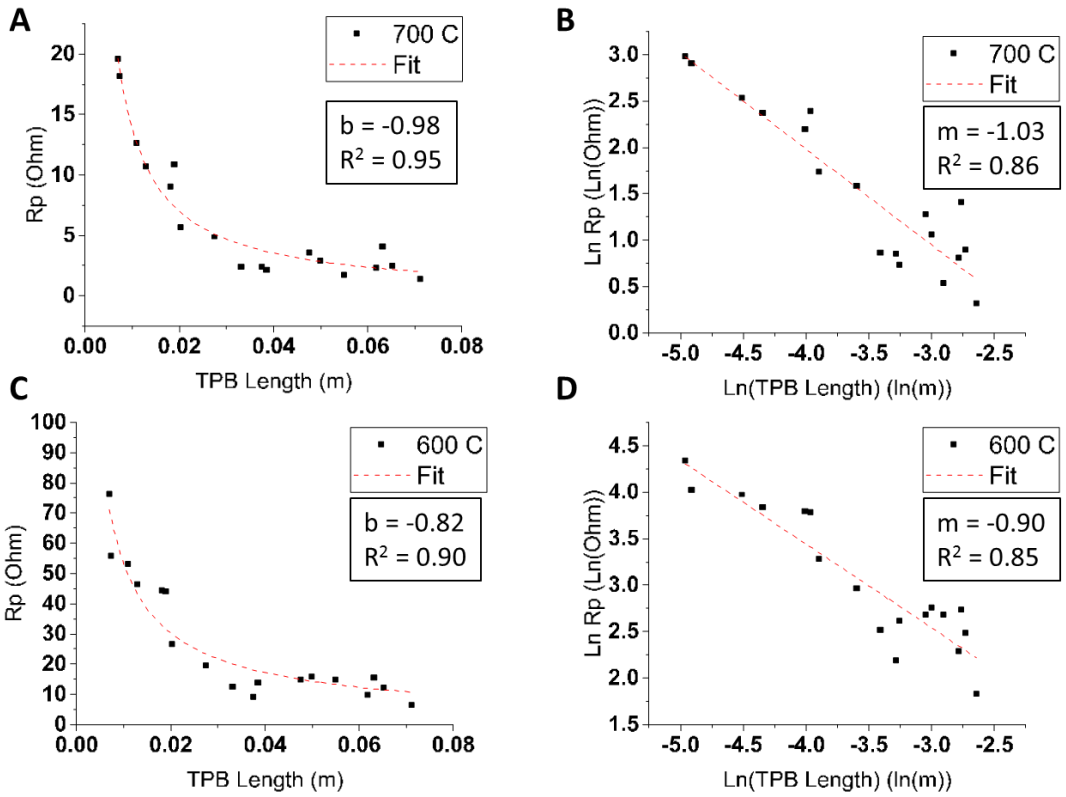

Figure 69 – Rp and Ln(Rp) (a, c) as a function of L_{TPB} collected at 700 °C (a,c) and 600 °C (b,d). Dashed lines represent (a,c) allometric ($y= ax^b$) and (b,d) linear (y=mx+b) fits

Indeed, as the TPB length increased the R_p of the model cell decreased, with α values near the 1.0 value predicted. Interestingly, as the temperature was reduced, there was a larger deviation from this α term, but these values remain within the range reported by other patterned anode works and verify the assumption that the embedded mesh model cell polarization with the L_{TPB}. Most importantly, this result supports the use of the embedded Ni-SDC platform in the quantification of site anodic activity. Since the activity was found to scale with L_{TPB}, the basic activity of different materials may be confidently calculated and compared by normalizing the activity ($1/R_p$) by the measured L_{TPB}.

5.6 Activity modification through deposition of functional coatings

One of the primary advantages of the open architecture of the embedded mesh architecture is the relative ease of material deposition through line-of-site coating techniques, for example DC or RF sputtering. Since the activity of the cell (defined here as $1/R_p$) is limited by the anode, by depositing different materials on the model anode surface the effect of different coating materials on performance can be quantified and compared. In this way, the model cell can be used to confidently screen different functional coatings for improved SOFC performance, either through improved activity or stability to corrosion. This strategy was demonstrated in this section by comparing a variety of candidate functional coatings, including CeO_2 films with small amounts of Ru, Ni, and Pt dopants.

Films were deposited through RF (ceramic targets) or DC (metal targets) sputtering, as described in Section 3.2.3. Coating thicknesses and growth rates are listed for tested coatings in Table 7, measured by SEM cross-sections taken from silicon wafer substrates coated simultaneously along with the polished model cells (Figure 70).

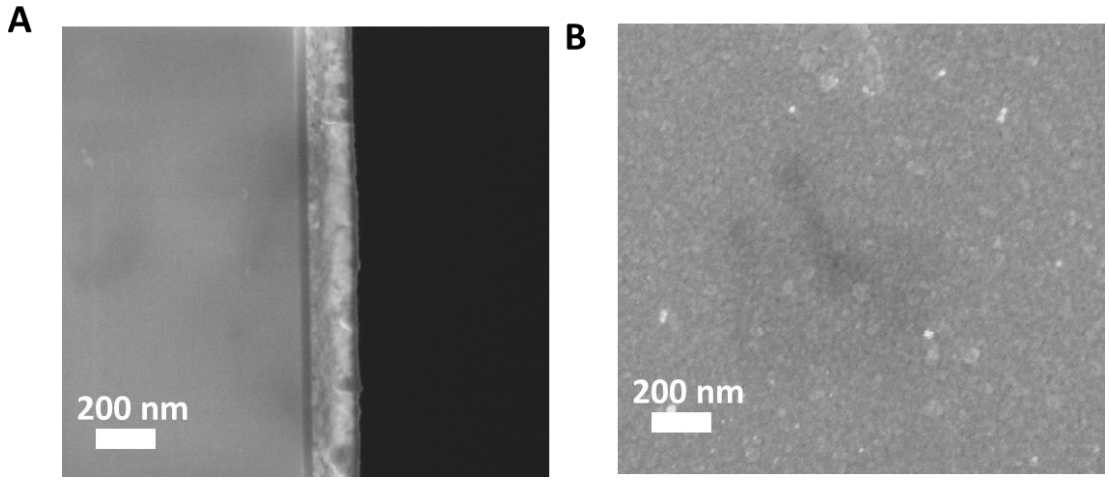

Figure 70 – (a) Cross section and (b) top-down SEM of SDC films sputtered on a clean Si wafer for 120 min at 15 W, vacuum pressure set 6.3 E-3 mBar by flowing 45 sccm Ar into the chamber.

Table 7 – Growth rates resulting from DC or RF sputtering for catalyst coatings, as measured by SEM cross-section on Si substrates. RF sputtering conditions were 15 W at 6.3E-3 mBar, DC conditions were 65W at 3.4e-2 mbar.

Material	Growth Rate (nm/min)
SDC	0.70
Ru-metal (DC)	5.1
Ru/Ni/Pt-doped CeO_2	0.73

XPS analysis of the films confirmed a significant amount of ionic dopant was present in each film, and these dopants remained largely ionic after testing. The raw composition of each film, as well as the dopant:Cerium ratio, is included in Table 7.

Table 8 – Elemental composition of deposited catalyst films tested in this work, collected by XPS survey scan data.

	SDC	Ru	$RuCeO_2$	$NiCeO_2$	$PtCeO_2$
Dopant:Ce ratio	0.22		0.04	0.26	0.54
O1s	45.71	49.12	81.35	71.1	52.84
Ce3d	5.67		9.90	11.28	5.35
4Sm3d	1.27				
C1s	47.35	36.29	8.33	14.68	17.13
Ru3p		8.26	0.42		
Ni2p		6.34		2.94	20.81
Pt4f					2.88

The Ruthenium and Ni doped films were able to retain their cationic state, with the Ru 3p binding energies of 463.7 eV and 463.0 eV for the as sputtered and tested coatings, respectively. Recall from Table 1 (chapter 4) that metallic Ruthenium shows a 3p binding energy of 461.2 eV. Similarly, the Ni 2p binding energies were 853.8 eV and 853.0 eV for the as sputtered and tested coatings, respectively, and the binding energy for metallic Ni^0 is only 852.4 eV. As observed for the nanoparticle catalysts described in chapter 4, the CeO_2 lattice has a substantial ability to stabilize Ru and Ni in ionic states, even after exposure to high temperature reducing conditions. The platinum doped films showed a more, although cationic Pt was observed for the as-sputtered films, the tested coatings showed substantial amounts of both ionic and metallic Pt, with a new peak appearing at 66.1 eV in addition to the cationic Pt peak at 72.22. This is likely due to the much higher

Pt loading of the sputtered $PtCeO_2$ films, relative to the $RuCeO_2$ and $NiCeO_2$, as the stability of the ionic state is more likely as lower doping levels.

The activity of the SDC film lowered the activity of the cell, as the ceramic phase covered the active Ni sites. Still, it's important to note that the relatively thick film of SDC (~120 nm) only decreased the activity by ~50%, demonstrating that a pure SDC surface does have reasonable electro catalytic activity toward H_2 oxidation. As expected, the addition of a film of porous Ruthenium (65 W with 130 sccm Ar, 3.4E-2 mbar, following the approach of Takagi et al[101]) on the Ni-SDC surface dramatically increased the activity, likely due to both its intrinsic activity toward H_2 oxidation, as well as its electronic conductivity creating additional triple phase boundary sites on the surface, beyond the Ni-SDC interface. In a similar fashion, the activity and impedance spectra of ionic Ru, Ni, and Pt doped CeO_2, were collected and compared (Figure 71). Ionically doped films were deposited using a composite target fabricated by wrapping a wire of the noble metal around a dense CeO_2 target, following the methodology of Matolin et al.[102] XPS analysis of the films confirmed a significant amount of ionic dopant was present in each film, and these dopants remained largely ionic after testing.

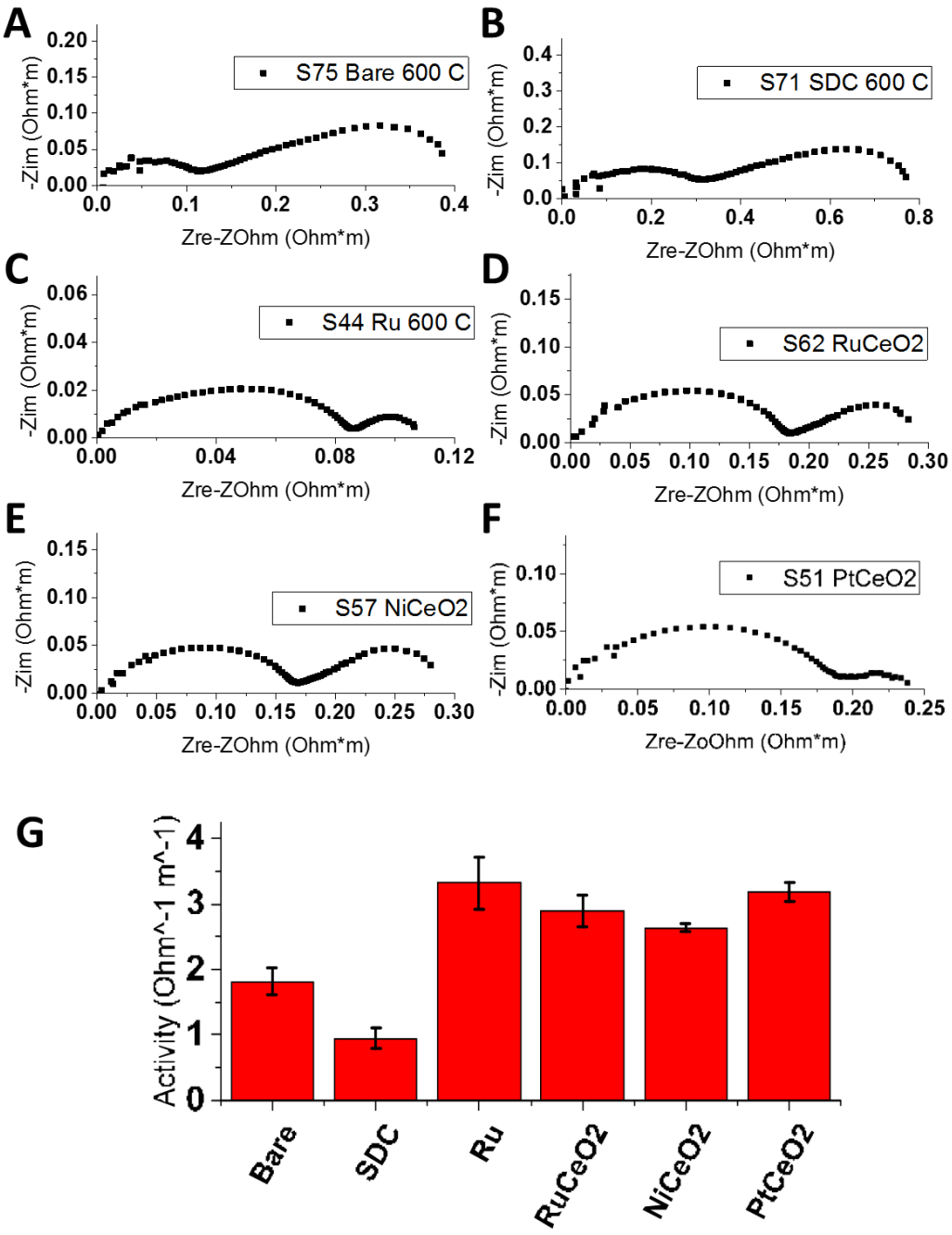

Figure 71 – Representative TPB normalized impedance spectra for (A) bare Ni-SDC, (B) SDC coated, (C) Ru coated, (D) Ru-CeO_2 coated, (E) Ni-CeO_2 coated, and (F) Pt-CeO_2 coated model cells, each collected at 600 °C with 60 sccm humidified (3%H_2O) H_2 flowing over the anode, and ambient air over the cathode. The L_{TPB} normalized activities are given in (G), error bars represent one standard deviation of the data.

The presence of a functional coating decreased the relative contribution of the low frequency arc observed for these model cells. Although there was only a subtle effect for the plain SDC coating (which showed the least activity), the higher activity coatings significantly affected the spectra, suggesting that a different reaction process has become rate-limiting over the coating anodes, relative to the bare cells. This is supported by the changes in activation energy of the coated model cells, calculated by measuring the Rp of each cell at temperatures between 600 °C and 750 °C and applying a linear fit to an Arrhenius plot. The presence of any coating significantly increased the E_a for the anodic reaction (Table 9).

Table 9 – Activation energy values measured from model cell Rp between 600 °C and 750 °C in 60 sccm H_2 fuel over anode with ambient air over cathode

Cell Type	E_a (eV)	Stdev (eV)
Bare Ni-SDC	1.09	0.13
SDC coated	1.29	0.1
Ru coated	1.31	0.01
$RuCeO_2$ coated	1.50	0.09
$NiCeO_2$ coated	1.39	0.13
$PtCeO_2$ coated	1.33	0.08

This result demonstrates the applicability of these model cell in the comparison of different functional coatings for SOFC anodes, and introduces the potential use of noble metal doped CeO_2 as an attractive candidate SOFC anode electrocatalyst for future development.

5.7 Design and fabrication of Operando SOFC chamber

The ability to characterize materials in the environment they are operated in is essential in the advancement of materials-based devices. Raman spectroscopy is an ideal characterization technique for operando experiments, since it doesn't require high vacuum conditions or physical contact. A number of in situ studies of fuel cell materials have been conducted by using an optical hot stage with controlled atmosphere, which can replicate the temperature and reactive gas environments.[24,25] Although this has provided critical information on the operation and corrosion of SOFCs, the single atmosphere condition does not accurately replicate the true operating conditions of the device, as a traditional full cell requires separate atmospheres for the cathode and anode to provide a chemical potential (OCV) and efficient flux of ionic species (O^{2-}). Although voltage can be applied on a symmetric cell, this again does not fully replicate the conditions of a full cell, since the atmosphere is identical at both electrodes. This is especially important when studying SDC based SOFCs, since the entirety of the electrolyte will become reduced in a symmetric cell, dramatically affecting the electronic and ionic conductivity of the electrolyte. The number of SOFC studies using operando Raman are rare, and therefore there is a present need to improve this characterization technology.

Button cell testing (described in section 3.1.2) is the work-horse of the SOFC academic community as it allows small scale prototype testing without the need for complicated stack construction. The information gained is primarily dominated by electrode behavior rather than macroscale effects such as gas flow, temperature management and fuel utilization, which are important issues but not directly related to materials chemistry. By fully replicating the button-cell testing apparatus within a Raman compatible chamber, there is less ambiguity between the conditions of a cell in the testing furnaces and one in the

operando furnace, and therefore the results are expected to be more meaningful to the SOFC device community.

There are a few contemporizes who have attempted to address this issue. Robert Walker's group has been especially prolific in this area, and have recently published many works using a home built system for operando Raman SOFC experiments, as well as operando experiment using several other optical techniques.[103-105]. Their system, shown in Figure 72, allows full button cell testing, but there are several drawbacks. The design is essentially a vertically mounted furnace placed underneath a custom optics system which guides the beam path into the furnace from a Raman system. This system is effective, with the ability to collect Raman signal from working SOFCs at temperatures as high as 800 °C with full control over both anodic and cathodic atmospheres. Still, there are several key drawbacks of this design. The system is relatively large, and is not directly compatible with a standard Raman microscope stage. This limits the adaptation of this design to other groups, and restricts the use of the Raman system to only operando experiments while the furnace is assembled. Critically, by not using a motorized stage to support the SOFC, there is no spatial resolution or mapping capability. Due to the composite nature of SOFC anodes, different regions of the cell can have dramatically different reactions taking place and this system is not able to distinguish on which component these reactions are occurring.

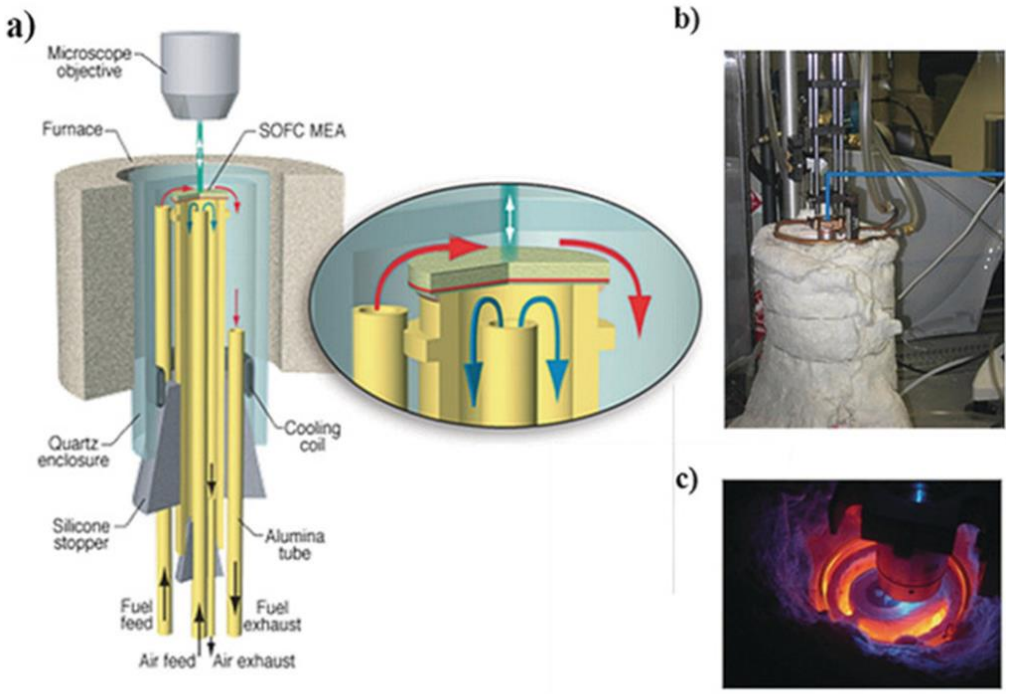

Figure 72 – Operando Raman SOFC apparatus designed and fabricated by the Walker group. Cross-section diagram is shown in (a), highlighting the anode and cathode chambers contained within the quartz tube under the optical path, (b) photograph of the operando system, including vertically mounted split-tube furnace and custom microscope optics (beam path shown by blue line). (c) Photo of anode surface during operation. Figure reproduced from Kirtley et al.[105]

Although the work done within the Walker group is the most prominent, there are a few alternative designs available in the literature. Brightman et al designed a miniaturized system that fits a standard optical stage, as described in Figure 26.[106] This design satisfies the requirement that the cell is mounted on a motorized stage for spatial resolution and mapping capability, while still reaching high operating temperatures (700 °C) and providing true SOFC operation with both cathode and anode atmosphere control. While a strong design, the complicated mounting and assembly of the unit does not replicate button-cell testing, and may introduce inconsistencies when compared to standard cell testing methodologies.

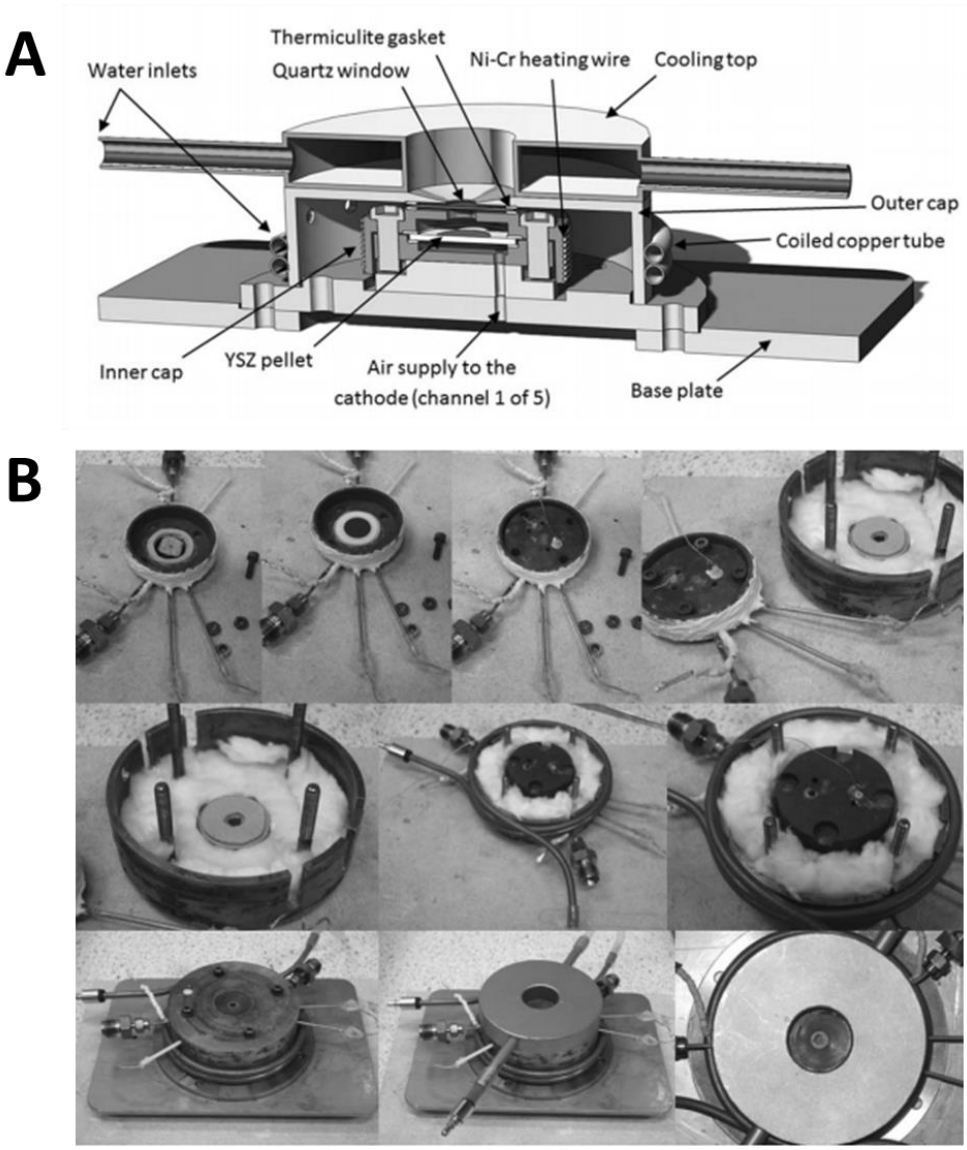

Figure 73 – Schematic (A) and photographs (B) of Brightman et al's design of an operando Raman chamber, highlighting the internal gas distribution cell mount, surrounding heating elements and insulation and outer water cooling coils. Figure reproduced from Brightman et al.[106]

There are currently no commercially available operando SOFC testing systems available, and therefore to improve the testing capabilities of the Liu group at Georgia tech, a new

design was proposed, making use of the lessoned learned through the previous designs described above.

In this design of an operando chamber there were a number of key functionalities: (1) the ability to test a full SOFC mounted as a button-cell (separately providing air and fuel to the cathode and anode, respectively); (2) the ability to reach temperatures in excess of 700 °C; (3) optical and electrochemical feedthroughs, allowing site-specific simultaneous collection of electrochemical and Raman spectra; and (4) relative simple construction, that can be adapted to common Raman systems and fabricated by other academic groups or companies. A drawing of the initial design is shown in Figure 74. A vertically mounted button cell supported on an alumina tube is inserted from the bottom of a rectangular chamber. A heating platen surrounds the cell at the end of the alumina tube, directly below an optical viewport. Feedthroughs for electrical connections, thermocouples, and gas flow are inserted from the sides.

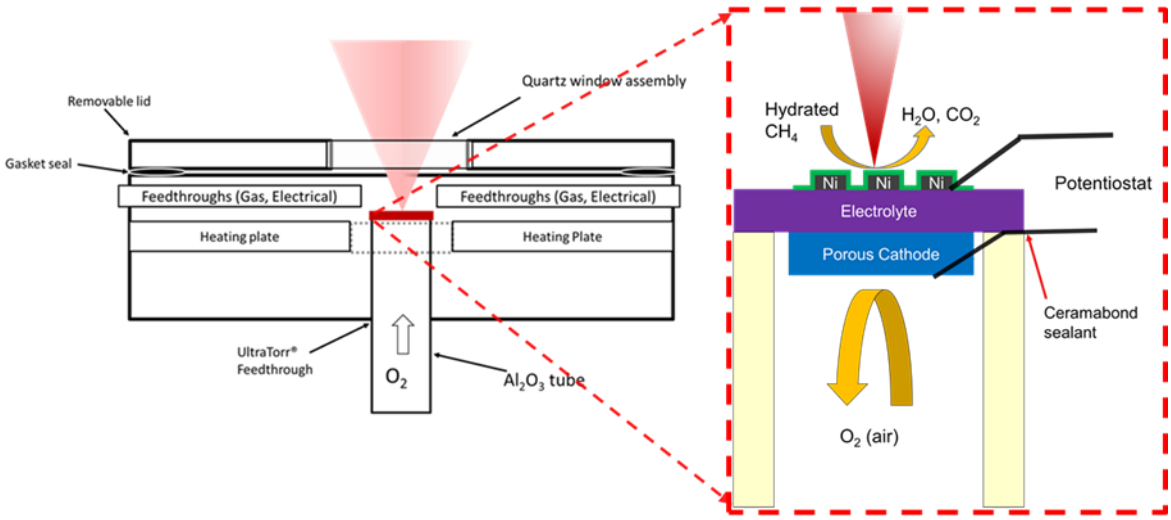

Figure 74 – Schematic of basic operando system design, including highlight of patterned model cell mounted on the end of an inserted alumina tube to replicate button cell type testing.

A 3D model of the final design of the chamber (after several iterations) is shown in Figure 75, the chamber is precisely machined to fit the standard cell culture plate perimeter used in many optical systems, so that it seats firmly into the motorized microscope stage (Prior ProScan II). The chamber is opened and sealed by use of a rectangular lid, which is placed over a high temperature silicon O-ring and compressed with four bolts against the main housing. The lid contains a quartz window assembly in its center, directly above the location of the SOFC button-cell. A rectangular platen (2.0” x 2.0” x 0.5”) is used to heat the cell, suspended in the center of the chamber by two heating cartridges (3/8” 300 W Watlow Firerod® with 2” hot zone) inserted horizontally into the chamber through two 0.5” diameter compression fittings (Swagelok Ultra-torr®). Platens fabricated from copper, 304 stainless steel, and titanium have been tested, and can be selected as per the requirements of the experiment. 304 stainless steel has the lowest thermal conductivity,

which increases the difference between sample and set platen temperature. In addition, the stainless steel may introduce chromium based contaminates into the chamber (which may be preferable for the study of Cr poisoning). Copper provides the greatest thermal conductivity but may have some catalytic activity towards reactions studied in chamber. Titanium is a good option, as it is less catalytically active while having no volatile corrosion species while still a better thermal conductor than 304 stainless. The platen has a 0.5" diameter hole bored in its center, which surrounds the SOFC during operation for direct heating of the sample. The SOFC is supported on a 0.5" Alumina tube, which is inserted from the bottom of the chamber through an O-ring sealed feedthrough (Swagelok Ultra-torr®). Three k-type thermocouples are used to measure the temperature of the heating platen, sample, and outer surface. The platen temperature is used for PID control, as it has a faster response time than the temperature of the sample. Electrical connections are made to the cell through two copper feedthroughs in the front of the chamber.

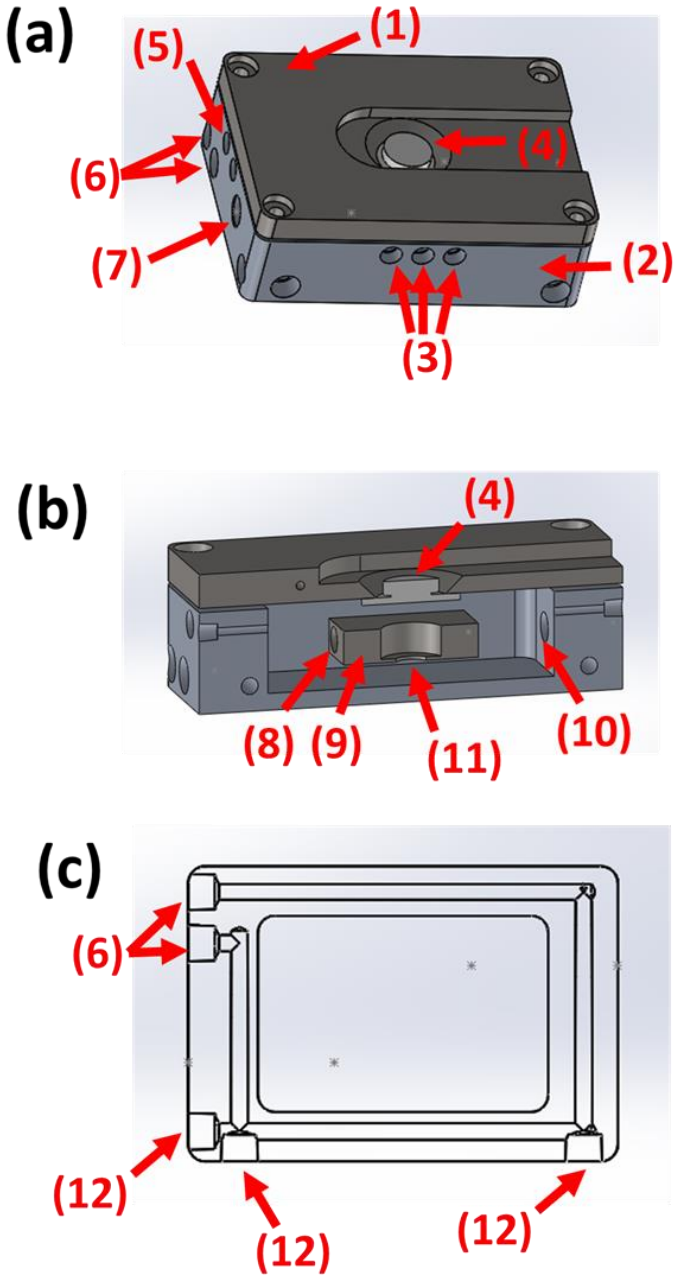

Figure 75 – Schematics of the operando chamber (a) outside from front (b) vertical cross-section through heating platen, and (c) horizontal cross-section of cooling channels. The numbered components refer to (1) Lid (2) Main housing, (3) Feedthrough positions for electrical connections and thermocouples, (4) Quartz window assembly, (5) Feedthroughs for gas input and exhaust, (6) Input and output for water cooling channels, (7) Feedthrough for left heating cartridge, (8) cartridge hole in heating platen, (9) heating platen body, (10) Feedthrough for right heating cartridge, (11) Feedthrough for Alumina button-cell support, (12) plugs required for the machined water channels

Due to the high temperatures required for SOFC testing, efficient cooling of the housing is critical. 0.25” diameter channels were drilled in both the main housing and the chamber lid, and a water-cooling system was used to flow chilled water through the Aluminum housing. Although the melting temperature of Aluminum (660 °C) is within the sample testing range, the thermal conductivity of Aluminum is relatively high compared to other available readily machined metals (e.g. Stainless Steel) and can be easily cooled. Alumina fiber insulation is packed between the housing and the heating platen, which allows a large but stable thermal gradient between the outside surface and heated region. The main components of the operando chamber were fabricated in the Georgia Tech machining mill. Photographs of the cell after final assembly are shown in Figure 76.

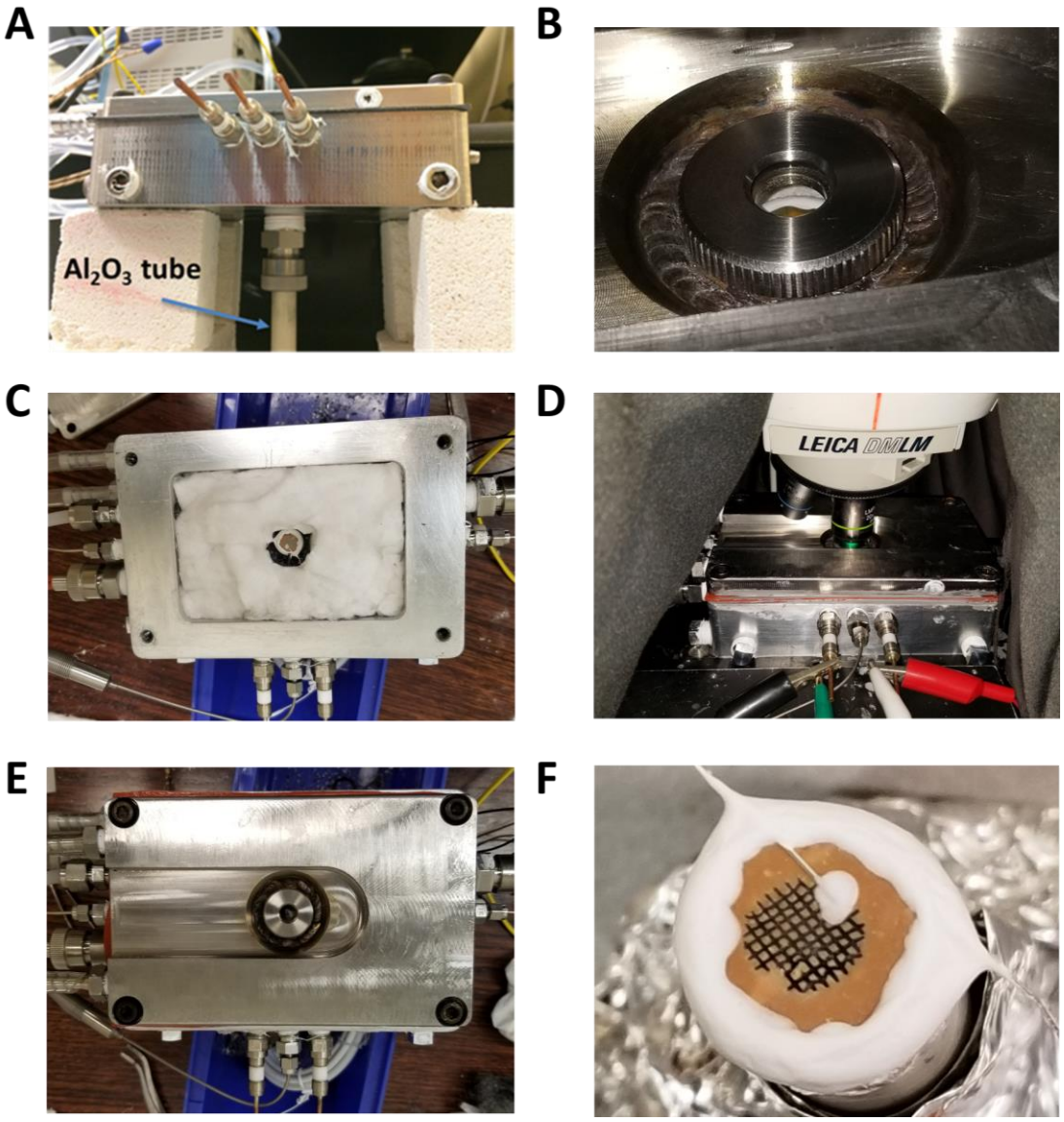

Figure 76 – Photographs of the final version of the operando cell highlighting (a) electrical feedthroughs and button cell insert, (b) optical viewport, (c) mounted cell inside chamber packed with insulation, (d) installation in the Raman system stage, (E) top-down image of lid with compression bolts for O-ring and machined slot for objective placement, (F) sealed model cell before insertion into operando chamber

The temperature of the cell components were tracked and controlled using an in-house Labview® program, (written and graciously provided by Ryan Murphy). There was a significant difference between the heating platen temperature used and the sample

temperature, therefore both temperatures were tracked by the program. The platen temperature was used for the PID control, as it provided much better response to the applied signal and therefore more stable temperature control. The temperature of the cooled housing was also tracked by the program; in the event of a cooling system malfunction, the program would automatically shut down the system once the housing reached 90 °C or above. A plot of sample and chamber outside surface temperature as a function of platen temperature is shown in Figure 77.

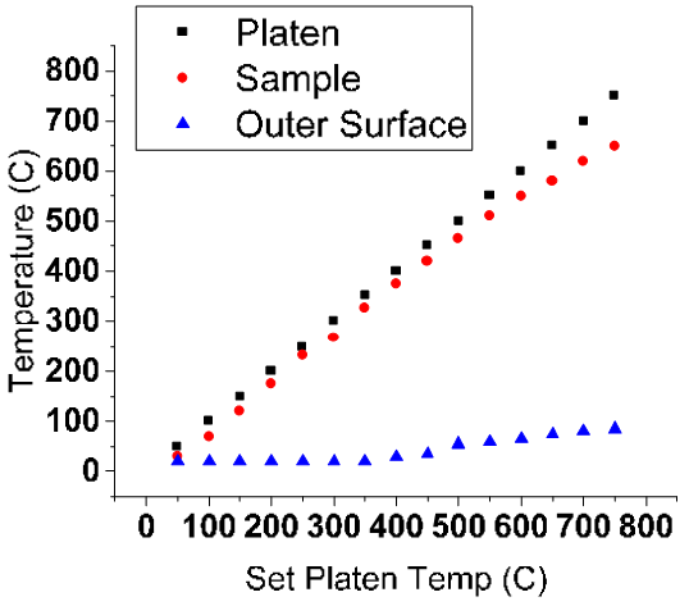

Figure 77 – Plot of measured Sample and operando chamber outer surface temperatures as a function of platen set point. Operando chamber was cooled during measurement by a chiller set to 20 °C, cell was held at each temperature for 30 min before recording the sample and outer surface data points.

The reactive atmospheres are controlled by mass flow controllers paired with a simple manifold connected to necessary gas tanks (Nitrogen, H_2, Hydrocarbon (e.g. methane or propane). Electrochemical, optical, and thermal control of the system is achieved through a CPU interface. A diagram of the system is shown in Figure 78.

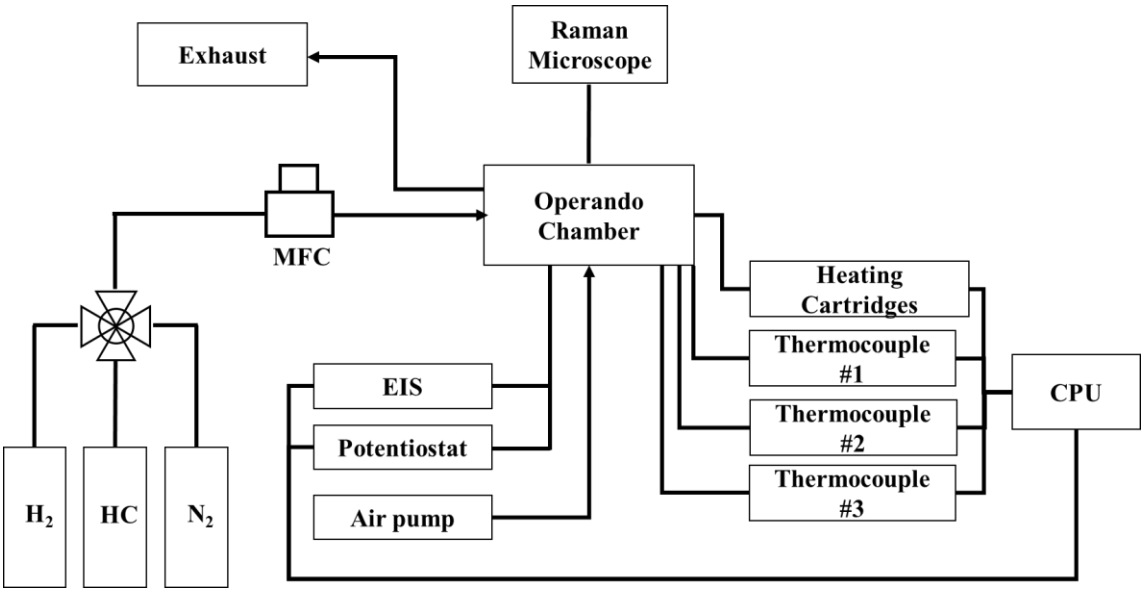

Figure 78 – Schematic flow diagram for the operando testing system.

Collection of Raman spectra at elevated temperature is not trivial. The quartz window cuts the intensity of the signal, and the high temperature cause the sample to emit IR radiation which can elevate the baseline noise of the Raman spectra. Selection of lower wavelength lasers and increasing incident power and collection times can address most of these issues. A representative example of a Raman spectra collected from a Ni-SDC model cell (SDC region) is shown in Figure 79. As the sample is heated in H_2, it is observed that the SDC surface is reduced, as the D:F_{2G} peak ratio (described in section 4`.6.1) is markedly increased, and the F_{2G} shows a subtle shift to lower wavenumbers.

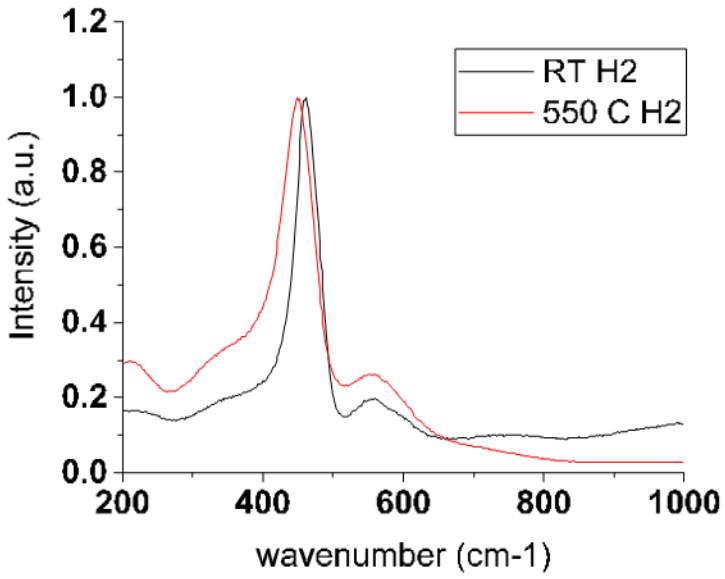

Figure 79 – Raman spectra collected from sample mounted in operando chamber at room temperature and at 550 °C. H_2 was flowed into the chamber at 100 sccm while ambient air was supplied to the cathode side achieving an OCV of 949 mV

5.7.1 Electrochemical behaviour of cells tested in operando chamber

To validate the use of the operando chamber for full button cell testing, embedded mesh Ni-SDC/LSCF cells were mounted in the chamber and their electrochemical behavior was characterized following similar tests as described earlier. Figure 80 shows the I-V-P and impedance spectra collected from the cell at 600 C, within the operando chamber. The I-V-P curve is similar to that collected in a traditional SOFC testing furnace for a model cell, as is the impedance spectra (see section 5.3.3 and 5.3.4). It's important to note the cell achieved a reasonable OCV of 0.94 V, demonstrating the quality of the sealing and successful separation of the anode and cathode atmospheres.

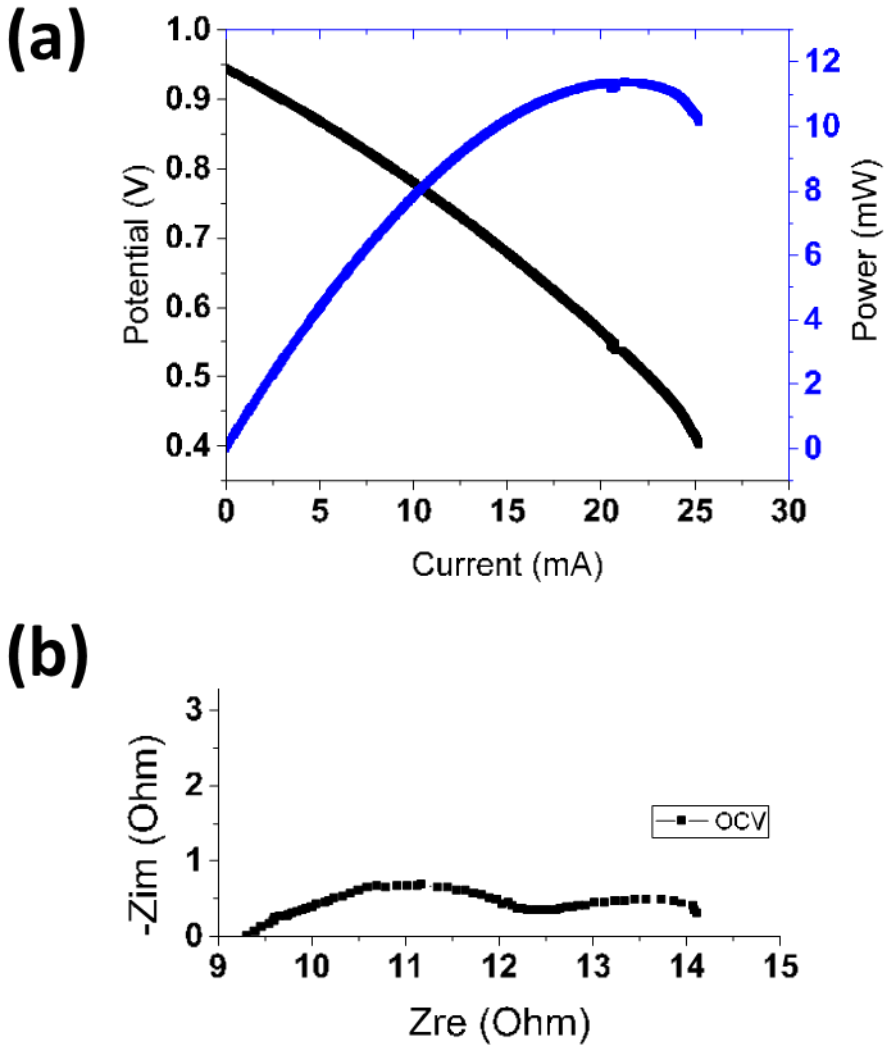

Figure 80 – (a) I-V-P curve and (b) EIS spectra of embedded mesh model cell collected within operando chamber at 600 °C, with 50 sccm H_2 flowing into the chamber with ambient air over the cathode

In addition, the electrochemical behavior of the model cells observed in the traditional SOFC testing furnaces is replicated in the operando chamber. As current is drawn from the cell, the impedance of the cell is increased. The impedance as a function of voltage is shown in Figure 81.

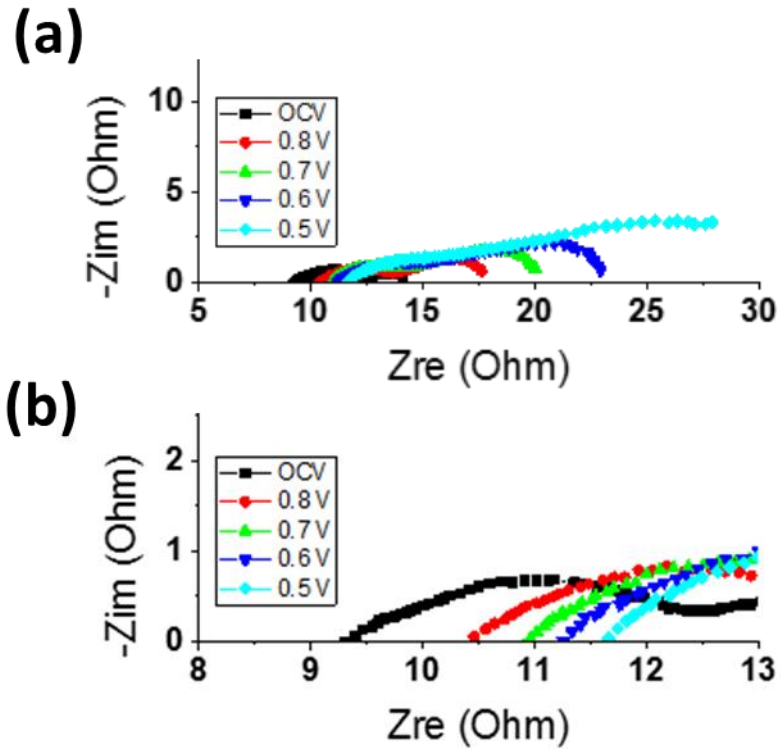

Figure 81 – Representative impedance of Ni-SDC model cell collected within the operando chamber at 600 °C while varying the potential of the cell.

As described earlier, both the Rohmic and Rp impedance are increased as the voltage of the cell is decreased from OCV. This replication of electrochemical behavior demonstrates the applicability of the operando chamber in the analysis of full cell electrochemical phenomena. Raman spectra collected from these samples should therefore be a true representation of the chemistry that is occurring during full cell testing, and is ready for use as a new tool in the investigation of SOFC materials under full operating conditions.

5.8 Conclusions

Taken together, the experiments described above lead to several important conclusions. First, the embedded mesh Ni-SDC model cell has been successfully demonstrated as a useful platform for characterizing intermediate temperature anode materials. These cells replicate basic SOFC function, establishing a reasonable open cell voltage (OCV) when H_2 is flowed over the Ni-mesh side while ambient air is used on the cathode side. The impedance of the cells has been shown to be dominated by the anodic processes, and any effects of connections or gas flow were successfully addressed. A protocol was developed for quantifying the L_{TPB} of each cell, and it was confirmed that there was a strong dependence of Ni-SDC cell polarization on the triple phase boundary length. The reciprocal of the polarization resistance, or interfacial conductance, per unit TPB remains relatively constant, implying that the TPBs are the only active sites for the electrode reactions, and the activities of the TPB are relatively uniform. Using this knowledge, the activity ($1/R_p$) of each cell was normalized by the L_{TPB} (Ni-SDC interfaces), allowing the quantification of activity between different cells and materials. Several observations on the basic electrochemical behavior of these model cells were made, including activation energies for the anodic reaction, and a general discussion of the impedance spectra. The application of functional coatings was found to dramatically affect the L_{TPB} normalized activity of the model cells. Application of precious metal doped CeO_2 coatings, such as Ni, Ru and Pt doped CeO_2 increased the activity of the anode towards H_2 even when the Ni surface was covered by a relatively thick ceramic film (>100 nm). Similar coverage of the Ni component by Sm-doped CeO_2 reduced the activity of the cell.

These results have demonstrated the potential of the embedded mesh architecture as a platform for rigorous screening and comparison of candidate catalyst coatings in future

SOFC materials development, and further motivate the addition of catalytically active coatings to Ni-based SOFC anodes to increase activity, while simultaneously protecting the Ni component from common poisons (such as H_2S) and carbon deposition. Through the design and development of a new operando Raman system, capable of testing SOFC materials under true operating conditions, this work has further contributed to the available characterization techniques possible for SOFC testing.

This work clearly sets the path for future research. The fundamental goal is to use the embedded mesh model cells to identify highly active catalyst coatings which provide high performance in both hydrogen and hydrocarbon fuels, without degradation or deposition of carbon (coking). Although much effort has been made to identify the correct conditions and coating materials for direct hydrocarbon tests using the model cells, key obstacles remain before adequate experimental results can be produced regarding film deposition and testing conditions. Once a suitable catalyst coating can be deposited that yields high performance and stability in hydrocarbon fuels, the fundamental mechanisms of electrode processes and structure-property relationships responsible can then be identified using the described operando chamber. These efforts and some initial observations have been described in the attached appendix. Through combination of the embedded mesh model cell and operando Raman chamber, this work lays out a new strategy for accelerated materials development for new SOFC anode coatings.

CHAPTER 6. CONCLUSIONS

SOFC technology has a current and pressing need to improve performance at lower temperatures. This work addresses this need in two ways, first by demonstrating a high performing SOFC design, and second, by advancing current SOFC testing capabilities. The SOFC design makes special use of a precious metal doped CeO_2 anode reforming layer to enable direct methane operation at temperatures as low as 500 °C. Structure property relationships were determined for this reforming catalyst, supported by in situ spectroscopy and DFT simulation, which attribute the high performance to a synergy between the ionic Ni and Ru dopants, and the unique defect structure caused by their introduction into the CeO_2 lattice. Raman analysis was used to determine the successful substitutional doping of both Ru and Ni. New peaks were observed due to the presence of these dopants, which predicted defect formation under high temperature reducing conditions. Cationic Ruthenium was correlated with dramatically enhanced formation of M^{3+} and V_O^{**} defects under in situ conditions, whereas the Ni dopant did not enhance in situ defect formation. DFT analysis supported the main conclusions of Raman experiments, and provided additional understanding of the role of each dopant in Steam Reforming. Briefly, the presence of cationic Ni provided enhanced CH_4 activation, and the cationic Ru increased the presence and formation rate of oxygen vacancies and the activation of steam through the filling of these vacancies.

The current SOFC testing capabilities are limited, often leading to empirical developments rather than rational design based on fundamental understanding of materials chemistry. A model cell was demonstrated for the investigation of new catalysts on the surface of a Ni-

SDC based anode, which is limited by the anodic processes of the cell. The basic assumptions of the cell were validated, showing SOFC behaviour, anode dominated impedance spectra, and direct relation between anodic polarization and triple phase boundary length. The cell enabled quantitative comparison of activity, normalized by the triple phase boundary length, and showed the effect of several thin film catalyst coatings on anodic impedance. The open architecture of the model cell not only enabled the ready deposition and comparison of different thin films of catalysts, but also is ideally suited for operando Raman experiments. To this end, an operando Raman chamber was designed and fabricated, which replicated the standard button-cell testing. This chamber was able to safely reach fuel cell operating temperatures as high as 750 ° C, and was precisely machined to fit the standard cell culture plate dimensions used on common motorized microscope stages, suitable for spatial resolution measurements and Raman mapping of the model anode surface

CHAPTER 7. RECCOMENDATIONS

This high performance demonstrated by the low temperature SOFC described in this work should inspire further investigation in the application of anode reforming layers to high-performance, low- and intermediate-temperature SOFC designs, as this strategy is currently underutilized. The use of precious metal doped CeO_2, in which highly active metals (e.g. Ru, Pt, Ni, etc) are ionically stabilized and exhibit remarkable catalytic activity, is especially attractive for SOFC application and these catalysts should be should be further explored for this application. Raman spectroscopy was found to be a powerful too in the

investigation of the defect structure of precious metal doped CeO_2, which was dynamic under operating conditions. Current literature on the Raman spectra of these materials is limited, and warrants more in depth analysis on the specific vibrational modes which produce the observed spectra both ex situ and in situ.

The embedded mesh Ni-SDC model cell was demonstrated as a powerful new characterization capability and is expected to provide increased understanding of SOFC anode surfaces, and catalyst coatings. These cells provide a stable testing platform for the deposition of candidate catalyst coating for more rigorous and less time-intensive screening. The combination of these model cells and the operando chamber described in this work is expected to accelerate the advancement of SOFC materials development by relating the observed Raman spectra to electrochemical behaviour of candidate anode materials, the especially for low-temperature applications in aggressive fuels.

APPENDIX

A.1 Use of model cells to investigate use of Ni-SDC for intermediate temperature hydrocarbon use

As discussed in Chapter 4, one of the primary advantages of SOFCs over PEFCs is their potential ability to efficiently run on hydrocarbon fuels. The two major obstacles to direct hydrocarbon use are low activity and corrosion, primarily by carbon deposition and poisoning by sulphur species present in modern logistics fuels. Embedded mesh model electrodes provide a unique platform for studying the degradation reactions in these fuels, although analysis of the electrochemical behaviour is lacking, as studies were primary limited to symmetric cell configurations of Ni-YSZ cells or prototype full cells with highly porous and poorly defined electrodes. These electrodes provide a relatively large amount of non-electrochemically active sites which can be active to various reforming reactions, convoluting any direct electrochemical reactions with the hydrocarbon, as the more active H_2 is produced by these reforming reactions The planar model anode provides the ideal substrate for the study of direct electrochemical oxidation of hydrocarbons, as the sites are limited and entirely electrochemical, with very little surface area available for internal reforming of the fuel before in interacts with the active triple phase boundary sites. To demonstrate the application of the embedded mesh Ni-SDC cells in the analysis of SOFC anodes tested in hydrocarbon fuels, cells were subjected to testing in three common fuels: methane, propane, and methanol.

A.1.1 Model cell testing in methane fuel

As the main component of natural gas, methane is the most attractive fuel for intermediate temperature SOFC operation. As discussed in section 4.1.1, internal reforming reactions such as steam reforming and dry reforming are less thermodynamically favoured at temperatures below 650 °C, and therefore the direct electrochemical oxidation of CH_4 is a more important possibility at low and intermediate temperatures.

In a similar approach to H_2 testing discussed in chapter 5, embedded mesh model cells were heated in H_2 and annealed at 750 °C for 4 h before testing at the desired temperature. After stabilizing cells at 600 C in 60 sccm H_2, the gas was abruptly changed from H_2 to CH_4 (both gasses were flowed through a water bubbler, ~3% H_2O). As the fuel was changed, the OCV of the cells rapidly decreased to ~ 200 mV in the methane atmosphere (Figure 82).

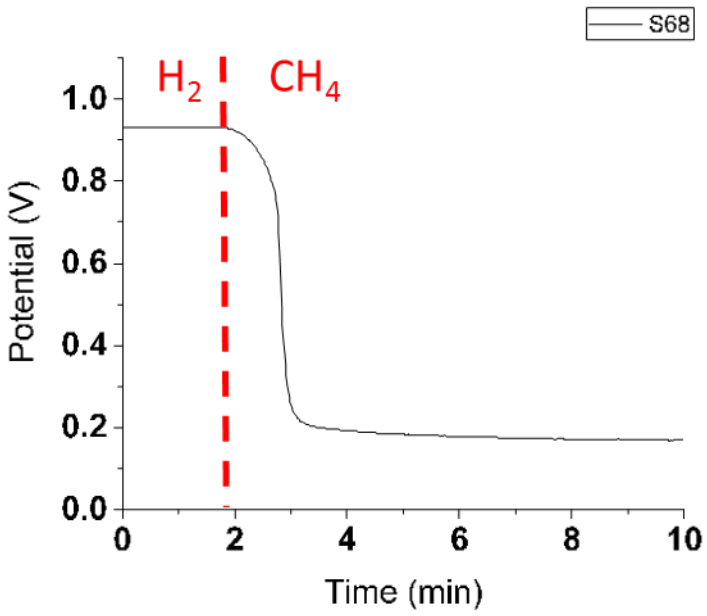

Figure 82 – Plot of measured open circuit potential (OCV) of bare Ni-SDC model cell during switch from 60 scmm H_2 (3%H_2O) to 60 sccm CH_4 (3%H_2O) at 600 °C.

After a certain incubation time, periodic oscillations in OCV occurred, with peak values nearing the original OCV measured in hydrogen (Figure 83). Oscillatory behaviour occurred on all samples tested in methane, regardless of catalyst coating, with similar incubation time and peak/valley height. The oscillation in voltage remained constant for several hours with no change in peak or valley voltage values.

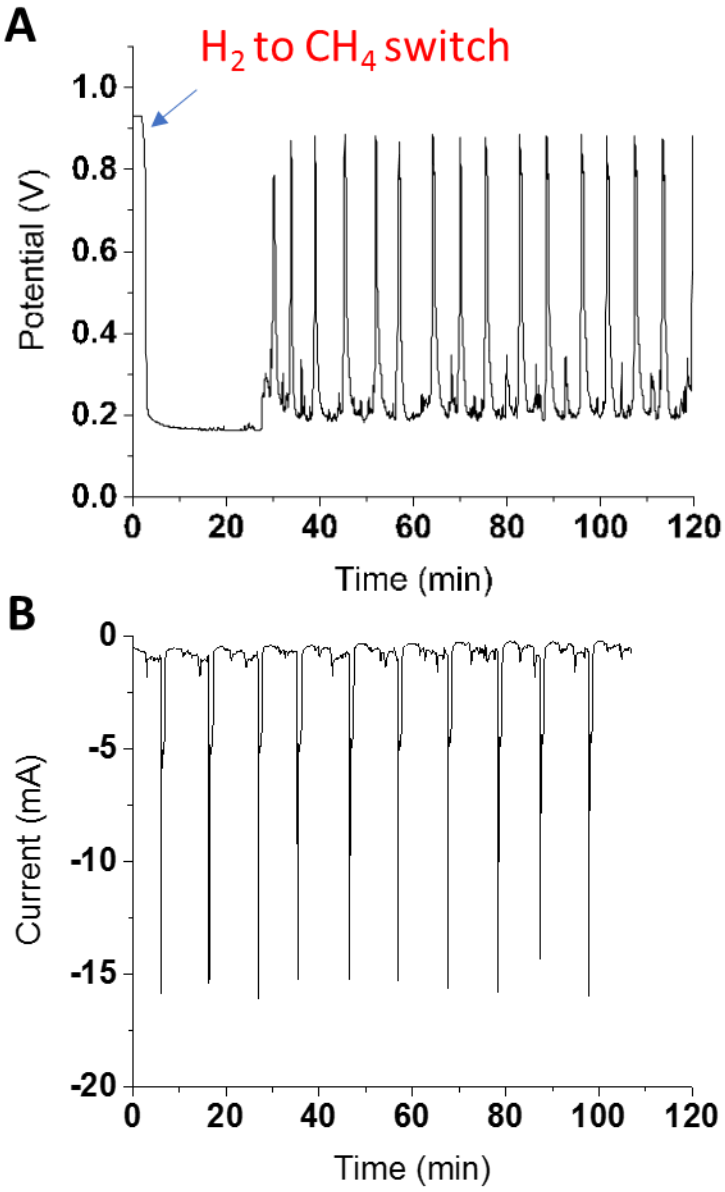

Figure 83 – (A) Plot of measured open circuit potential (OCV) of bare Ni-SDC model cell during switch from 60 sccm H_2 (3%H_2O) to 60 sccm CH_4 (3%H_2O) at 600 °C. Switch occurred at 2 min in this figure, oscillation began at 28 min. (B) current measure of cell under 60 sccm CH_4 at constant 0.6 V.

These oscillations were found to be variable as a function of temperature, with narrowing voltage oscillations as temperature is increased and widening oscillation as temperature is decreased (Figure 84).

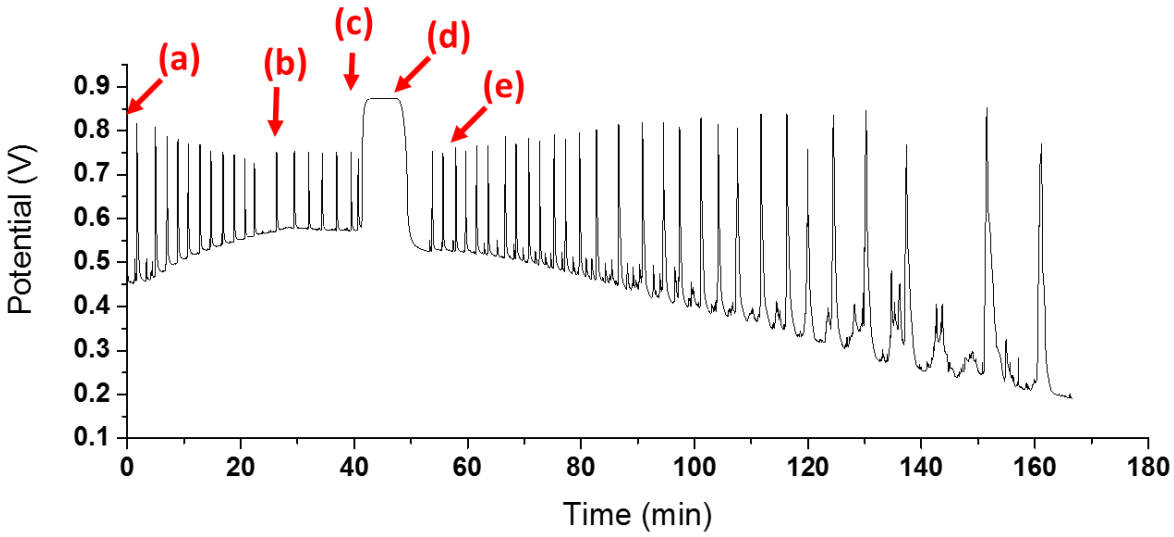

Figure 84 – Plot of open cell voltage of a Ni-SDC model cell fueled with 60 sccm CH_4 (3%H_2O) as temperature is varied. (a) 650 °C, heating at 2 °C/min, (b) held at 700 °C, (c) switch from CH_4 to H_2, (d) switched from H_2 back to CH_4, (e) started cooling at 2 °C/min.

Due to the instability of voltage in methane, impedance spectra could not be collected under methane (oscillations is voltage occur faster than the time required for an impedance scan). Therefore, to track the activity of the cell as a function of time exposed to methane, the cell was periodically returned to H_2 for impedance collection. This process was repeated several times over a 24 h period, as shown in Figure 85.

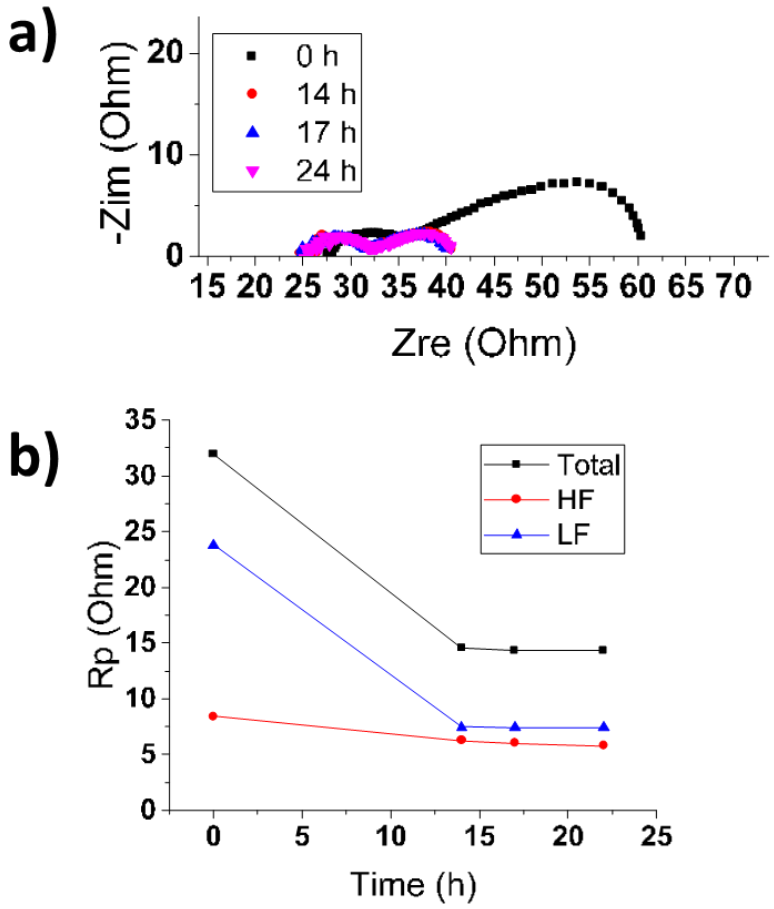

Figure 85 – (a) impedance spectra collected at 600 °C in H_2 after various exposure times to methane fuel, (b) plot of polarization values collected in H_2, as a function of time exposed to methane fuel.

After this experiment, the samples were cooled back to room temperature in flowing H_2 for characterization. Top-down SEM, shown in Figure 86, reveals significant surface modification of the Ni component. A rough and porous film was grown on the Ni surface, which appeared microcrystalline and exhibited different microstructure dependent on the

exposed grain structure of the polished Ni, with additional growth along the Ni grain boundaries.

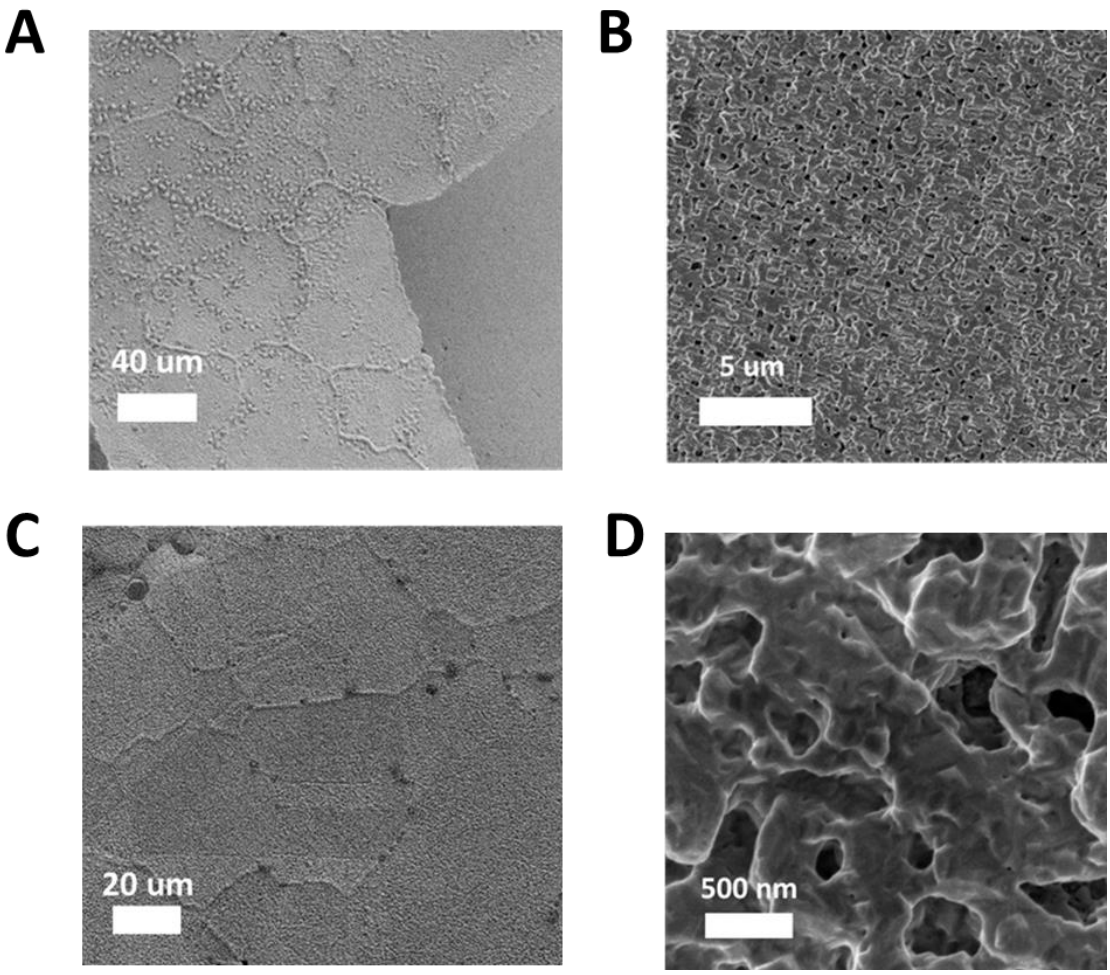

Figure 86 – Top-down SEM images of the Ni surface of model cell after 24 h of operation in methane fuel, cycling back to H_2 for impedance measurements. Magnification is increased through (A-D). Sample was cooled to room temperature under flowing H_2.

Chemical analysis of the Ni surface after testing revealed that the surface was primarily Ni (Figure 87), with no detectable carbon signal by either EDS or Raman (which would be expected from carbon deposition). In comparison, a cell tested in parallel with a shorter, 1

h exposure to propane, showed a dramatic increase in both EDS and Raman signal for carbon. Testing in propane will be discussed in a later section, and this result is presented here as a reference.

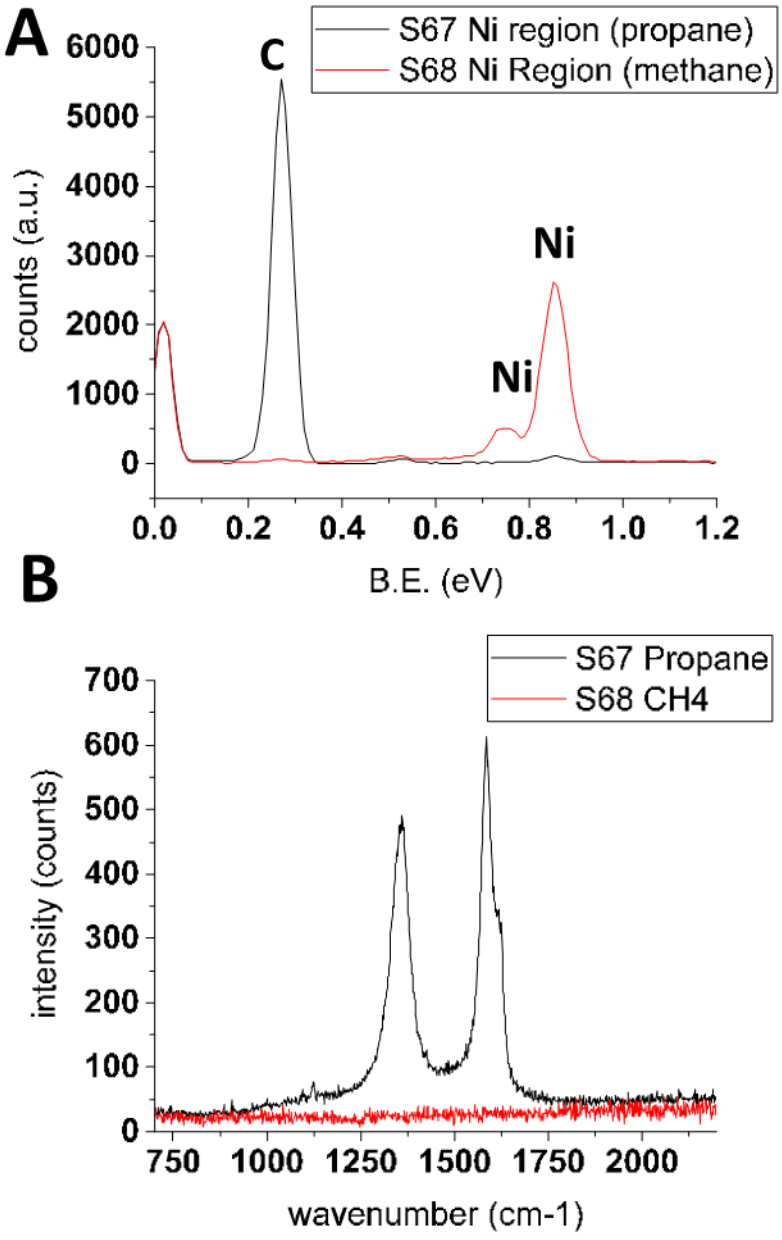

Figure 87 – (a) EDS and (b) Raman spectra of model cells after cyclic exposure to CH4 (S68) and exposure to propane fuel (S67). Raman spectra shown represent the average of four scans over different locations on the Ni surface.

There are several possible explanations for oscillatory behaviour proposed in the literature, although an exact mechanism remains in dispute.[107-110] Coking has been shown to briefly improve cell performance, due to the increased electrical conductivity of the anode with the addition of graphite deposits, but the performance soon begins to degrade as the carbon deposit covers the active sites. Huang et al described a similar voltage pattern in their cells, which they ascribed to the cyclical oxidation and reduction of the metallic anode component (in this case Ni). The restructuring of the Ni surface resulted in a porous film with higher surface area than the original anode, increasing the surface area of the Ni component and the amount of active triple phase boundary interfaces.

The observation that the impedance of the cell markedly decreased after 12 h of exposure to methane at OCV, then stabilizes, suggests that coking is likely not responsible for the oscillatory behaviour. Carbon would block active sites and thus increased anodic impedance, and the impedance would be expected to continue to increase as more carbon is deposited over time. In addition, the surface of theF Ni component after testing in CH_4 shows a porous Ni film had formed, with additional feature height and density on different Ni facet orientations, as well as along the Ni grain boundaries. This type of morphology is similar to that reported for high temperature oxidation of Ni, which exhibits short-circuit diffusion of Ni cations trough the NiO grain boundary as well as the growth of oxide protuberances (due to the higher rate of Ni cation diffusion to the material surface than the rate of oxygen diffusion to the Ni). Therefore, the results of these experiments suggest that the model cell shows oscillation in voltage (and current density under potentiostatic conditions) due to the cyclic oxidation/reduction of the Ni component. In contrast to other direct methane SOFCs, the embedded mesh model cell has a very limited amount of

exposed Ni, and therefore there are less sites for reforming of the methane to H_2 before it reaches the triple phase boundary sites. The direct electrochemical oxidation of methane may be very sluggish, and if the methane is not being efficiently oxidized the fuel atmosphere becomes less reducing. Therefore, the oscillations likely occur through the periodic transformation of the Ni surface from active/conductive Ni to inert/insulating NiO. During the initial switch from H_2 to CH_4, there is a smooth decrease in OCV as the concentration of H_2 is flushed from the anode. When the fuel composition equilibrates at 97% CH_4 3% H_2O, the oxygen vacancies of the SDC likely start to fill and eventually the local effective pO_2 of the surface reaches a critical point at which the Ni surface is oxidized to NiO. Due to the higher diffusion rate of Ni cations through NiO relative to O^{2-}, the NiO film grows at the gas/solid interface, forming a nanostructured surface with additional growth features along short-circuit diffusion paths such as grain boundaries. Eventually, this nanostructured NiO film becomes active enough to catalyse the oxidation of the CH_4 fuel, which causes a dramatic decrease in the effective pO_2 of the fuel, reducing the NiO back to Ni. When returned to the metallic Ni state, the anode will rapidly achieve a higher activity and OCV, since the metallic Ni is more active and most importantly electronically conductive. Still, the kinetics of the methane activation are low under these conditions and the Ni quickly reoxidizes to NiO and the OCV rapidly drops again. This process continues, and the repeated oxidation and reduction of the NiO film forms a porous, high surface area Ni.

The cyclic growth and reduction of the NiO film on the surface would be expected to form a porous structure, as was observed in post mortem SEM, increasing the number of interfaces with the SDC electrolyte. This yields a possible explanation for the increased

activity of the cell when it is returned to a pure H_2 atmosphere, as the surface area of the anode is effectively increased as the polished Ni surface becomes porous. Similar explanations have been posited, and further suggestions that conditions of low Ni site density (such as those inherent to the embedded mesh architecture) may exasperate and amplify this oscillation phenomena.[110]

These oscillations in voltage and current were consistently observed in several tests, including those with the active coatings described in Chapter 5. There is significant interest in the identification of a coating material which can protect the Ni component from coking while simultaneously reforming or directly oxidizing the hydrocarbon fuel, and the model cell platform was designed in part to quickly screen a variety of coating materials for direct methane operation. Although a basic explanation of the observed oscillation is given, the most productive research direction is to attempt to avoid these oscillations and find conditions in which stable impedance can be collected, as was done in H_2 fuels. Before different catalyst materials can be accurately studied for direct methane oxidation, the testing conditions must be further optimized to remove the oscillatory behaviour, through changes in gas composition, L_{TPB}, or catalyst morphology.

A.1.2 Model cell testing in propane fuel

In contrast to results in methane, there was no observed oscillation in propane fuels during testing under both open circuit and constant potential. The current of an embedded mesh cell operated at 0.6 V during a switch from H_2 to propane fuel is shown in Figure 88.

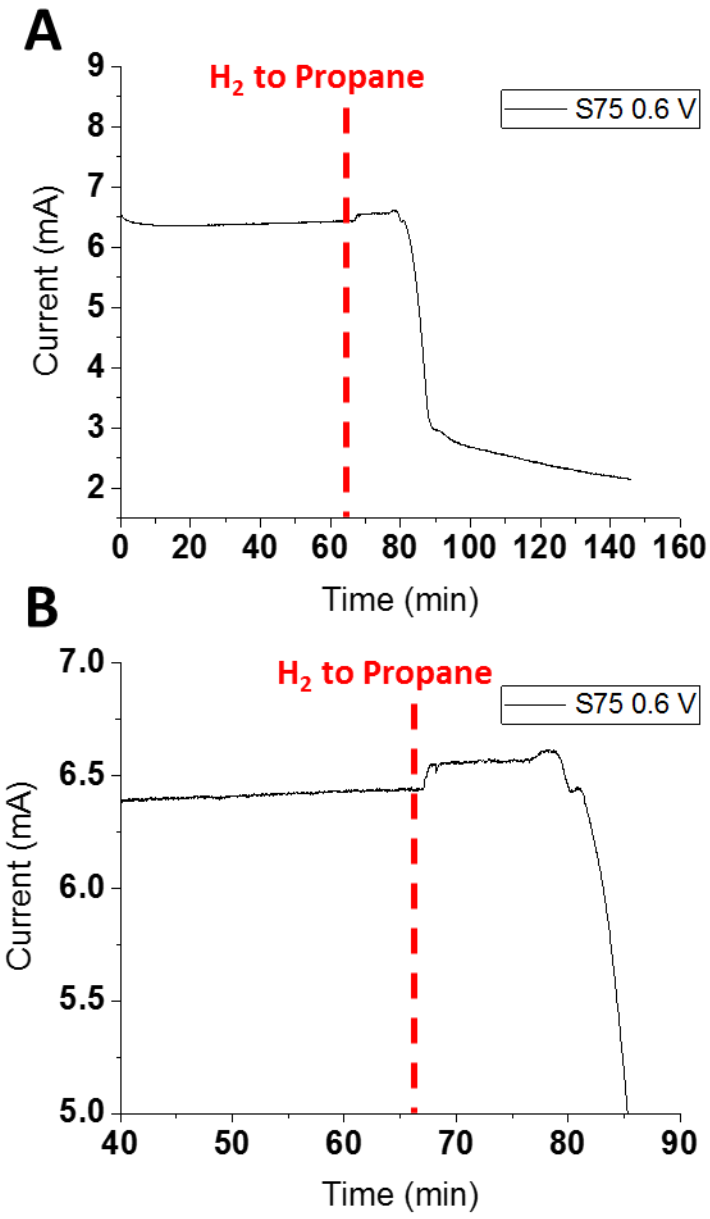

Figure 88 – (A) Current at 0.6 V for a model cell during switch from 60 sccm H_2 to 60 sccm propane (both fuel humidified to 3% H_2O). (B) Adjustment of scale of plot from (A) highlighting the immediate effects of the fuel switch

After an initial increase, the current quickly decreases to a steady baseline, about 10% the value measured in the H_2 fuel. As no oscillations were observed, EIS was used to collect

impedance spectra in both hydrogen and propane fuels. As shown in Figure 89, the Rp increased dramatically in propane, relative to H_2.

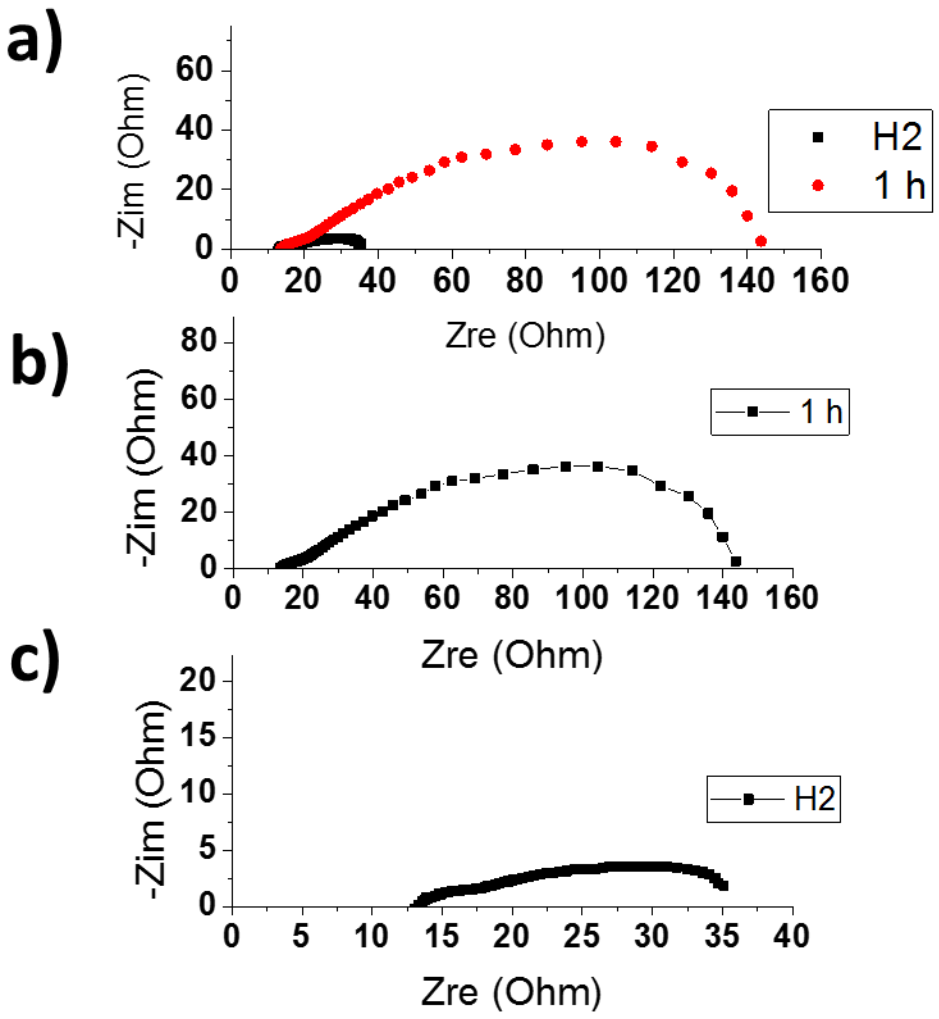

Figure 89 – Impedance spectra of embedded mesh model cell collected at 600 °C, while holding at 0.6 V, before and after one hour of exposure to 3%H_2O humidified propane fuel. Spectra are overlaid together in (a) and then the propane and H_2 spectra are plotted separately for clarity in (b) and (c), respectively.

Since the voltage and current of the cell was relatively constant in propane fuel, the impedance could be tracked as a function of time. The cell was held at 0.6 V for roughly

12 hours, taking impedance spectra periodically. The current output of the model cell decreased steadily over this time, as the measured impedance increased. As shown in Figure 90, the degradation of the cell was primarily due to the increase in the ohmic resistance of the cell, although the Rp increased substantially after the switch from hydrogen, it was relatively stable over the remainder of the 12 h test. .

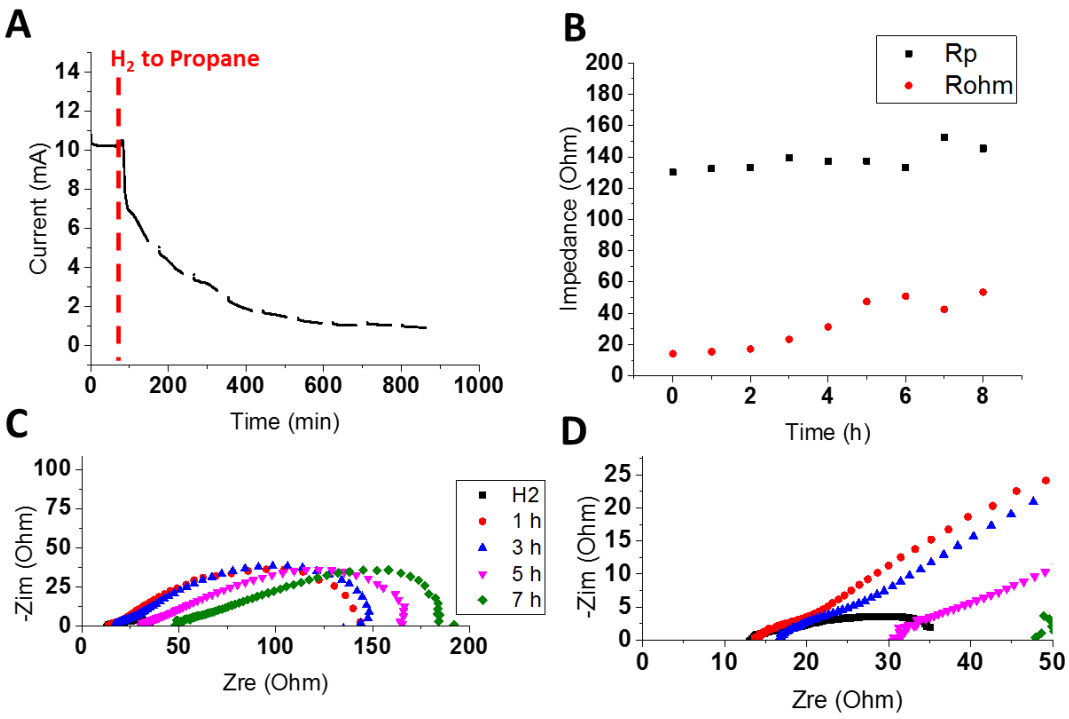

Figure 90 – (A) plot of current as a function of time for an embedded mesh model cell. Fuel atmosphere was changed from $H_2$to Propane at 62 min, as illustrated by the line in red. (B) plot of impedance contributions from anodic polarization (Rp) and bulk ohmic resistance (Rohm) as a function of time exposed to propane. (C) Impedance spectra collected at 0.6 V in H_2 and propane as a function of exposure time (impedance were collected in time period gaps in (A)). (D) rescaling of (C) to highlight the relatively low impedance collected from the cell in H_2 at 0.6 V.

Two key observations are made from model cell testing in propane: (i) the performance in propane was decreased, but the cell remained operational, and (ii) Although the Rp of the cell in propane was much larger than the Rohmic of the cell increased during operation in propane, more so than the Rp. The lower performance in propane could be due to either lower activity to the hydrocarbon, or due to corrosion of the Ni surface by carbon deposition. The large increase in Rohmic, relative to Rp, suggests that degradation of the anodic current collection occurred, since the bulk of the electrolyte is isolated from the propane atmosphere and should be unaffected by the fuel. This could be due to the possible lift-off of the Nickel phase from the SDC bulk, or of the Ag paste connection from the surface, caused by the growth of solid carbon on the surface.

Post mortem analysis of the cells operated in propane show clear and significant carbon deposition, in the form of carbon fibers, on the Ni surface. Raman spectra and SEM images are shown in Figure 91; Raman spectroscopy of the model anode surface clearly show the G and 2D peaks, indicative of graphitic carbon, which was corroborated by the strong carbon signal detected by EDS of the Ni component (Figure 92). There was no carbon deposition on the ceramic phases, demonstrating the catalytic nature of this corrosion mechanisms, i.e. even though carbon deposition is thermodynamically favoured in these conditions, the presence of a C-C formation catalyst is required (Ni).

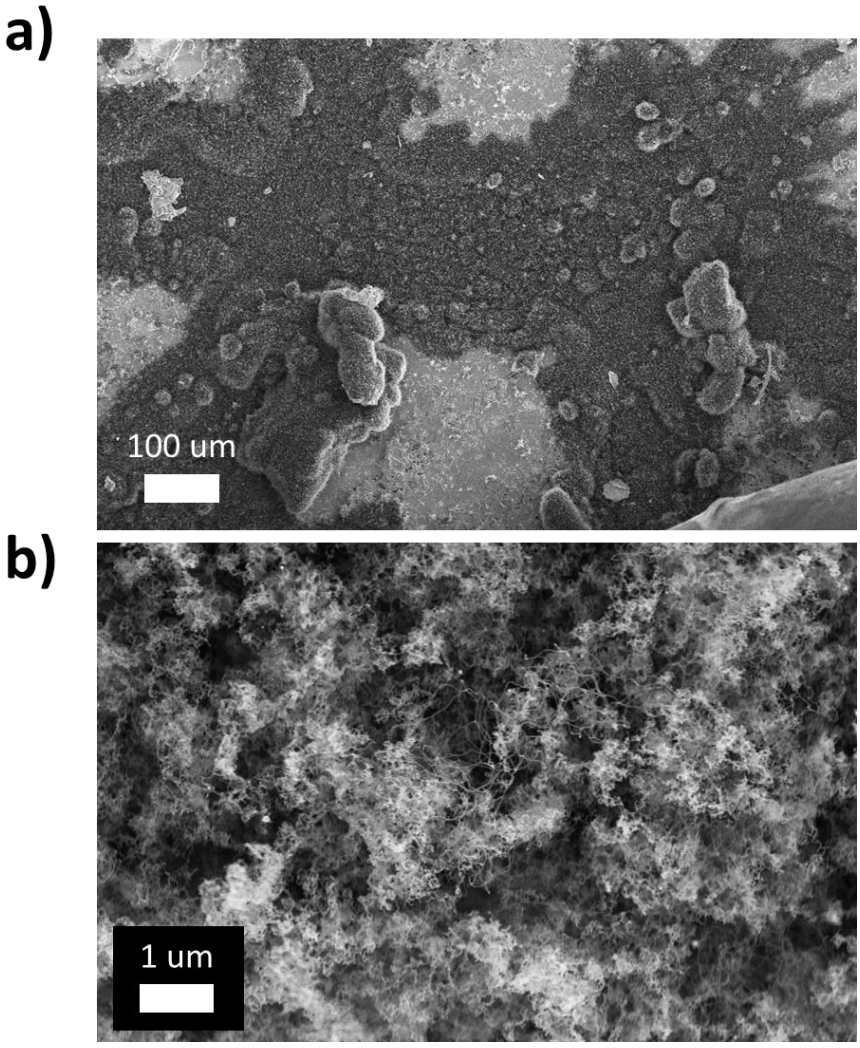

Figure 91 – Top down SEM images of bare Ni-SDC model cell after 12 h of potentiostatic (0.6 V) operation in propane at 600 °C. 60 sccm of propane, humidified to 3%H_2O was flowed over the anode, with ambient air over the cathode.

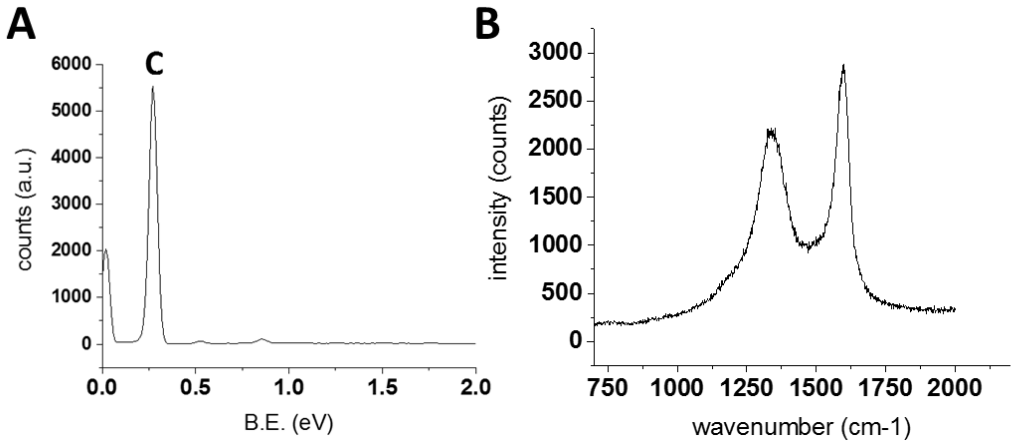

Figure 92 – (A) EDS and (B) Raman signal collected from the Ni surface of the model cell after testing in propane, from the cell shown in Figure 91.

A.2 Conclusions of model cell testing in hydrocarbons

The Ni-SDC embedded mesh model cells were tested in both methane and propane fuels. In methane, the cells exhibited severe oscillations in both open circuit voltage, as well as output current density. No evidence of coking during methane testing was observed, and post-mortem analysis showed evidence of surface restructuring of the Ni surface caused by cyclic oxidation and reduction (Ni to NiO). The increased surface area caused by the restructuring increased the baseline activity in H_2, after long term exposure to CH_4. Although significant efforts were taken to avoid this oscillation, since the unstable voltage inhibited the collection of impedance spectra, this behaviour persisted with different temperatures, surface coatings, and gas compositions. Before these Ni-SDC model cells can be used to make strong conclusions on the behaviour of SOFC materials under direct methane operation, the conditions must be optimized to avoid the oscillation, and therefore this is the recommended research direction as this work continues.

In propane there were no oscillations observed, but severe coking quickly inhibited the model cells. The graphitic carbon fibers covered the Ni surface while leaving the SDC electrolyte relatively un-touched, demonstrating the need for protective coatings to isolate the Ni component from the hydrocarbon fuel while retaining high activity. Further optimization of catalyst coating process is necessary, in order to achieve stable propane operation. This testing platform was able to immediately identify the degredation mechanisms and anode activity during tests in hydrocarbon fuels, and therefore is expected to be a critical tool in ongoing anode materials development for direct hydrocarbon SOFCs.

REFERENCES

1 Gür, T. M. Comprehensive review of methane conversion in solid oxide fuel cells: Prospects for efficient electricity generation from natural gas. *Progress in Energy and Combustion Science* **54**, 1-64, doi:https://doi.org/10.1016/j.pecs.2015.10.004 (2016).

2 Gellings, P. J. & Bouwmeester, H. *Handbook of solid state electrochemistry*. (CRC press, 1997).

3 Stambouli, A. B. & Traversa, E. Solid oxide fuel cells (SOFCs): a review of an environmentally clean and efficient source of energy. *Renewable and sustainable energy reviews* **6**, 433-455 (2002).

4 Lefebvre-Joud, F., Gauthier, G. & Mougin, J. Current status of proton-conducting solid oxide fuel cells development. *Journal of applied electrochemistry* **39**, 535-543 (2009).

5 Yang, L. *et al.* Enhanced sulfur and coking tolerance of a mixed ion conductor for SOFCs: BaZr0. 1Ce0. 7Y0. 2–xYbxO3–δ. *Science* **326**, 126-129 (2009).

6 Li, M., Hua, B., Pu, J., Chi, B. & Jian, L. Electrochemical performance and carbon deposition resistance of M-BaZr 0.1 Ce 0.7 Y 0.1 Yb 0.1 O 3-δ (M= Pd, Cu, Ni or NiCu) anodes for solid oxide fuel cells. *Scientific Reports* **5**, 7667 (2015).

7 Duan, C. *et al.* Readily processed protonic ceramic fuel cells with high performance at low temperatures. *Science* **349**, 1321-1326 (2015).

8 Gao, Z., Mogni, L. V., Miller, E. C., Railsback, J. G. & Barnett, S. A. A perspective on low-temperature solid oxide fuel cells. *Energy & Environmental Science* **9**, 1602-1644 (2016).

9 Wachsman, E. D. & Lee, K. T. Lowering the temperature of solid oxide fuel cells. *Science* **334**, 935-939 (2011).

10 Hanna, J., Lee, W. Y., Shi, Y. & Ghoniem, A. Fundamentals of electro-and thermochemistry in the anode of solid-oxide fuel cells with hydrocarbon and syngas fuels. *Progress in Energy and Combustion Science* **40**, 74-111 (2014).

11 Bard, A. J., Faulkner, L. R., Leddy, J. & Zoski, C. G. *Electrochemical methods: fundamentals and applications*. Vol. 2 (wiley New York, 1980).

12 Pekridis, G., Kalimeri, K., Kaklidis, N., Athanasiou, C. & Marnellos, G. Electrode polarization measurements in the Fe|SrCe0.95Yb0.05O2.975|Au proton conducting solid electrolyte cell. *Solid State Ionics* **178**, 649-656, doi:https://doi.org/10.1016/j.ssi.2007.02.005 (2007).

13 contributors, W. *Raman spectroscopy*, <https://en.wikipedia.org/w/index.php?title=Raman_spectroscopy&oldid=888262233> (

14 Salunkhe, A., Khot, V., Phadatare, M. & Pawar, S. Combustion synthesis of cobalt ferrite nanoparticles—Influence of fuel to oxidizer ratio. *Journal of alloys and compounds* **514**, 91-96 (2012).

15 Yuvaraj, S., Fan-Yuan, L., Tsong-Huei, C. & Chuin-Tih, Y. Thermal decomposition of metal nitrates in air and hydrogen environments. *The Journal of Physical Chemistry B* **107**, 1044-1047 (2003).

16 Deganello, F., Marcì, G. & Deganello, G. Citrate–nitrate auto-combustion synthesis of perovskite-type nanopowders: a systematic approach. *Journal of the European Ceramic Society* **29**, 439-450 (2009).

17 Segadaes, A. M., Morelli, M. R. & Kiminami, R. G. Combustion synthesis of aluminium titanate. *Journal of the European Ceramic Society* **18**, 771-781 (1998).

18 Jain, S., Adiga, K. & Verneker, V. P. A new approach to thermochemical calculations of condensed fuel-oxidizer mixtures. *Combustion and flame* **40**, 71-79 (1981).

19 Ding, D., Li, X., Lai, S. Y., Gerdes, K. & Liu, M. Enhancing SOFC cathode performance by surface modification through infiltration. *Energy & Environmental Science* **7**, 552-575 (2014).

20 Lou, X. *et al.* Controlling the morphology and uniformity of a catalyst-infiltrated cathode for solid oxide fuel cells by tuning wetting property. *Journal of Power Sources* **195**, 419-424 (2010).

21 Nie, L., Liu, M., Zhang, Y. & Liu, M. La 0.6 Sr 0.4 Co 0.2 Fe 0.8 O 3− δ cathodes infiltrated with samarium-doped cerium oxide for solid oxide fuel cells. *Journal of Power Sources* **195**, 4704-4708 (2010).

22 Oh, T.-S., Yu, A. S., Adijanto, L., Gorte, R. J. & Vohs, J. M. Infiltrated lanthanum strontium chromite anodes for solid oxide fuel cells: Structural and catalytic aspects. *Journal of Power Sources* **262**, 207-212, doi:http://dx.doi.org/10.1016/j.jpowsour.2014.03.141 (2014).

23 Liu, Z. *et al.* Fabrication and modification of solid oxide fuel cell anodes via wet impregnation/infiltration technique. *Journal of Power Sources* **237**, 243-259 (2013).

24 Cheng, Z. & Liu, M. Characterization of sulfur poisoning of Ni–YSZ anodes for solid oxide fuel cells using in situ Raman microspectroscopy. *Solid State Ionics* **178**, 925-935 (2007).

25 Blinn, K. S. *et al.* Raman spectroscopic monitoring of carbon deposition on hydrocarbon-fed solid oxide fuel cell anodes. *Energy & Environmental Science* **5**, 7913-7917 (2012).

26 Cheng, Z. *et al.* From Ni-YSZ to sulfur-tolerant anode materials for SOFCs: electrochemical behavior, in situ characterization, modeling, and future perspectives. *Energy & Environmental Science* **4**, 4380-4409 (2011).

27 Hanna, J., Lee, W., Shi, Y. & Ghoniem, A. Fundamentals of electro-and thermochemistry in the anode of solid-oxide fuel cells with hydrocarbon and syngas fuels. *Progress in Energy and Combustion Science* **40**, 74-111 (2014).

28 Vernoux, P., Guindet, J. & Kleitz, M. Gradual Internal Methane Reforming in Intermediate-Temperature Solid-Oxide Fuel Cells. *Journal of The Electrochemical Society* **145**, 3487-3492, doi:10.1149/1.1838832 (1998).

29 Lai, S. Y., Ding, D., Liu, M., Liu, M. & Alamgir, F. M. Operando and In situ X-ray Spectroscopies of Degradation in La0. 6Sr0. 4Co0. 2Fe0. 8O3− δ Thin Film Cathodes in Fuel Cells. *ChemSusChem* **7**, 3078-3087 (2014).

30 Klein, J.-M., Hénault, M., Roux, C., Bultel, Y. & Georges, S. Direct methane solid oxide fuel cell working by gradual internal steam reforming: Analysis of operation. *Journal of Power Sources* **193**, 331-337 (2009).

31 Zhan, Z. & Barnett, S. A. An Octane-Fueled Solid Oxide Fuel Cell. *Science* **308**, 844-847 (2005).

32 Zhan, Z. & Barnett, S. A. Operation of ceria-electrolyte solid oxide fuel cells on iso-octane–air fuel mixtures. *Journal of Power Sources* **157**, 422-429, doi:http://dx.doi.org/10.1016/j.jpowsour.2005.08.008 (2006).

33 Liu, X. *et al.* Enabling catalysis of Ru–CeO2 for propane oxidation in low temperature solid oxide fuel cells. *Journal of Power Sources* **199**, 138-141, doi:http://dx.doi.org/10.1016/j.jpowsour.2011.09.072 (2012).

34 Sun, C., Xie, Z., Xia, C., Li, H. & Chen, L. Investigations of mesoporous CeO 2–Ru as a reforming catalyst layer for solid oxide fuel cells. *Electrochemistry communications* **8**, 833-838 (2006).

35 Shao, Z. *et al.* A thermally self-sustained micro solid-oxide fuel-cell stack with high power density. *Nature* **435**, 795-798, doi:http://www.nature.com/nature/journal/v435/n7043/suppinfo/nature03673_S1.html (2005).

36 Zhan, Z. & Barnett, S. A. Use of a catalyst layer for propane partial oxidation in solid oxide fuel cells. *Solid State Ionics* **176**, 871-879, doi:http://dx.doi.org/10.1016/j.ssi.2004.12.005 (2005).

37 Wang, W., Zhou, W., Ran, R., Cai, R. & Shao, Z. Methane-fueled SOFC with traditional nickel-based anode by applying Ni/Al2O3 as a dual-functional layer. *Electrochemistry Communications* **11**, 194-197, doi:http://dx.doi.org/10.1016/j.elecom.2008.11.014 (2009).

38 Suzuki, T. *et al.* Application of catalytic layer on solid oxide fuel cell anode surface. *Electrochemistry Communications* **15**, 26-28, doi:http://dx.doi.org/10.1016/j.elecom.2011.11.016 (2012).

39 Weber, W. H., Hass, K. C. & McBride, J. R. Raman study of ${\mathrm{CeO}}_{2}$: Second-order scattering, lattice dynamics, and particle-size effects. *Physical Review B* **48**, 178-185 (1993).

40 Tao, Z., Hou, G., Xu, N. & Zhang, Q. A highly coking-resistant solid oxide fuel cell with a nickel doped ceria: Ce1−xNixO2−y reformation layer. *International Journal of Hydrogen Energy* **39**, 5113-5120, doi:http://dx.doi.org/10.1016/j.ijhydene.2014.01.092 (2014).

41 Bera, P. & Hegde, M. S. Noble metal ions in CeO2 and TiO2: synthesis, structure and catalytic properties. *RSC Advances* **5**, 94949-94979, doi:10.1039/C5RA16474E (2015).

42 McFarland, E. W. & Metiu, H. Catalysis by doped oxides. *Chemical reviews* **113**, 4391-4427 (2013).

43 Argyle, M. D. & Bartholomew, C. H. Heterogeneous Catalyst Deactivation and Regeneration: A Review. *Catalysts* **5**, 145-269 (2015).

44 Upham, D. C., Derk, A. R., Sharma, S., Metiu, H. & McFarland, E. W. CO 2 methanation by Ru-doped ceria: the role of the oxidation state of the surface. *Catalysis Science & Technology* **5**, 1783-1791 (2015).

45 Ciston, J. *et al.* Morphological and Structural Changes during the Reduction and Reoxidation of CuO/CeO2 and Ce1–xCuxO2 Nanocatalysts: In Situ Studies with Environmental TEM, XRD, and XAS. *The Journal of Physical Chemistry C* **115**, 13851-13859, doi:10.1021/jp203882h (2011).

46 Hartman, T., Wondergem, C. S., Kumar, N., van den Berg, A. & Weckhuysen, B. M. Surface- and Tip-Enhanced Raman Spectroscopy in Catalysis. *The Journal of Physical Chemistry Letters* **7**, 1570-1584, doi:10.1021/acs.jpclett.6b00147 (2016).

47 Hegde, M., Madras, G. & Patil, K. Noble metal ionic catalysts. *Accounts of chemical research* **42**, 704-712 (2009).

48 Myung, J.-h., Shin, T. H., Huang, X., Carins, G. & Irvine, J. T. S. Enhancement of redox stability and electrical conductivity by doping various metals on ceria, Ce1−xMxO2−δ (M = Ni, Cu, Co, Mn, Ti, Zr). *International Journal of Hydrogen Energy* **40**, 12003-12008, doi:http://dx.doi.org/10.1016/j.ijhydene.2015.05.029 (2015).

49 Kehoe, A. B., Scanlon, D. O. & Watson, G. W. Role of lattice distortions in the oxygen storage capacity of divalently doped CeO2. *Chemistry of Materials* **23**, 4464-4468 (2011).

50 Hegde, M. S. & Bera, P. Noble metal ion substituted CeO2 catalysts: Electronic interaction between noble metal ions and CeO2 lattice. *Catalysis Today* **253**, 40-50, doi:https://doi.org/10.1016/j.cattod.2015.03.035 (2015).

51 Sharma, S., Hu, Z., Zhang, P., McFarland, E. W. & Metiu, H. CO2 methanation on Ru-doped ceria. *Journal of Catalysis* **278**, 297-309, doi:https://doi.org/10.1016/j.jcat.2010.12.015 (2011).

52 Acerbi, N., Tsang, S. C. E., Jones, G., Golunski, S. & Collier, P. Rationalization of Interactions in Precious Metal/Ceria Catalysts Using the d-Band Center Model. *Angewandte Chemie International Edition* **52**, 7737-7741, doi:10.1002/anie.201300130 (2013).

53 Chen, Y. *et al.* A robust fuel cell operated on nearly dry methane at 500° C enabled by synergistic thermal catalysis and electrocatalysis. *Nature Energy* **3**, 1042 (2018).

54 Chen, Y. *et al.* A highly efficient and robust nanofiber cathode for solid oxide fuel cells. *Advanced Energy Materials* **7**, 1601890 (2017).

55 Chen, Y. *et al.* A Highly Efficient Multi-phase Catalyst Dramatically Enhances the Rate of Oxygen Reduction. *Joule* **2**, 938-949 (2018).

56 Chen, Y. *et al.* A robust and active hybrid catalyst for facile oxygen reduction in solid oxide fuel cells. *Energy & Environmental Science* **10**, 964-971 (2017).

57 Chen, Y. *et al.* A durable, high-performance hollow-nanofiber cathode for intermediate-temperature fuel cells. *Nano Energy* **26**, 90-99 (2016).

58 Liu, M., Ding, D., Bai, Y., He, T. & Liu, M. An efficient SOFC based on samaria-doped ceria (SDC) electrolyte. *Journal of The Electrochemical Society* **159**, B661-B665 (2012).

59 Sun, W., Shi, Z., Qian, J., Wang, Z. & Liu, W. In-situ formed Ce0. 8Sm0. 2O2− δ@ Ba (Ce, Zr) 1− x (Sm, Y) xO3− δ core/shell electron-blocking layer towards Ce0. 8Sm0. 2O2− δ-based solid oxide fuel cells with high open circuit voltages. *Nano Energy* **8**, 305-311 (2014).

60 Chen, Y. *et al.* A highly active, CO2-tolerant electrode for the oxygen reduction reaction. *Energy & Environmental Science* **11**, 2458-2466, doi:10.1039/C8EE01140K (2018).

61 Mai, H.-X. *et al.* Shape-selective synthesis and oxygen storage behavior of ceria nanopolyhedra, nanorods, and nanocubes. *The Journal of Physical Chemistry B* **109**, 24380-24385 (2005).

62 Suzuki, T. *et al.* A functional layer for direct use of hydrocarbon fuel in low temperature solid-oxide fuel cells. *Energy & Environmental Science* **4**, 940-943 (2011).

63 Hibino, T. *et al.* An Intermediate-Temperature Solid Oxide Fuel Cell Providing Higher Performance with Hydrocarbons than with Hydrogen. *Electrochemical and Solid-State Letters* **5**, A242-A244, doi:10.1149/1.1508551 (2002).

64 Lin, Y., Zhan, Z., Liu, J. & Barnett, S. A. Direct operation of solid oxide fuel cells with methane fuel. *Solid State Ionics* **176**, 1827-1835 (2005).

65 Morgan, D. J. Resolving ruthenium: XPS studies of common ruthenium materials. *Surface and Interface Analysis* **47**, 1072-1079, doi:10.1002/sia.5852 (2015).

66 Chen, Y. *et al.* A robust fuel cell operated on nearly dry methane at 500° C enabled by synergistic thermal catalysis and electrocatalysis. *Nature Energy*, 1 (2018).

67 Nakajima, A., Yoshihara, A. & Ishigame, M. Defect-induced Raman spectra in doped CeO 2. *Physical Review B* **50**, 13297 (1994).

68 Zoellner, M. H. *et al.* Temperature-Dependent Reduction of Epitaxial Ce1–xPrxO2−δ (x = 0–1) Thin Films on Si(111): A Combined Temperature-Programmed Desorption, X-ray Diffraction, X-ray Photoelectron Spectroscopy, and Raman Study. *The Journal of Physical Chemistry C* **117**, 24851-24857, doi:10.1021/jp4082867 (2013).

69 Wu, Z., Li, M., Howe, J., Meyer III, H. M. & Overbury, S. H. Probing defect sites on CeO2 nanocrystals with well-defined surface planes by Raman spectroscopy and O2 adsorption. *Langmuir* **26**, 16595-16606 (2010).

70 Chan, H. Y. H., Takoudis, C. G. & Weaver, M. J. High-pressure oxidation of ruthenium as probed by surface-enhanced Raman and X-ray photoelectron spectroscopies. *Journal of Catalysis* **172**, 336-345 (1997).

71 Weinstock, N., Schulze, H. & Müller, A. Assignment of ν2 (E) and ν4 (F 2) of tetrahedral species by the calculation of the relative Raman intensities: The vibrational spectra of VO 4 3−, CrO 4 2−, MoO 4 2−, WO 4 2−, MnO 4−, TcO 4−, ReO 4−, RuO4, and OsO4. *The Journal of Chemical Physics* **59**, 5063-5067 (1973).

72 Satsuma, A., Yanagihara, M., Ohyama, J. & Shimizu, K. Oxidation of CO over Ru/Ceria prepared by self-dispersion of Ru metal powder into nano-sized particle. *Catalysis today* **201**, 62-67 (2013).

73 Guo, Y. *et al.* Low-Temperature CO2 Methanation over CeO2-Supported Ru Single Atoms, Nanoclusters and Nanoparticles Competitively Tuned by Strong Metal-Support Interactions and H-Spillover Effect. *ACS Catalysis* (2018).

74 Huang, H., Dai, Q. & Wang, X. Morphology effect of Ru/CeO2 catalysts for the catalytic combustion of chlorobenzene. *Applied Catalysis B: Environmental* **158**, 96-105 (2014).

75 Wang, F. *et al.* Catalytic behavior of supported Ru nanoparticles on the {1 0 0},{1 1 0}, and {1 1 1} facet of CeO2. *Journal of Catalysis* **329**, 177-186 (2015).

76 Li, W., Srinivasan, S. G., Salahub, D. & Heine, T. Ni on the CeO 2 (110) and (100) surfaces: adsorption vs. substitution effects on the electronic and geometric structures and oxygen vacancies. *Physical Chemistry Chemical Physics* **18**, 11139-11149 (2016).

77 Nolan, M. Enhanced oxygen vacancy formation in ceria (111) and (110) surfaces doped with divalent cations. *Journal of Materials Chemistry* **21**, 9160-9168 (2011).

78 Li, Q. *et al.* Simultaneous ni doping at atom scale in ceria and assembling into well-defined lotuslike structure for enhanced catalytic performance. *ACS applied materials & interfaces* **9**, 16243-16251 (2017).

79 Pal, P., Singha, R. K., Saha, A., Bal, R. & Panda, A. B. Defect-induced efficient partial oxidation of methane over nonstoichiometric Ni/CeO2 nanocrystals. *The Journal of Physical Chemistry C* **119**, 13610-13618 (2015).

80 Andriopoulou, C. *et al.* Structural and Redox Properties of Ce1–x Zr x O2− δ and Ce0. 8Zr0. 15RE0. 05O2− δ (RE: La, Nd, Pr, Y) Solids Studied by High Temperature in Situ Raman Spectroscopy. *The Journal of Physical Chemistry C* **121**, 7931-7943 (2017).

81 Mamontov, E., Egami, T., Brezny, R., Koranne, M. & Tyagi, S. Lattice Defects and Oxygen Storage Capacity of Nanocrystalline Ceria and Ceria-Zirconia. *The Journal of Physical Chemistry B* **104**, 11110-11116, doi:10.1021/jp0023011 (2000).

82 Bessler, W. G. *et al.* Model anodes and anode models for understanding the mechanism of hydrogen oxidation in solid oxide fuel cells. *Physical Chemistry Chemical Physics* **12**, 13888-13903, doi:10.1039/C0CP00541J (2010).

83 Mizusaki, J. *et al.* Preparation of Nickel Pattern Electrodes on YSZ and Their Electrochemical Properties in H 2-H 2 O Atmospheres. *Journal of the Electrochemical Society* **141**, 2129-2134 (1994).

84 Mizusaki, J. *et al.* Kinetic studies of the reaction at the nickel pattern electrode on YSZ in H2・H2O atmospheres. *Solid State Ionics* **70-71**, 52-58, doi:https://doi.org/10.1016/0167-2738(94)90286-0 (1994).

85 Bessler, W. G., Warnatz, J. & Goodwin, D. G. The influence of equilibrium potential on the hydrogen oxidation kinetics of SOFC anodes. *Solid State Ionics* **177**, 3371-3383 (2007).

86 Bieberle, A., Meier, L. P. & Gauckler , L. J. The Electrochemistry of Ni Pattern Anodes Used as Solid Oxide Fuel Cell Model Electrodes. *Journal of The Electrochemical Society* **148**, A646-A656, doi:10.1149/1.1372219 (2001).

87 Chueh, W. C., Hao, Y., Jung, W. & Haile, S. M. High electrochemical activity of the oxide phase in model ceria–Pt and ceria–Ni composite anodes. *Nature materials* **11**, 155 (2012).

88 Chueh, W. C., Lai, W. & Haile, S. M. Electrochemical behavior of ceria with selected metal electrodes. *Solid State Ionics* **179**, 1036-1041 (2008).

89 Choi, Y., Brown, E. C., Haile, S. M. & Jung, W. Electrochemically modified, robust solid oxide fuel cell anode for direct-hydrocarbon utilization. *Nano Energy* **23**, 161-171 (2016).

90 Utz, A., Störmer, H., Gerthsen, D., Weber, A. & Ivers-Tiffée, E. Microstructure stability studies of Ni patterned anodes for SOFC. *Solid State Ionics* **192**, 565-570, doi:https://doi.org/10.1016/j.ssi.2010.05.004 (2011).

91 Yao, W. & Croiset, E. Ni/YSZ pattern anodes fabrication and their microstructure and electrochemical behavior changes in H2–H2O environments. *Journal of Power Sources* **226**, 162-172, doi:https://doi.org/10.1016/j.jpowsour.2012.10.053 (2013).

92 Doppler, M. C., Fleig, J., Bram, M. & Opitz, A. K. Hydrogen oxidation mechanisms on Ni/yttria stabilized zirconia anodes: Separation of reaction pathways by geometry variation of pattern electrodes. *Journal of Power Sources* **380**, 46-54, doi:https://doi.org/10.1016/j.jpowsour.2018.01.073 (2018).

93 Sun, W. *et al.* Hydrogen oxidation at the Pt–BaZr 0.1 Ce 0.7 Y 0.1 Yb 0.1 O 3− δ (BZCYYb) interface. *Physical Chemistry Chemical Physics* **15**, 3820-3826 (2013).

94 Li, X. *et al.* An operando surface enhanced Raman spectroscopy (SERS) study of carbon deposition on SOFC anodes. *Physical Chemistry Chemical Physics* **17**, 21112-21119, doi:10.1039/C4CP05176A (2015).

95 Blinn, K. S., Li, X., Liu, M., Bottomley, L. A. & Liu, M. Probing and mapping electrode surfaces in solid oxide fuel cells. *Journal of visualized experiments: JoVE* (2012).

96 Nakamura, T. *et al.* Determination of the Reaction Zone in Gadolinia-Doped Ceria Anode for Solid Oxide Fuel Cell. *Journal of The Electrochemical Society* **155**, B1244-B1250, doi:10.1149/1.2975322 (2008).

97 Jung, W., Dereux, J. O., Chueh, W. C., Hao, Y. & Haile, S. M. High electrode activity of nanostructured, columnar ceria films for solid oxide fuel cells. *Energy & Environmental Science* **5**, 8682-8689 (2012).

98 Liu, M. & Hu, H. Effect of Interfacial Resistance on Determination of Transport Properties of Mixed-Conducting Electrolytes. *Journal of the Electrochemical Society* **143**, L109-L112 (1996).

99 Chueh, W. C., Lai, W. & Haile, S. M. Electrochemical behavior of ceria with selected metal electrodes. *Solid State Ionics* **179**, 1036-1041, doi:https://doi.org/10.1016/j.ssi.2007.12.087 (2008).

100 Jung, W., Gu, K. L., Choi, Y. & Haile, S. M. Robust nanostructures with exceptionally high electrochemical reaction activity for high temperature fuel cell electrodes. *Energy & Environmental Science* **7**, 1685-1692 (2014).

101 Takagi, Y., Lai, B.-K., Kerman, K. & Ramanathan, S. Low temperature thin film solid oxide fuel cells with nanoporous ruthenium anodes for direct methane operation. *Energy & Environmental Science* **4**, 3473-3478 (2011).

102 Matolín, V. *et al.* Platinum-doped CeO2 thin film catalysts prepared by magnetron sputtering. *Langmuir* **26**, 12824-12831 (2010).

103 Bode, G. L. *et al.* Electrochemical and Operando Spectroscopic Studies of Sr2Fe1. 5Mo0. 5O6-δ Anode Catalysts in Solid Oxide Fuel Cells Operating with Direct Alcohol Fuels. *ChemElectroChem* **5**, 3162-3168 (2018).

104 Pomfret, M. B., Owrutsky, J. C. & Walker, R. A. High-Temperature Raman Spectroscopy of Solid Oxide Fuel Cell Materials and Processes. *The Journal of Physical Chemistry B* **110**, 17305-17308, doi:10.1021/jp063952l (2006).

105 Kirtley, J. D., Pomfret, M. B., Steinhurst, D. A., Owrutsky, J. C. & Walker, R. A. Toward a Working Mechanism of Fuel Oxidation in SOFCs: In Situ Optical Studies of Simulated Biogas and Methane. *The Journal of Physical Chemistry C* **119**, 12781-12791, doi:10.1021/jp511304x (2015).

106 Brightman, E. *et al.* Designing a miniaturised heated stage for in situ optical measurements of solid oxide fuel cell electrode surfaces, and probing the oxidation of solid oxide fuel cell anodes using in situ Raman spectroscopy. *Review of Scientific Instruments* **83**, 053707 (2012).

107 Bebelis, S. *et al.* Methane oxidation on composite ruthenium electrodes in YSZ cells. *Solid State Ionics* **177**, 2087-2091, doi:https://doi.org/10.1016/j.ssi.2006.02.014 (2006).

108 Kokkofitis, C. & Stoukides, M. Rate and oxygen activity oscillations during propane oxidation on Pt/YSZ. *Journal of Catalysis* **243**, 428-437, doi:https://doi.org/10.1016/j.jcat.2006.07.032 (2006).

109 Huang, T.-J., Huang, M.-C., Chen, W.-J. & Chou, C.-L. Oscillation of electrical current during direct methane oxidation over Ni-added LSCF–GDC anode of solid oxide fuel cells. *Chemical Engineering Journal* **153**, 164-169, doi:https://doi.org/10.1016/j.cej.2009.06.014 (2009).

110 Lee, D., Kim, D., Kim, J. & Moon, J. Characterizing nano-scale electrocatalysis during partial oxidation of methane. *Scientific Reports* **4**, 3937, doi:10.1038/srep03937

https://www.nature.com/articles/srep03937#supplementary-information (2014).